Type of the Paper (Article.)

Two finite mirror-image series restrict the non-trivial zeros of Riemann's *zeta* function to $\mathrm{Re}(s) = \frac{1}{2}$ and the zeros of its derivative to $\mathrm{Re}(s) > \frac{1}{2}$.

Anthony Lander

Department of Surgery, Birmingham Women's and Children's Hospital, Steelhouse Lane, Birmingham B4 6NH, UK

Correspondence: tony.lander@bch.nhs.uk; Tel.: +44-121-333-9999

Abstract: Euler's product formula over the primes and Euler's *zeta* function equate to enshrine the Fundamental Theorem of Arithmetic that every integer > 1 is the product of a unique set of primes. The product formula has no zero, and with a domain ≤ 1 Euler's *zeta* diverges. Dirichlet's *eta* function $\eta(s)$, negates alternate terms of *zeta*, permitting convergence when $s \in \mathbb{C}$ and $\mathrm{Re}(s) < 1$, and its non-trivial zeros $\{\rho\}$, have a deep relationship with the distribution of the primes. The Riemann Hypothesis is that all the non-trivial zeros have $\mathrm{Re}(\rho) = \frac{1}{2}$. This work examines the symmetries in a partial Euler's *zeta* series with a complex domain equating it to the difference between two finite vector series whose matched terms have mirror-image arguments, but whose magnitudes differ when $\mathrm{Re}(s) \neq \frac{1}{2}$. Analytical continuation generates a modified *eta* series $\eta_l(s)$, in which every l^{th} term is multiplied by $(1 - l)$. If the integer l is appropriately determined by the $\mathrm{Im}(s)$, similar paired finite vector series have a difference that closely follows $\eta_l(s)$ and their terminal vectors intersect in a unique way permitting zeros only when $\mathrm{Re}(s) = \frac{1}{2}$. Furthermore, those vectors tracking the derivatives of the series, have a special relationship permitting zeros of the differential only when $\mathrm{Re}(s) > \frac{1}{2}$.

Keywords: Riemann Hypothesis; Dirichlet *eta* function; *Zeta* function; prime numbers; number theory; critical-line; critical-strip; symmetry breaking

---

1. Introduction

Proposition 30 of Book VII of Euclid's Elements, known as Euclid's lemma, states that if p is a prime number and $p|ab$, where a and b are integers then $p|a$ or $p|b$ [1]. This lemma with propositions 31 and 32 give us the Fundamental Theorem of Arithmetic, namely that every integer > 1 is the product of a unique set of primes $n = p_1^{a_1} p_2^{a_2} p_3^{a_3} \ldots p_i^{a_i}$, where $p_1 = 2$, $p_2 = 3$, $p_3 = 5, \ldots.$.

The Fundamental Theorem of Arithmetic is encoded in the *zeta* function equating to Euler's product formula over the primes thus

$$\zeta(\sigma) = \sum_{n=1}^{\infty} n^{-\sigma} = \prod_{p=primes} \frac{1}{1 - p^{-\sigma}} = \prod_{p=primes} (1 + p^{-\sigma} + p^{-2\sigma} + \cdots) \text{ with } \sigma \in \mathbb{R}. \qquad (1)$$

To see this clearly the right hand side of Equation (1) is multiplied out

$$\zeta(\sigma) = 1 + p_1^{-\sigma} + p_2^{-\sigma} + p_1^{-2\sigma} + p_3^{-\sigma} + p_1^{-\sigma} p_2^{-\sigma} + p_4^{-\sigma} + p_1^{-3\sigma} + p_2^{-2\sigma} + p_1^{-\sigma} p_3^{-\sigma} + \cdots .$$

As the positive integers increase, the primes thin out with $\pi(x)$, the number of primes less than x, being asymptotic to $x/\ln(x)$. This asymptotic distribution, known as the Prime Number Theorem was conjectured by Gauss in the 1790's and proved independently by Hadamard [2] and de la Vallée Poussin [3] in 1896 using the Riemann *zeta* function. In November 1859 Riemann published his paper "On the Number of Primes Less Than a Given Magnitude" [4]. Riemann only refers to the imaginary component with the variable t and does not assign a symbol to the real component. We follow convention and let $\sigma = \mathrm{Re}(s)$. Riemann's paper contains an explicit formula for $\pi(x)$, given in terms of the related function $\Pi(x)$ which counts the primes and prime powers up to x, counting a prime power p^n, as $1/n$ of a prime, thus

$$\Pi(x) = \pi(x) + \frac{1}{2}\pi\left(x^{\frac{1}{2}}\right) + \frac{1}{3}\pi\left(x^{\frac{1}{3}}\right) + \frac{1}{4}\pi\left(x^{\frac{1}{4}}\right) + \frac{1}{5}\pi\left(x^{\frac{1}{5}}\right) + \cdots.$$

The Möbius function $\mu(n)$, is related to the inverse of $\zeta(s)$

$$\frac{1}{\zeta(s)} = \sum_{n=1}^{\infty} \frac{\mu(n)}{n^s},$$

which enables the number of primes to be recovered,

$$\pi(x) = \sum_{n=1}^{\infty} \frac{\mu(n)}{n} \Pi\left(x^{\frac{1}{n}}\right).$$

Riemann's formula then becomes

$$\Pi_0(x) = \mathrm{Li}(x) - \sum_{\rho} \mathrm{Li}(x^{\rho}) - \ln(2) + \int_x^{\infty} \frac{dt}{t(t^2-1)\ln(t)}$$

where $\mathrm{Li}(x) = \int_0^x \frac{1}{\ln(t)} dt$ is the un-offset logarithmic integral and $\{\rho\}$ are the non-trivial zeros.

Riemann believed that $\mathrm{Re}(\rho)$ was always $\frac{1}{2}$ but did not demonstrate this as it was not central to his paper. There is ample empirical evidence [5], but no accepted proof that $\mathrm{Re}(\rho) = \frac{1}{2}$ for all ρ. In the language of the *zeta* function, σ is limited to the "critical-line" in the middle of the "critical-strip" $(0 < \mathrm{Re}(s) < 1)$. In 1914 Hardy [6] proved the infinitude of $\{\rho\}$ with $\sigma = \frac{1}{2}$, which we will call $\{\rho_i\}$ indexing those on the critical-line with i, but Hardy's proof does not preclude there being other real values in the critical-strip off the line. Importantly, the functional equation

$$\zeta(s) = \Gamma(1-s)(2\pi)^{s-1} 2\sin\left(\frac{\pi s}{2}\right)\zeta(1-s), \tag{2}$$

imposes a symmetry about the critical-line and the real axis becomes a line of reflection [7].

Euler's *zeta* function is classically confined to the real axis and diverges when $\sigma \le 1$. If in place of σ we have $s \in \mathbb{C}$ with $s = \sigma + it$ and $i = \sqrt{-1}$ then Euler's *zeta* has a pathway of diminishing vectors in the Argand plane. After a countable set of individual vectors, that often seem to lack overt structure, in what can be called the proximal pathway the vectors of Euler's *zeta* series enter a countable set of superstructures in its distal pathway. The superstructures, here designated $\mathcal{R}_r$, are paired pseudo-spirals whose *principal-axes* can be equated to vectors, here designated $\vec{\mathcal{R}}_r$, which are objects in their own right. The $\vec{\mathcal{R}}_r$, form their own series of diminishing vectors running counter to the pathway of Euler's *zeta* and soon form superstructures of their own, with *principal-axes* which can be equated to the proximal vectors of Euler's *zeta*. The largest pair of pseudo-spirals $\mathcal{R}_1$, has a final pseudo-convergence that precedes the slowly growing spiral of inevitable divergence. The cardinality of the set of proximal vectors equates to that of the set of distal superstructures. The location of the final pseudo-convergence can be remarkably close to zero. Apart from cardinality, there is a striking symmetry between the arguments of neighbouring vectors of the paired sets under all real domains but a symmetry between their magnitudes only when $\sigma = \frac{1}{2}$.

Analytical continuation in Dirichlet's *eta* function $\eta(s)$, abolishes the spiral of divergence through negation of alternate terms. Dirichlet's *eta* locates the non-trivial zeros $\{\rho\}$, which are remarkably similar to the minima of an appropriately terminated Euler's partial *zeta* series, but the relationships between the proximal and distal vectors in Dirichlet's *eta* are less clear.

This work characterises the overt symmetries in the pathway of the partial Euler's *zeta* vector series preceding its final divergent expanding spiral. A similar analysis applies to the covert but easily exposed symmetries in a family of analytically continued modified Dirichlet *eta* functions. Once exposed, the symmetries in the modified *eta* function can be tracked by two short finite vector series whose behaviour, under changes in the $\mathrm{Re}(s)$, confirms Riemann's Hypothesis through a simple symmetry breaking argument. The implications for the derivative easily follow and reinforce that confirmation.

doi:10.20944/preprints201703.0121.v1

2. Materials and Methods

2.1. Resources

Microsoft Excel 2010 with Visual Basic was used for repetitive calculations and GraphPad Prism 5 for Windows was used to create figures. A published table of non-trivial zeros was obtained [8].

2.2. Terminology and notation, unknown non-trivial zeros ρ_u, and ignoring the sign of t

In this work the formulation $\zeta(s)$ is principally used for Riemann's *zeta* function, whilst $\zeta_n(s)$ is restricted to Euler's *zeta* function to n terms acting on $s \in \mathbb{C}$. The following sets are used; $\mathbb{O} = \{1, 3, 5, 7 \dots\}$, $\mathbb{E} = \{2, 4, 6, 8 \dots\}$, $\mathbb{N} = \{1, 2, 3, 4 \dots\}$ and $\mathbb{N}_0 = \{0, 1, 2, 3, 4 \dots\}$.

If $f_{l,n}(s)$ is a vector series to n terms influenced by l, then $\mathrm{P}(f_{l,n}(s))$ is used to mean the pathway of sequential vectors representing the terms of that series when plotted in the Argand plane. In this way $\mathrm{P}(f_{l,n}(s))$ is richer than $f_{l,n}(s)$ which on its own identifies a point in the plane, or implies a vector to that point. If $f_{l,n}(s)$ is used as a vector this is implied by context and not notation. Each series has a specific index using different fonts/scripts; care is needed to avoid confusion.

This work describes four divergent vector series and their pathways $\mathrm{P}(\zeta_n(s)), \mathrm{P}(h_{l,r}(s))$, $\mathrm{P}\left(\bar{h}_{l,r}(s)\right)$ and $\mathrm{P}(\ell_{l,\mathfrak{n}}(s))$, these summate using the indices m, r, r and n respectively to final terms of n, r, r and $\mathfrak{n}$. The vectors of these series are $\vec{m}$, $\vec{\mathcal{R}}_r$, $\vec{\mathcal{R}}_r$ and $\vec{\mathcal{L}}_n$ respectively. The pathway of the converging $\mathrm{P}(\eta_{l,n}(s))$ has index m, runs to n terms and summates vectors designated $\vec{m}$.

Each divergent pathway passes through a number of pseudo-convergences before entering a final pseudo-convergence which precedes the infinite spiral of divergence. In any series the term corresponding to the vector preceding the growing spiral of divergence is designated *tau*, τ. These pathways also have proximal and distal parts separated by a vector at a term *kappa*, κ. The converging $\mathrm{P}(\eta_{l,n}(s))$ has a related proximo-distal separation at its κl vector when $l > \kappa$, and the function $\eta_l(s)$, can be considered as $\eta_l(\sigma)$ with t fixed, or $\eta_l(t)$ with σ fixed, since curves with one parameter fixed are informative.

The known non-trivial zeros are the set $\{\rho_i\}$, each having $\mathrm{Re}(\rho_i) = ½$ and $\mathrm{Im}(\rho_i) \in \{t_i\}$. An unknown non-trivial zero off the critical-line is designated ρ_u with $\mathrm{Re}(\rho_u) \neq ½$ and $t = t_u$ with $t_u \notin \{t_i\}$. The functional equation, Equation (2), demands that if $\zeta(\sigma_\alpha + it_u) = 0$ then $\zeta(\sigma_\beta - it_u) = 0$ when the restriction $\sigma_\beta = 1 - \sigma_\alpha$ applies. Since the sign of t can be ignored without weakening our conclusions we will consider that if there is a $\rho_{u_\alpha} = \sigma_\alpha + it_u$ then there is a $\rho_{u_\beta} = \sigma_\beta + it_u$, see Figure 1. We will let RH mean the Riemann Hypothesis being, $Re(\rho) = \frac{1}{2}$ for all ρ.

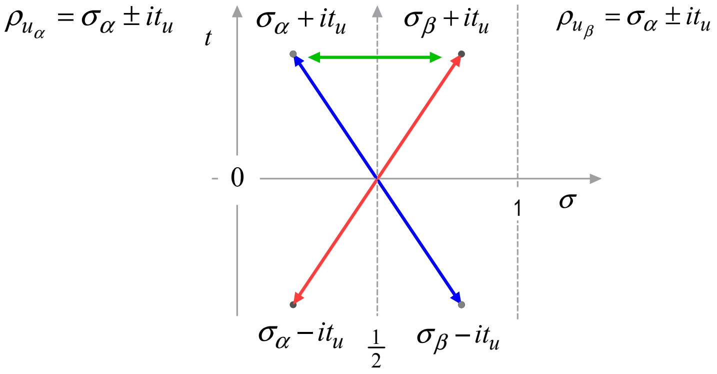

Figure 1. The critical-strip and the critical-line are shown with four related hypothetical zeros. The functional equation follows the red and blue double arrows. We limit σ_α to the left of the critical-line and σ_β to the right. The green line is a mapping of $\rho_{u_\alpha} = \sigma_\alpha + it_u$ to $\rho_{u_\beta} = \sigma_\beta + it_u$ which is formally equivalent to the functional equation ignoring the sign of t.

The notation $[x]$ means the nearest integer to $x \in \mathbb{R}$, with floor $\lfloor x \rfloor$ and ceiling $\lceil x \rceil$ functions meaning the nearest integers below and above x respectively. The notation $[\![x]\!]$ is used to mean the nearest element to x in an ordered set; so if the set were $\mathbb{E}$ then $4 = [\![3.1]\!]$. Additional objects are detailed in the text and listed in Appendix B Notation.

2.3. Salient points in this work

Whilst outlining the strategies of this work this section introduces a number of mathematical objects, including the five vector series $\zeta_n(s)$, $\eta_{l,n}(s)$, $\ell_{l,n}(s)$, $h_{l,r}(s)$ and $\bar{h}_{l,r}(s)$. Some objects, common to more than one function, are introduced before their associated functions. The Results section expands upon the enumerated points and illustrates the anatomy and behaviour of the vector series and their pathways.

1. A partial Euler's *zeta* series, without analytical continuation is defined as;

$$\zeta_n(s) := \sum_{m=1}^{n} m^{-s} = \sum_{m=1}^{n} \vec{m}, \tag{3}$$

with the vectors $\vec{m}$ having

$$|\vec{m}| = m^{-\sigma} \text{ and } \arg(\vec{m}) = -t\ln(m).$$

2. The series $\zeta_n(s)$ has a transition when $m = \tau$, at a vector $\vec{m} = \vec{\tau}$ in $\mathrm{P}(\zeta_n(s))$ which signals the end of the final pseudo-convergence and the start of spiraling divergence. *Tau* is a function of t alone in Euler's *zeta* and in the series $\ell_{l,n}(s)$ which is described below. *Tau* is also a function of t and l for the diverging vector series $h_{l,r}(s)$ and $\bar{h}_{l,r}(s)$ both of which summate a series of vectors designated $\vec{\mathcal{R}}_r$ which are also described below. There are two related formulations;

$$\tau = \left[\tfrac{1}{2}\left(\left(e^{\frac{\pi}{t}} - 1\right)^{-1} + \left(1 - e^{\frac{-\pi}{t}}\right)^{-1}\right)\right] \text{ for Euler's zeta } \zeta_\tau(s) \text{ and } \ell_{l,\tau}(s),$$
$$\tau = \left[\left(e^{\frac{\pi}{tl}} - 1\right)^{-1} + \left(1 - e^{\frac{-\pi}{tl}}\right)^{-1}\right] \text{ if } l \geq 2 \text{ for } h_{l,\tau}(s) \text{ and } \bar{h}_{l,\tau}(s). \tag{4}$$

The function $\eta_{l,n}(s)$ needs no *tau* vector since it converges.

3. The vector series $\zeta_n(s)$, $\ell_{l,n}(s)$, $h_{l,r}(s)$ and $\bar{h}_{l,r}(s)$ each have proximal and distal parts separated at a term designated *kappa*. For example, in $\zeta_n(s)$ an m for which $m = \kappa$, separates *proximal* values of m for which $m < \kappa$, from *distal* values of m for which $m > \kappa$. *Proximal* and *distal* parts of $\mathrm{P}(\zeta_\tau(s))$ are similarly separated by the vector $\vec{m}$ for which $m = \kappa$, and which is designated $\vec{\kappa}$. *Kappa* $\in \mathbb{N}$ is defined as

$$\kappa := \left[\tfrac{1}{2}\left(\left(e^{\frac{2\pi}{t}} - 1\right)^{-\frac{1}{2}} + \left(1 - e^{\frac{-2\pi}{t}}\right)^{-\frac{1}{2}}\right)\right], \tag{5}$$

with a random tie-breaking rule applied. There are similar *kappa* vectors at the end of the proximal series $\ell_{l,\kappa}(s)$ having vector $\vec{\mathcal{L}}_\kappa$, and the proximal series $h_{l,\kappa}(s)$ having vector $\vec{\mathcal{R}}_\kappa$. In $\eta_{l,n}(s)$ an m for which $m = \kappa l$, separates *proximal* values of m for which $m < \kappa l$, from *distal* values of m for which $m > \kappa l$, when $l > \kappa$.

4. A residual, *kappa dot* written $\dot{\kappa} \in \mathbb{R}$, with $-\frac{1}{2} < \dot{\kappa} < \frac{1}{2}$ is simply,

$$\dot{\kappa} := \frac{1}{2}\left(\left(e^{\frac{2\pi}{t}} - 1\right)^{-\frac{1}{2}} + \left(1 - e^{\frac{-2\pi}{t}}\right)^{-\frac{1}{2}}\right) - \kappa. \tag{6}$$

Kappa dot has a relationship with the fractional intersection of the *kappa* vectors $\vec{\mathcal{L}}_\kappa$ and $\vec{\mathcal{R}}_\kappa$ of at the non-trivial zeros. The fractional intersection of the *kappa* vectors is $0 < x \leq 1$.

5. A function $\theta(s)$ represents a "focal point" in the final pseudo-convergence of an ultimately diverging series. Using *tau*, the point of final pseudo-convergence in Euler's *zeta* is considered to be at either

$$\theta(s) = \tfrac{1}{2}\left(\zeta_\tau(s) + \zeta_{\tau+1}(s)\right) \text{ or } \theta(s) = \tfrac{1}{2}\left(\zeta_\tau(s) + \zeta_{\tau-1}(s)\right). \tag{7}$$

This average is implied when the formulation $\zeta_\tau(s)$ is used, but this averaging does not apply when $\zeta_n(s)$ entertains values of $n \neq \tau$. Related, but more involved, averaging is applicable for $h_{l,\tau}(s)$, but once more the formulation $h_{l,\tau}(s)$ is considered to imply that "focal point" in the final pseudo-convergence rather than the point $h_{l,\tau}(s)$ itself.

6. An integer l identifies every l^{th} term in a vector series. This allows a different rule to apply to the magnitude or argument of the l^{th} vectors. Euler's *zeta* is assigned a value of $l = 1$, since every term is treated the same as its neighbours.

7. The modified *eta* function $\eta_l(s)$ is derived for $l \in \{2, 3, 4 \ldots\}$ so that it shares zeros with Riemann's *zeta*: $\eta_l(s) = (1 - l^{1-s})\zeta(s)$. The function $\eta_l(s)$ has a partial form to n terms,

$$\eta_{l,n}(s) = \sum_{m=1}^{n} jm^{-s}$$
$$\text{with } j = 1 \text{ when } l \nmid m \text{ and } j = (1 - l) \text{ when } l|m. \tag{8}$$

The partial series in vector format is as a series of $\vec{m}$ with j reassigned

$$\eta_{l,n}(s) = \sum_{m=1}^{n} \vec{m},$$
$$|\vec{m}| = jm^{-\sigma} \text{ and } \arg(\vec{m}) = -t\ln(m) + \phi:$$
$$\text{with } j = 1 \text{ and } \phi = 0 \text{ when } l \nmid m,$$
$$\text{and } j = (l - 1) \text{ and } \phi = \pi \text{ when } l|m. \tag{9}$$

8. The partial series to κl terms is specifically considered to be

$$\eta_{l,\kappa l}(s) := \zeta_{\kappa l}(s) - l\sum_{n=1}^{\kappa}(ln)^{-s}. \tag{10}$$

When $l > \kappa$ the symmetries in $\mathrm{P}(\eta_l(s))$ are overt, and when $l \approx \left\lfloor\frac{\tau}{\kappa}\right\rfloor$ and $s \in \{\rho_i\}$ the term $\zeta_{\kappa l}(s) \approx 0$. It is argued in this paper that when $l \approx \left\lfloor\frac{\tau}{\kappa}\right\rfloor$ and $s \in \{\rho_u\}$ then the term $\zeta_{\kappa l}(s) \approx 0$.

9. In relation to $\eta_l(s)$, a function $\mathcal{m}(q)$ determines important values of $m = \mathcal{m}(q)$, with $q \in \mathbb{N}$

$$\mathcal{m}(q) := \left\lfloor\frac{1}{2}\left(\left(e^{\frac{q\pi}{lt}} - 1\right)^{-1} + \left(1 - e^{\frac{-q\pi}{lt}}\right)^{-1}\right)\right\rfloor. \tag{11}$$

10. An ordered set R_l has elements $q_r \in \mathbb{N}$. Using "\" to mean the set theoretic difference, R_l is defined for $l \geq 2$ and has elements indexed by r,

$$\mathrm{R}_l = \{q_r\} = \{\{q: 2|(q+1)\}, \{q: 2l|q\}\} \setminus \{\{q: 2l|(q+1) \text{ or } 2l|(q-1)\}\}. \tag{12}$$

This rule generates $\mathrm{R}_l = \mathbb{O}$ when $l \to \infty$, a position we require for Euler's *zeta*, which is in many ways appropriate, however, Euler's *zeta* is already associated with $l = 1$.

11. For Euler's *zeta* when $l = 1$ we have $\mathrm{R}_1 = \mathbb{O}$.

12. The point which best represents a structural change related to q is an average of two l^{th} vectors in the pathway $\mathrm{P}(\eta_l(s))$ near q, for any specified l, and is defined as *eta* hat $\hat{\eta}_q(s)$;

$$\hat{\eta}_q(\mathrm{s}) := \frac{1}{4}\left(\eta_{l,a-1}(\mathrm{s}) + \eta_{l,a}(\mathrm{s}) + \eta_{l,b-1}(\mathrm{s}) + \eta_{l,b}(s)\right)$$
$$\text{with } a = l\lfloor\mathcal{m}(q)/l\rfloor \text{ and } b = l(\lfloor\mathcal{m}(q)/l\rfloor + 1). \tag{13}$$

13. An $\mathcal{R}_r$ structure is a set of vectors $\{\vec{m}\}$ such that

$$\mathcal{R}_r := \left\{\vec{m} : \left\lfloor\left(e^{\frac{q_r\pi}{lt}} - 1\right)^{-1}\right\rfloor > m \geq \left\lfloor\left(e^{\frac{(q_{r+1})\pi}{lt}} - 1\right)^{-1}\right\rfloor\right\} \quad r \in \mathbb{N},\ q_r \in \mathrm{R}_l, \tag{14}$$

with a *principal-axis* which runs between $\hat{\eta}_{q_r}(\mathrm{s})$ and $\hat{\eta}_{q_{r+1}}(\mathrm{s})$. The *principal-axis* of an $\mathcal{R}_r$ structure preserves its orientation under changes in σ. The final and largest structure in the pathway is $\mathcal{R}_1$, whose *principal-axis* has magnitude $\sqrt{l}$ when $\sigma = \frac{1}{2}$.

14. The tangent to a smooth curve following the distal pathway of $\mathrm{P}(\eta_l(s))$ within an $\mathcal{R}_r$ has a *point-of-inflection* when the curve changes from a clockwise to an anticlockwise progression. This tangent bisects the *principal-axis* crossing it at an acute angle of $\frac{\pi}{4}$.

15. A real number ν, locates the *point-of-inflection* in the pathway of the final paired pseudo-spiral superstructure $\mathcal{R}_1$ of $\mathrm{P}\big(\eta_l(s)\big)$ thus

$$\nu := \frac{1}{2}\left(\left(e^{\frac{2\pi}{tl}} - 1\right)^{-1} + \left(1 - e^{\frac{-2\pi}{tl}}\right)^{-1}\right). \tag{15}$$

16. The *point-of-inflection* in an $\mathcal{R}_r$ structure is identified by the r^{th} element of the ordered set $\chi_l = \{q_{\bar{r}}\}$, which contains even values of q but when $l \geq 2$ excludes those values where $2l|q$;

$$\begin{gathered}\chi_l = \{q_{\bar{r}}\} = \{q\colon 2|q, q > 0\} \setminus \{q\colon 2l|q\} \quad \text{for } l \geq 2,\\ \chi_1 = \{q_{\bar{r}}\} = \{q\colon 2|q, q > 0\} = \mathbb{E} \quad \text{for Euler's } zeta.\end{gathered} \tag{16}$$

17. A vector $\vec{\mathcal{R}}_r$, which represents the magnitude of the *principal-axis* of an $\mathcal{R}_r$ structure is an object in its own right and has magnitude $\left|\vec{\mathcal{R}}_r\right|$ being

$$\left|\vec{\mathcal{R}}_r\right| = \sqrt{l}\,\nu^{\left(\frac{1}{2}-\sigma\right)}\left(\frac{q_{\bar{r}}}{2}\right)^{(\sigma-1)} \quad \text{with } q_{\bar{r}} \in \chi_l, \tag{17}$$

and after taking the nearest integer $\left[\frac{\nu}{l}\right]$, the vector has an argument

$$\arg\left(\vec{\mathcal{R}}_r\right) = \frac{\pi}{4} - t\ln\left(\frac{2l}{q_{\bar{r}}}\left[\frac{\nu}{l}\right]\right). \tag{18}$$

18. A series $\bar{h}_{l,\tau}(s)$ summing the $\vec{\mathcal{R}}_r$ with $q_{\bar{r}} \in \chi_l$ to *tau* terms for all $l \geq 2$ has a relationship with $\eta_l(s)$, and is defined as;

$$\bar{h}_{l,\tau}(s) := \sum_{r=1}^{\tau} \vec{\mathcal{R}}_r \quad \text{with } \vec{\mathcal{R}}_r \text{ following } q_{\bar{r}} \in \chi_l. \tag{19}$$

At a non-trivial zero the function $\bar{h}_{l,\tau}(s)$ after its *kappa* vector $\vec{\mathcal{R}}_\kappa$ follows the proximal part of $\mathrm{P}(\eta_l(s))$. The final pseudo-convergence can be refined from the point $\bar{h}_{l,\tau}(s)$ to an average of points near $\bar{h}_{l,\tau}(s)$ using $\theta(s)$ again. Once more this averaging is a nicety and of no real material importance other than for calculations and illustrations;

$$\begin{gathered}\theta(s) = \tfrac{1}{4}\big(\bar{h}_{l,a-1}(\mathrm{s}) + \bar{h}_{l,a}(\mathrm{s}) + \bar{h}_{l,b-1}(\mathrm{s}) + \bar{h}_{l,b}(s)\big)\\ \text{with } a = l\lfloor\tau/l\rfloor \text{ and } b = l\lceil\tau/l\rceil.\end{gathered} \tag{20}$$

19. The term *proximal* refers to the early vectors of a pathway and *distal* to the later. Since $\mathrm{P}\big(\bar{h}_{l,\tau}(s)\big)$ runs counter to $\mathrm{P}(\eta_l(s))$ at zeros, what is proximal for one pathway is distal for the other.

20. When $r < l$ a vector $\vec{\mathcal{R}}_r$ has a simpler magnitude since $\frac{q_{\bar{r}}}{2} = r$ giving

$$\left|\vec{\mathcal{R}}_r\right| = \sqrt{l}\,\nu^{\left(\frac{1}{2}-\sigma\right)} r^{(\sigma-1)}, \tag{21}$$

and a simpler argument

$$\arg\left(\vec{\mathcal{R}}_r\right) = \frac{\pi}{4} - t\ln\left(\frac{l}{r}\left[\frac{\nu}{l}\right]\right). \tag{22}$$

It is noted that for all $r < l$, when $\sigma = 1$ the $\left|\vec{\mathcal{R}}_r\right| = \sqrt{l/\nu}$, and when $\sigma = \frac{1}{2}$ the $\left|\vec{\mathcal{R}}_r\right| = \sqrt{l/r}$, and when $\sigma = 0$ the $\left|\vec{\mathcal{R}}_r\right| = \frac{\sqrt{l\nu}}{r}$.

21. A series to $\mathscr{r}$ terms $h_{l,\mathscr{r}}(s)$, having a relationship to Euler's *zeta* and to $\eta_l(s)$ when $\mathscr{r} < l$ is defined as;

$$h_{l,\mathscr{r}}(s) := \sum_{r=1}^{\mathscr{r}} \vec{\mathcal{R}}_r \quad \text{with } \vec{\mathcal{R}}_r \text{ following } q_{\bar{r}} \in \mathbb{E}. \tag{23}$$

22. It is noted that $\mathrm{P}\left(\bar{h}_{l,a}(s)\right) = \mathrm{P}\left(h_{l,a}(s)\right)$ if $a < l$.

23. Likewise the series $h_{l,\kappa}(s)$ to *kappa* terms is applicable to Euler's *zeta* and to $\eta_l(s)$ if $\kappa < l$;

$$h_{l,\kappa}(s) = \sum_{r=1}^{\kappa} \vec{\mathcal{R}}_r \quad \text{with } \vec{\mathcal{R}}_r \text{ following } q_{\bar{r}} \in \mathbb{E} \text{ if } \kappa < l. \tag{24}$$

24. A finite series of vectors indexed by $\mathscr{n}$ and summated to $\mathfrak{n}$ terms is

$$\ell_{l,\mathfrak{n}}(s) := -l^{(1-s)} \sum_{\mathscr{n}=1}^{\mathfrak{n}} \mathscr{n}^{-s} = \sum_{\mathscr{n}=1}^{\mathfrak{n}} \vec{\mathcal{L}}_{\mathscr{n}}. \tag{25}$$

The notation $\mathfrak{n}$ for the final term is analogous to $\mathscr{r}$ and n for other series in this paper. However, this series is principally needed to *kappa* terms and so $\ell_{l,\kappa}(s)$ is;

$$\ell_{l,\kappa}(s) = -l^{(1-s)} \sum_{\mathscr{n}=1}^{\kappa} \mathscr{n}^{-s} = \sum_{\mathscr{n}=1}^{\kappa} \vec{\mathcal{L}}_{\mathscr{n}}, \tag{26}$$

$$\text{with } \vec{\mathcal{L}}_{\mathscr{n}} = -l^{(1-s)}\mathscr{n}^{-s}. \tag{27}$$

The function $\ell_{l,\tau}(s)$ has a final pseudo-convergence before diverging that can be considered to be at τ as defined for Euler's *zeta*.

25. In the case of Euler's *zeta* $\zeta_\tau(s)$, matched vectors $\vec{\mathscr{m}}$ from $\mathrm{P}(\zeta_\kappa(s))$, and $\vec{\mathcal{R}}_{\mathscr{r}}$ from $\mathrm{P}\left(h_{1,\kappa}(s)\right)$ have mirror-image arguments about a common line of reflection but their magnitudes, which equate when $\sigma = \frac{1}{2}$ differ when $\sigma \neq \frac{1}{2}$.

26. In the case of $\eta_l(s)$, if $l > \kappa$ then matched vectors $\vec{\mathcal{L}}_{\mathscr{n}}$ from $\ell_l(s)$, and $\vec{\mathcal{R}}_{\mathscr{r}}$ from $h_l(s)$ have mirror-image arguments as far as the *kappa* vectors $\vec{\mathcal{L}}_\kappa$ and $\vec{\mathcal{R}}_\kappa$. Once more, the magnitudes, which equate when $\sigma = \frac{1}{2}$ differ when $\sigma \neq \frac{1}{2}$.

27. If $l > \kappa$ and the overlap of the *kappa* vectors $\vec{\mathcal{L}}_\kappa$ and $\vec{\mathcal{R}}_\kappa$ is accounted for with $0 < x < 1$ then

$$\eta_l(s) = \zeta_{\kappa l}(s) + \ell_{l,\kappa-1}(s) + x\vec{\mathcal{L}}_\kappa - \left(h_{l,\kappa-1}(s) + x\vec{\mathcal{R}}_\kappa\right). \tag{28}$$

The symmetries between $\mathrm{P}\left(\ell_{l,\kappa}(s)\right)$ and $\mathrm{P}\left(h_{l,\kappa}(s)\right)$ are now overt, but $\zeta_{\kappa l}(s)$ introduces a small asymmetry. Fortunately, near the non-trivial zeros the term $\zeta_{\kappa l}(s)$ can be ignored leaving the symmetries fully exposed. This is best satisfied with $l = \left[\frac{\tau}{\kappa}\right]$ when $\zeta_\tau(\rho) \approx 0$.

28. The line of reflection ψ, has an unspecified magnitude but an argument of

$$\arg(\psi) = -\tfrac{t}{2}\ln\left(l^2\left\lfloor\tfrac{\nu}{l}\right\rfloor\right) - \tfrac{3\pi}{8} \text{ if } l \geq 2 \tag{29}$$

and

$$\arg(\psi) = \tfrac{5\pi}{8} - \tfrac{t}{2}\ln([\nu]) \text{ if } l = 1, \text{ for Euler's } \textit{zeta}. \tag{30}$$

29. A function $\lambda_l(s,x)$, which is essentially a modified *eta* function that is agnostic of $\zeta_\tau(s)$, has zeros which are remarkably close to the non-trivial zeros of Riemann's *zeta* function

$$\lambda_l(s,x) := \ell_{l,\kappa-1}(s) + x\vec{\mathcal{L}}_\kappa - \left(h_{l,\kappa-1}(s) + x\vec{\mathcal{R}}_\kappa\right), \tag{31}$$

and with a minor adjustment to the magnitudes of the *kappa* vectors through $x = f(t)$ those zeros can be understood to equate with $\{\rho\}$.

30. The symmetry breaking in $\lambda_l(s,x)$ either side of $\mathrm{Re}(s) = \frac{1}{2}$ limits the non-trivial zeros to the critical-line in support of RH. It then follows by elementary calculus that the pathways for the zeros of the derivative are limited to the right of the critical-line adding further support.

31. A $\mathrm{P}(\eta_l(s))$ capable of producing a ρ_{u_α} and a ρ_{u_β} would have to be able to do so far all l. An asymmetry is required to produce a loop with a double-point in $\eta_l(s)$, and those loops are necessarily sensitive to changes in l. The sensitivity of loops in $\eta_l(s)$ to changes in l is yet further support for RH.

2.4. The graphical context for this work

The modified *eta* function $\eta_l(s)$ can be plotted as $\eta_l(\sigma)$ for fixed t, and as $\eta_l(t)$ for fixed σ, and provides a context for imagining the mechanisms required if RH is not true.

Figure 2(a) shows hypothetical plots of curves related to ρ_u for a t_u, σ_α and σ_β. If there is a ρ_u which disproves RH there has to be a loop in $\eta_l(\sigma)$ for fixed $t = t_u$, something like the loop shown in black. Crossing this loop at right angles, as prescribed by the partial differentials $\frac{\partial \eta_l(s)}{\partial \sigma} = -i\frac{\partial \eta_l(s)}{\partial t}$, and passing in almost opposite directions are the two curves $\eta_l(t)$ for fixed σ_α and $\eta_l(t)$ for fixed σ_β. The red curve is the true cycloid-like curve in $\eta_l(t)$ for fixed σ_c, which would meet a true cycloid-like curve $\eta_l(\sigma)$ for fixed t_c, which is not shown. The cycloids meet at $\eta_l(\sigma_c + it_c)$, indicated with a red square, and $\eta'_l(\sigma_c + it_c) = 0$ with $\sigma_\beta - \sigma_c > \sigma_c - \sigma_\alpha$. This is the challenge for the differential requiring it to have a zero to the left of the critical-line.

The graph also gives context to that which seems impossible: if RH is to fail then a loop in $\eta_l(\sigma)$ must exist that would be stable under changes in l.

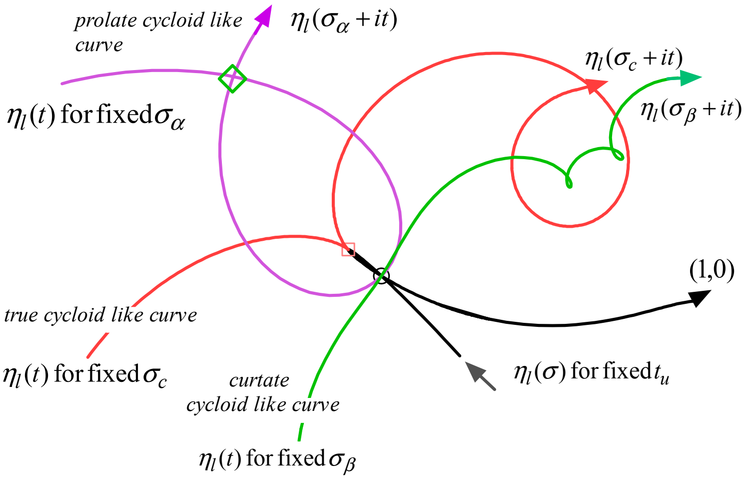

Figure 2. A curve in $\eta_l(\sigma)$ for fixed t_u in black, has a loop, and a double-point in the small black circle where $\eta_l(\sigma_\alpha + it_u) = \eta_l(\sigma_\beta + it_u) = 0$. A prolate cycloid-like curve in $\eta_l(t)$ for fixed σ_α in purple has a double-point $\eta_l(\sigma_\alpha + it_a) = \eta_l(\sigma_\alpha + it_b)$ in a green diamond. A curtate cycloid-like curve for $\eta_l(t)$ for fixed σ_β is shown in green. The true cycloid-like curve $\eta_l(\sigma_c + it)$ lies near the tip of the loop and has a zero differential at $\eta_l(\sigma_c + it_c)$ indicated with a red square.

It is important to appreciate how pathway changes secondary to a rising $\mathrm{Re}(s)$ can bring about a curve in $\eta_l(\sigma)$ and so a loop in $\eta_l(\sigma)$. A loop which satisfies Equation (2) is required for RH to fail. Curves capable of forming loops in $\eta_l(\sigma)$ as $\mathrm{Re}(s)$ rises are solely a consequence of pathway metamorphosis secondary to the differential change in the magnitude of the vectors along the pathway in a proximo-distal direction. In Figure 3(a) three pathways for $\mathrm{P}(\eta_l(s))$ are shown for $\sigma = \frac{1}{2}$ in black, $\sigma = \frac{7}{10}$ in red and $\sigma = 1$ in blue, with the curve $\eta_l(\sigma)$ in green. The curve $\eta_l(\sigma)$ for t_{632} passes through zero when $\sigma = \frac{1}{2}$ and then heads towards (1,0) for larger values of σ. There is no loop in Figure 3(a), but the mechanisms underlying looping are clear.

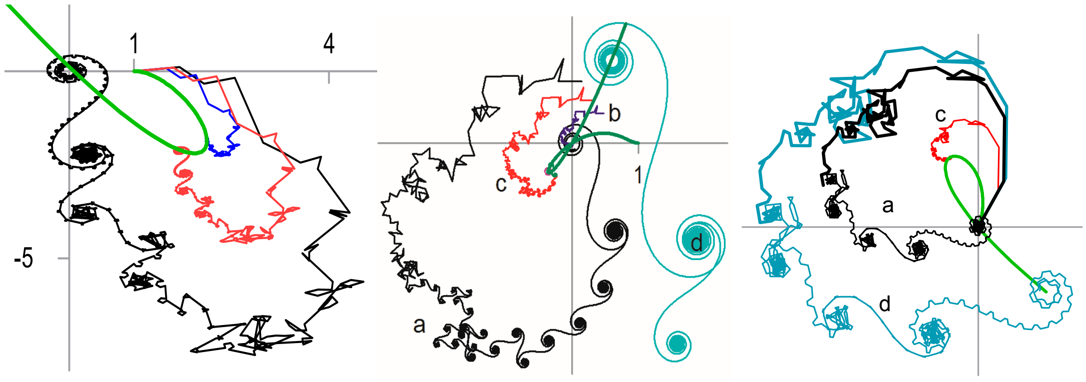

(a) (b) (c)

Figure 3. (a) The pathways $\mathrm{P}(\eta_3(\sigma + it_{632}))$ for three values of σ showing the proximo-distal "shrinkage" of the pathway as σ rises. Matched vectors are parallel but "shrinkage" is greater at

doi:10.20944/preprints201703.0121.v1

higher values of m as σ rises. A plot of $\eta_3(\sigma)$ in green is shown for fixed t. There is no loop or double-point but the mechanism underlying looping is evident. **(b)** and **(c)** hypothetical loops for a ρ_u formed by the same proximo-distal "shrinkage" gradient see text for detail.

Figure 3 panels (b) and (c) show two hypothetical loops in $\eta_l(\sigma)$ in green for two ρ_u. Pathway (a) in black is for $\rho_u = \sigma_\alpha + it_u$, pathway (b) in blue is for $\rho_u = \sigma_\beta + it_u$ (shown in the centre panel only), and pathway (c) in red is for a value of σ satisfying $\sigma_\alpha < \sigma < \sigma_\beta$. Pathway (d) in light blue is for a value of σ satisfying $\sigma < \sigma_\alpha$. Figure 3(b) and Figure 3(c) illustrate how the proximo-distal gradient of "shrinkage" of the pathway on rising σ can create a loop.

It is not clear how a double-loop with a triple-point could be created by such a mechanism since there are only two phenomena acting: (1) pathway layout and (2) the proximo-distal gradient. A double-loop and triple-point have to be capable of being generated if RH is not true. This corollary of RH will be discussed below.

The behaviour of $\zeta(s)$, and therefore the existence of its non-trivial zeros, is intimately linked to the non-trivial zeros of $\eta_l(s)$, and has a deterministic link to a set of sequential integers whose cardinality rises gently with the $\mathrm{Im}(\rho)$. The mechanics of this determinism follow directly from the relationship between neighbouring vectors $\vec{m}$ and $\overrightarrow{m+1}$ as far as the κl vector.

3. Results

The results are presented in 8 sections with further results and illustrations in Appendix A.

3.1. The series $\eta_l(s)$, the partial series $\eta_{l,n}(s)$ and the complimentary pathways
3.2. A partial Euler's zeta function with a complex domain has two roles
3.3. The pathway to convergence for Dirichlet's eta function
3.4. The $\mathcal{M}_m$ structures in the distal $\mathrm{P}\left(\bar{h}_{l,r}(s)\right)$ and the $\mathcal{L}_n$ structures in the distal $\mathrm{P}\left(\ell_{l,n}(s)\right)$
3.5. Symmetry-breaking in $\eta_l(s)$
3.6. The function $\lambda_l(s,x)$ identifies short intervals in t capable of hosting non-trivial zeros
3.7. Simultaneous zeros for $\eta_l(s)$: a metaphor for a ρ_u
3.8. The derivatives of $\eta_l(s)$ and of the related series $h_{l,r}(s)$, $\ell_{l,n}(s)$ and $\zeta_{l,\kappa l}(s)$

3.1. The series $\eta_l(s)$, the partial series $\eta_{l,n}(s)$ and the complimentary pathways

Starting with $\zeta(s) = \sum_m^\infty m^{-s}$, a modified Dirichlet *eta* function is derived through multiplication by l^{1-s} which is then subtracted from $\zeta(s)$ to give a series with every l^{th} term negated and multiplied by $(l-1)$,

$$\zeta(s) - l^{1-s}\zeta(s) = 1 + 2^{-s} + 3^{-s} + \cdots - (l-1)l^{-s} + \cdots - (l-1)(2l)^{-s} + \cdots - (l-1)(3l)^{s} + \cdots.$$

Then if $\eta_l(s) := 1 + 2^{-s} + 3^{-s} + \cdots - (l-1)l^{-s} + \cdots - (l-1)(2l)^{-s} + \cdots - (l-1)(3l)^{s} + \cdots$,

it can then be seen that, since

$$\eta_l(s) = (1 - l^{1-s})\zeta(s), \tag{32}$$

$\eta_l(s)$ will share its non-trivial zeros with $\zeta(s)$. Though Riemann's *zeta* function has a pole at $s = 1$ it is noted that $\eta_l(s)$ can have a domain with $\mathrm{Re}(s) = 1$.

Returning to the modified *eta* function we have a partial series $\eta_{l,n}(s)$ being simply

$$\eta_{l,n}(s) := \sum_{m=1}^{n} jm^{-s}$$
$$\text{with } j = 1 \text{ when } l \nmid m \text{ and } j = (1-l) \text{ when } l|m, \tag{33}$$

and the domain in $\eta_{l,n}(s)$ can receive $s = \sigma + it$ to give, using Euler's formula,

$$\eta_{l,n}(s) = \sum_{m=1}^{n} jm^{-s} = \sum_{m=1}^{n} jm^{-\sigma}(\cos(t\ln(m)) - i.\sin(t\ln(m))), \tag{34}$$

with j as above.

From this formulation the point $\eta_{l,n}(s)$ is reached after n vectors, indicated $\vec{m}$, as follows

$$\eta_{l,n}(s) = \sum_{m=1}^{n} \vec{m} \tag{35}$$

$$\text{with } |\vec{m}| = m^{-\sigma} \text{ when } l \nmid m \text{ and } |\vec{m}| = (l-1)m \text{ when } m|l$$
$$\text{with } \arg(\vec{m}) = -t\ln(m) \text{ when } l \nmid m \text{ and } \arg(\vec{m}) = \pi - t\ln(m) \text{ when } m|l.$$

The pathway $\mathrm{P}\left(\eta_{l,n}(s)\right)$ is then the operation of plotting those n vectors in the Argand plane.

3.1.1. The pathway $P(\eta_2(s))$, the index r, $P(\zeta_n(s))$ and other series

The orientation of neighbouring $\vec{m}$ in $\mathrm{P}(\eta_2(s))$ going forward sees a vector at $(m+1)$ of length $(m+1)^{-\sigma}$ lying in relation to an m^{th} vector of length $m^{-\sigma}$ at an angle of $\vartheta = t\ln\left(\frac{m+1}{m}\right)$ with a reduced form θ,

$$\theta = \vartheta - 2\pi(r-1) \text{ where } r \in \mathbb{N}, \text{ for } \mathrm{P}\left(\eta_{l,n}(s)\right) \text{ or } \mathrm{P}(\zeta_n(s)) \tag{36}$$

with r chosen so that $0 < \theta \leq 2\pi$. In Figure 4(a) a cartoon shows a pathway a little after the *point-of-inflection* when $r = 1$ and $\vartheta = \theta$ at a value a little less than π. As m rises, the path encloses irregular polygons with a gradually reducing number sides before triangles are formed (see Figure 4(b)) which narrow and shorten as the vectors repeatedly double-back on themselves.

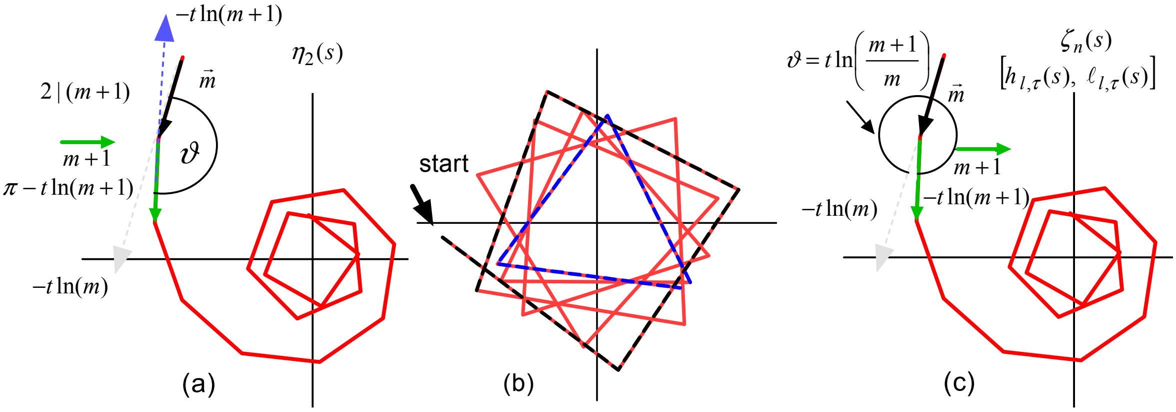

Figure 4. (a) A final pseudo-spiral in $\eta_2(s)$ is shown beginning when $\vartheta < \pi$. **(b)** Later vectors on the same path are shown much enlarged, with a quadrilateral (black and red) first appearing when $\vartheta < \frac{\pi}{2}$ and then later still a triangular path is about to appear as ϑ approaches $\frac{\pi}{6}$. The blue and red path is the last quadrilateral having a very short final side so that it appears almost triangular. **(c)** For comparison a few $\vec{m}$ in the last pseudo-spiral before divergence in $\zeta_n(s)$ beginning when $\vartheta < 2\pi$.

In Figure 4(c) the cartoon is used to illustrate the final pseudo-convergence of $\mathrm{P}(\zeta_n(s))$. This pathway has passed the *point-of-inflection* and $\vartheta = \theta$ is a little less than 2π. When $\vartheta = \theta$ falls to π the *tau* vector is found, and thereafter the final spiral of divergence is entered.

The cartoon in Figure 4(c) would also apply if the $\vec{m}$ were replaced with $\vec{\mathcal{R}}_r$ or $\vec{\mathcal{L}}_n$ and we had their superstructures $\mathcal{M}_m$ and $\mathcal{L}_m$ indexed by m.

$$\theta = \vartheta - 2\pi(m-1) \text{ where } m \in \mathbb{N}, \text{ for } \mathrm{P}\left(h_{l,r}(s)\right) \text{ or } \mathrm{P}\left(\ell_{l,\tau}(s)\right). \tag{37}$$

Consideration is also given to $t\ln\left(\frac{m}{m-1}\right)$, which looks backwards, since this can be important at structural changes at low values of t and can affect some approximations. If in $\mathrm{P}(\zeta_n(s))$ the r associated with $t\ln\left(\frac{m}{m-1}\right)$ and that associated with $t\ln\left(\frac{m+1}{m}\right)$ differ by more than 1 then that m will be in the proximal pathway. That is if $t\ln\left(\frac{m^2-1}{m^2}\right) > 2\pi$ then $m < \left(1 - e^{\frac{-2\pi}{t}}\right)^{-1/2}$ and this of course is *kappa*, see Equation (5). The same applies to $h_{l,r}(s)$ and $\ell_{l,\mathrm{n}}(s)$.

The distal pathway has a set of vectors forming a superstructure for each r since neighbouring pairs of $\vec{m}$ share the same value of r. These superstructures have a stability under changes in σ. A superstructure, seen as m rising, has a smooth clockwise growing pseudo-spiral which unwinds before entering a straighter region which crosses the *principal-axis* at $\frac{\pi}{4}$, before entering a smooth anti-clockwise pseudo-spiral which winds in towards a pseudo-convergence or a final convergence in the case of $\eta_l(s)$.

Three examples using $\eta_2(\rho_i)$ are shown in Figure (5). The proximal pathways have a smaller number of much larger vectors than the distal pathways which have very many small vectors which form the superstructures. The $\mathcal{R}_1$ structures all have a *principal-axis* of magnitude $\sqrt{l}$, here sitting on a circle of radius $\sqrt{2}$. Note the paired pseudo-spirals have an anticlockwise unwinding followed by a clockwise pseudo-convergence.

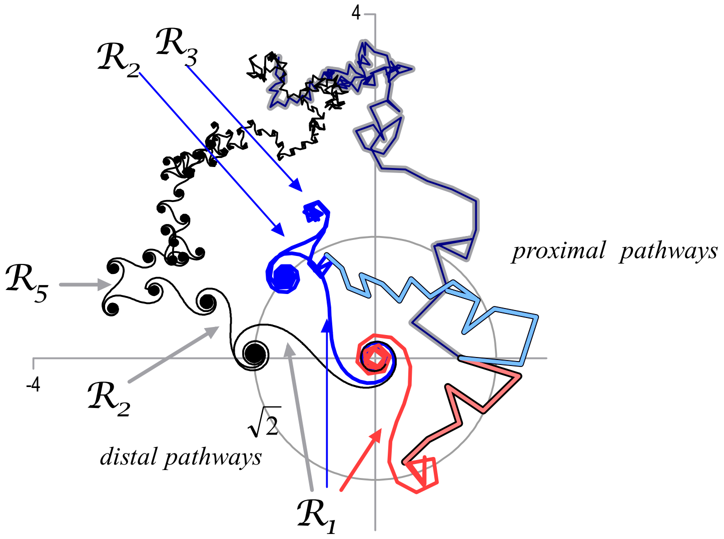

Figure 5. Pathways for $t_i = 59.347$ in red, $t_i = 376.324$ in blue and $t_i = 74920.8275$ the $100{,}000^{th}$ zero in black, all with $\sigma = \frac{1}{2}$. All pathways are shown starting from (1,0) omitting $\vec{1}$.

3.1.2. The $\mathcal{R}_r$ structures of $\eta_l(s)$ contain near regular polygons and star-polygons when $l > 2$

For $\mathrm{P}(\eta_l(s))$ when $l > 2$ the mechanism of convergence is subtly different and is illustrated in Figure 4, for $l = 5$ and $l = 23$. One consequence of the modification to Dirichlet's *eta* is that as l rises the final pseudo-spiral occurs at higher values of m. The final pseudo-spiral contains near regular polygons with one side missing.

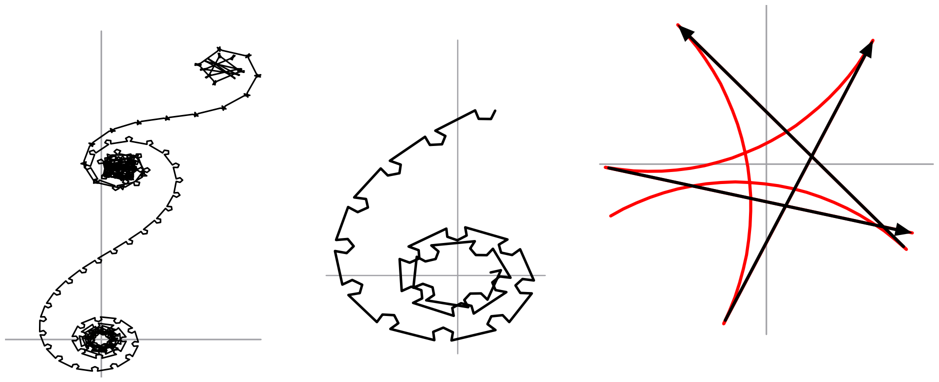
(a) (b) (c)

Figure 6. **(a)** The final paired pseudo-spirals of part of a $\mathrm{P}(\eta_5(s))$. **(b)** Detail from a similar pseudo-convergence showing near-regular pentagons with one side missing, made from 4

vectors that lie between each of the negated 5th vectors. **(c)** With $l = 23$, the mechanism of convergence can be appreciated as 22 vectors preceding convergence form smooth arcs (in red), followed by the larger negated returning vectors (in black): the arcs gradually reduce their curvature as infinity approaches.

In $\eta_l(s)$ when $l > 2$ there are near regular polygons and near regular star-polygons along the pathway $\mathrm{P}(\eta_l(s))$ whose number of sides relates to l. The polygons lie between the $\vec{m}$ vectors where $l|m$. The rules that apply when $l > 2$ are generalizable to $l = 2$. The index r falls as m rises. We proceed in stages using first $m(q) = f(r, l, t)$ to identify the points in a pathway at which significant geometric changes take place to the polygons. These changes lie near the pseudo-convergences and near the *points-of-inflection* that would be found in a smooth curve approximating to the pathway. Appendix A1 expands on the geometry at structural changes in pathways.

The difference in arguments between neighbouring $\vec{m}$ is $t\ln\left(\frac{m+1}{m}\right)$ looking forward and $t\ln\left(\frac{m}{m-1}\right)$ looking backwards. Important structural changes occur when neighbouring differences lie immediately either side of specific integral multiples of $\frac{\pi}{l}$. This follows from the geometry of the pathway. The integer q distinguishes significant m^{th} vectors, thus

$$t\ln\left(\frac{m+2}{m+1}\right) < \frac{q\pi}{l} \leq t\ln\left(\frac{m+1}{m}\right). \tag{38}$$

A function $m(q)$ determines important values of m, with $q \in \mathbb{N}$ such that $q \neq 0$;

$$m(q) := \left[\frac{1}{2}\left(\left(e^{\frac{q\pi}{lt}} - 1\right)^{-1} + \left(1 - e^{\frac{-q\pi}{lt}}\right)^{-1}\right)\right] \quad q \in \mathbb{N}. \tag{39}$$

We let Q_q designate a structural unit containing all points in the pathway $\mathrm{P}(\eta_l(s))$ between $m = m(q+1)$ and $m = m(q)$. Although we should not strictly included $q = 0$ we can give meaning to Q_0 by briefly allowing $q \in \mathbb{R}$ when $0 < q \leq 1$ since we recognise that the $\lim_{q\to 0}\left(e^{\frac{q\pi}{lt}} - 1\right)^{-1} = \infty$. To this end we can allow $q \in \mathbb{N}_0$ without loss of rigor or argument conscious of the limitations. Temporary meaning is given to Q_q as a set thus

$$Q_q = \{\vec{m} : m(q) > m \geq m(q+1)\} \quad \text{with } q \in \mathbb{N}_0. \tag{40}$$

The set $\mathrm{M}_l = \{m : m = m(q)\}$ are important points in the pathway $\mathrm{P}(\eta_l(s))$. The structural unit Q_q may be a substantial part of a paired pseudo-spiral $\mathcal{R}_r$ or a region that makes no substantial progress in the Argand plane but rather contains oscillations about a pseudo-convergence.

We now consider a partial series $\eta_{l,n}(s)$ ending near the centre of a pseudo-spiral with $m \in \mathrm{M}_l$. The end point of the final vector $\vec{m}$, with $m = n$ in the partial series $\eta_{l,n}(s)$ may not best represent the centre of the pseudo-spiral. This is evident in smaller pseudo-spiral pairs at low values of m and especially evident when $l \gg 2$, since $|\vec{m}|$ when $l|m$ is much greater than the magnitude of the preceding $(l-1)$ vectors and the subsequent $(l-1)$ vectors. For example if $l = 5$ the 100^{th} vector is longer than vectors 96 to 99 and longer than vectors 101 to 104.

An appropriate average to represent the region of the pathway $\mathrm{P}(\eta_l(s))$ at q (for a specified l) is defined as *eta* hat $\hat{\eta}_q(s)$;

$$\hat{\eta}_q(\mathrm{s}) := \frac{1}{4}\left(\eta_{l,a-1}(\mathrm{s}) + \eta_{l,a}(\mathrm{s}) + \eta_{l,b-1}(\mathrm{s}) + \eta_{l,b}(s)\right) \tag{41}$$
$$\text{with } a = l\lfloor m(q)/l\rfloor \text{ and } b = l(\lfloor m(q)/l\rfloor + 1).$$

An approximate start to Q_q is the point $\hat{\eta}_{q+1}(s)$ and an approximate end of Q_q is $\hat{\eta}_q(s)$. The point $\hat{\eta}_q(s)$ approximates to a point best representing the transition from one structure to the next.

Our next task is to recognise the geometric requirement that when $2l|q$ the neighbouring structures Q_{q-1} and Q_{q+1} will collapse and become pseudo-convergences within the region of a pseudo-spiral of $\mathcal{R}_r$. We can also state the following equivalence relation

$$\hat{\eta}_{(q-1)}(\mathrm{s}) \cong \hat{\eta}_q(s) \cong \hat{\eta}_{(q+1)}(s) \tag{42}$$

$$\text{when } \ l|2(q+1) \text{ or } l|2(q-1).$$

In practice convergence can be placed at $q = 1$ since $\eta_l(s) = \hat{\eta}_0(s) \cong \hat{\eta}_1(s)$ and pursuing $\eta_{l,n}(s)$ any further merely adds computational burden without benefit, see Figure 7. We can now comfortably revert to $q \in \mathbb{N}$ as we no longer require $q = 0$.

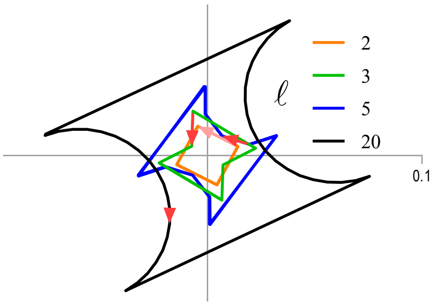

Figure 7. Vectors for $\mathrm{P}(\eta_l(s))$ for the 3000^{th} non-trivial zero near $q = 1$ with the $\vec{m}$ for $m = \mathcal{m}(1)$ indicated with an arrow for each of four different values of l. As can be seen the averaging of $\hat{\eta}_q(s) \cong 0$ when $q = 1$.

We now clarify the relationship between r and q which will depend on l and the geometry near each $\vec{m}$ when $m \in \mathrm{M}_l$. The mapping of an r onto a specific q is captured in the set $\mathrm{R}_l = \{q_1, q_2, q_3 \dots q_r \dots\}$ and is easily derived. The set R_l is not to be confused with the structure indicated with the scripted $\mathcal{R}_r$. For any value of $l \geq 2$ we take odd values of q, and the even values of q which satisfy $2l|q$. We then remove the odd values of q which lie either side of the values of q for which $2l|q$. We could include $q = 0$ since this specifies convergence, but are happy to accept $q_1 = 1$ in its place. We order this set as q rises and index the elements by $r \in \mathbb{N}$ and so generate $\mathrm{R}_l = \{q_1, q_2, q_3 \dots q_r \dots\}$. We can state R_l formally using "\" to mean the set theoretic difference, thus

$$\mathrm{R}_l = \{q_r\} = \big\{\{q: 2|(q+1)\}, \{q: 2l|q\}\big\} \setminus \{q: 2l|(q+1) \ or \ 2l|(q-1)\} \ \text{ with } q \in \mathbb{N}. \tag{43}$$

A few sets are illustrated below.

If $l = 2$ then $\mathrm{R}_2 = \{1, 4, 8, 12, 16, 20, 24, 28, 32 \dots\}$.
If $l = 3$ then $\mathrm{R}_3 = \{1, 3, 6, 9, 12, 15, 18, 21, 24 \dots\}$.
If $l = 4$ then $\mathrm{R}_4 = \{1, 3, 5, 8, 11, 13, 16, 19, 21, 24, 27, 29, 32, 35 \dots\}$.
If $l = 5$ then $\mathrm{R}_5 = \{1, 3, 5, 7, 10, 13, 15, 17, 20, 23, 25, 27, 30, 33 \dots\}$.

To incorporate Euler's *zeta* as a special case (rather than letting $l \to \infty$) we add that if $l = 1$ then $\mathrm{R}_1 = \{1, 3, 5, 7 \ \dots\} = \mathbb{O}$ and notice that the elements of R_l for $l \geq 2$ follow this pattern until the l^{th} term. With $q = 1$ Equation (39) gives $\mathcal{m}(q) = \tau$ for Euler's *zeta* which is appropriate.

The collapse of structures either side of $2l|q$ is shown in Appendix A2.

3.1.3. Two ways of counting structures: Q_q or $\mathcal{R}_r$: the sets R_l and χ_l

Distal structures in $\mathrm{P}(\eta_l(s))$ can be grouped as $\{Q_q\}$ or $\{\mathcal{R}_r\}$. The Q_q (Equation (40)) are indexed by q and $|Q_q| = \hat{\eta}_{q+1}(s) - \hat{\eta}_q(s)$ which may be very small when $l|2(q+1)$ or $l|2(q-1)$. In $\eta_l(s)$ each $\mathcal{R}_r$ has a *principal-axis* which have arguments and magnitudes related to the vector $\vec{\mathcal{R}}_r$. The *principal-axes* have end points $\hat{\eta}_{q_{r+1}}(s)$ and $\hat{\eta}_{q_r}(s)$ with $q_r \in \mathrm{R}_l$.

We now have all the $\vec{m}$ vectors in $\mathcal{R}_r$ with m in the specified interval using the floor function

$$\mathcal{R}_r := \left\{\vec{m} : \left\lfloor \left(e^{\frac{q_r \pi}{lt}} - 1\right)^{-1} \right\rfloor > m \geq \left\lfloor \left(e^{\frac{(q_{r+1})\pi}{lt}} - 1\right)^{-1} \right\rfloor \right\} \quad r \in \mathbb{N}, \ q_r \in \mathrm{R}_l. \tag{44}$$

The *principal-axis* of an $\mathcal{R}_r$ has a magnitude $|\Delta\hat{\eta}_{q_r}|$;

$$|\Delta\hat{\eta}_{q_r}| = |\hat{\eta}_{q_r}(\mathrm{s}) - \hat{\eta}_{q_{r+1}}(\mathrm{s})|. \tag{45}$$

Appendix A3 tabulates some ratios of $|\Delta\hat{\eta}_{q_r}|/|\Delta\hat{\eta}_{q_1}|$.

The centre or *point-of-inflection* in any $\mathcal{R}_r$ structure can be located with the r^{th} element of the ordered set $\chi_l = \{q_{\bar{r}}\}$, which contains even values of q but for $l \geq 2$ excludes those where $2l|q$;

$$\chi_l = \{q_{\bar{r}}\} = \{q: 2|q, q > 0\} \setminus \{q: 2l|q\}\ for\ l \geq 2, \tag{46}$$

$$\text{and } \chi_l = \mathbb{E} \text{ for Euler's } zeta\ l = 1.$$

The bar in $\bar{r}$, clarifies that the object carrying the subscript relates to the inflection or "middle" of the $\mathcal{R}_r$ structure and not to a pseudo-convergence. The elements are in a similar format to those of R_l;

$$\chi_l = \{q_{\bar{1}}, q_{\bar{2}}, q_{\bar{3}}, \dots q_{\bar{r}}, \dots\}.$$

If $l = 2$ then $\chi_2 = \{2, 6, 10, 14, 18, 22, 26, 30, \dots q_{\bar{r}}, \dots\}$.
If $l = 3$ then $\chi_3 = \{2, 4, 8, 10, 14, 16, 20, 22, 26, \dots q_{\bar{r}}, \dots\}$.
If $l = 4$ then $\chi_4 = \{2, 4, 6, 10, 12, 14, 18, 20, 22, 26, \dots q_{\bar{r}}, \dots\}$.
If $l = 5$ then $\chi_5 = \{2, 4, 6, 8, 12, 14, 16, 18, 22, 24, 26, 28, 32 \dots q_{\bar{r}}, \dots\}$ and so on.

For $l \geq 2$ we can also define $q_{\bar{r}}$ inductively as $q_{\bar{1}} = 2$ and then $q_{\overline{r+1}} = q_{\bar{r}} + 2$ if $2l \nmid (q_{\bar{r}} + 2)$ and $q_{\overline{r+1}} = q_{\bar{r}} + 4$ if $2l|(q_{\bar{r}} + 2)$.

The elements in the ordered set χ_l rise in increments of 2 until $l - 1$ terms have been reached, and so if $\kappa = l - 1$ we have

$$\left\{\frac{q_{\bar{r}}}{2} : for\ r < l\right\} = \{1, 2, 3, \dots l - 1\} = \{1, 2, 3, \dots \kappa\}.$$

The section above principally refers to $\eta_l(s)$ and so $l \geq 2$. To allow application in Euler's *zeta* we have $\chi_1 = \{2, 4, 6, 8, 10 \dots q_{\bar{r}} \dots\}$.

3.1.4. An example of an $\mathcal{R}_1$ structure and the $\arg(\vec{\mathcal{R}}_1)$

To proceed we need *nu,* the indicator of the *point-of-inflection* in $\mathcal{R}_1$ for any *t* and l;

$$\nu := \frac{1}{2}\left(\left(e^{\frac{2\pi}{tl}} - 1\right)^{-1} + \left(1 - e^{\frac{-2\pi}{tl}}\right)^{-1}\right). \tag{47}$$

Using $t = 740$ Figure 8 shows that the orientation of the $\vec{m}$ vectors, for which $l|m$, follow the principal part of the structure. It is noted that their magnitudes are $(l-1)m^{-\sigma}$. There are gaps between *neighbour*ing vectors for with $l|m$ which are filled by the near-regular polygons with one missing side.

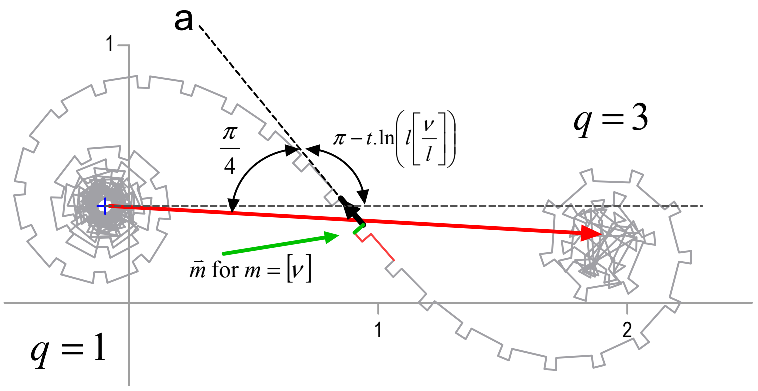

Figure 8. The paired pseudo-spirals of $\mathcal{R}_1$ for $t = 740$ and $\sigma = \frac{1}{2}$ with $l = 4$ are shown from $q = 3$ at $m = 314$ to $m = 942$ at $q = 1$. The red arrow is $\vec{\mathcal{R}}_1$.

In Figure 8. The short vector $\vec{m}$, with $m = \left[\left(e^{q\pi/tl} - 1\right)^{-1}\right]$ for $q = 2$ is shown in green at $m = 471$. This sits nearest the point-of-inflection. In general as here, such a vector may point in an unhelpful direction unless $l|m$. Its nearest neighbour $l\left[\frac{\nu}{l}\right]$, is shown in black at $m = 472$. Being near the point-of-inflection, this has an argument of $\pi - t\ln(l[\nu/l])$ which is a good estimate of the tangent to the curve (a). The tangent crosses the *principal-axis* at an acute angle of $\frac{\pi}{4}$. The vector $\vec{\mathcal{R}}_1$

in red with magnitude $\sqrt{4}$, has an orientation displaced by π from the sum of the two illustrated arguments thus $\arg(\vec{\mathcal{R}}_1) = \frac{\pi}{4} - t\ln(l[\nu/l])$, see Equation (22).

3.1.5. Comment on *nu*

Nu locates a vector which is nearly tangential to the *point-of-inflection* on a smooth curve following the pathway. The associated integer must satisfy $l|m$ else the vector could lie in the near-regular open polygon in $\mathrm{P}(\eta_l(s))$ and its relationship to the $arg(\vec{\mathcal{R}}_1)$ would be challenging to determine. Importantly, the larger t becomes the smoother the pathway $\mathrm{P}(\eta_l(s))$ is in the region and the closer the $arg(\vec{m})$ becomes to the tangent when $l|m$, and it is pretty good already at low values of t. Hence, the tangential vector is located by $l\left[\frac{\nu}{l}\right]$ and the $arg(\vec{\mathcal{R}}_1)$ becomes $\frac{\pi}{4} - t.\ln\left(l\left[\frac{\nu}{l}\right]\right)$; noting that the addition of π for when $l|m$, cancels with the π associated with $\vec{\mathcal{R}}_1$ being directed against the progress of the *principal-axis*.

Nu also separates proximal and distal parts within the $\mathcal{R}_1$ pathway. In $\mathcal{R}_1$ there are 3 times as many $\vec{m}$ in the distal part as in the proximal part. The proximal part has

$$\left(e^{\frac{3\pi}{tl}} - 1\right)^{-1} < m < \left(e^{\frac{2\pi}{tl}} - 1\right)^{-1} \tag{48}$$

and in the distal part has

$$\left(e^{\frac{2\pi}{tl}} - 1\right)^{-1} < m < \left(e^{\frac{\pi}{tl}} - 1\right)^{-1}, \tag{49}$$

and

$$\left(e^{\frac{\pi}{tl}} - 1\right)^{-1} - \left(e^{\frac{2\pi}{tl}} - 1\right)^{-1} \approx \frac{3}{1}\left(\left(e^{\frac{2\pi}{tl}} - 1\right)^{-1} - \left(e^{\frac{3\pi}{tl}} - 1\right)^{-1}\right). \tag{50}$$

In sequence, the ratios for the number of vectors in the distal to proximal parts of well recognisable $\mathcal{R}_r$ structures will be very close to $\frac{3}{1}, \frac{5}{3}, \frac{7}{5}, \frac{9}{7} \ldots \frac{2r+1}{2r-1}$, with the approximation being best with large t and small r.

3.1.6. The function $\bar{h}_{l,\mathscr{r}}(s)$: a partial series to $\mathscr{r}$ terms driven by $\frac{q_{\bar{r}}}{2}$

A vector $\vec{\mathcal{R}}_r$, with $r < \kappa$, shares a relationship with the *principal-axis* of an $\mathcal{R}_r$ superstructure made of many $\vec{m}$ vectors. Using *nu*, the vector $\vec{\mathcal{R}}_r$ has magnitude

$$\left|\vec{\mathcal{R}}_r\right| := \sqrt{l}\,\nu^{\left(\frac{1}{2}-\sigma\right)}\left(\frac{q_{\bar{r}}}{2}\right)^{(\sigma-1)} \text{ with } q_{\bar{r}} \in \chi_l. \tag{51}$$

Turning to the arguments of $\vec{\mathcal{R}}_r$, we have for $l \geq 2$

$$\arg\left(\vec{\mathcal{R}}_r\right) = \frac{\pi}{4} - t\ln\left(l\left[\frac{\nu}{l}\right]\right) + t\ln\left(\frac{q_{\bar{r}}}{2}\right). \tag{52}$$

Because $q_{\bar{r}}$, has a subscript r *bar*, and this is the distinguishing parameter for the vector, the *bar* is re-used as an accent in the function $\bar{h}_{l,\mathscr{r}}(s)$. The function $\bar{h}_{l,\mathscr{r}}(s)$, now summates a series of $\mathscr{r}$ vectors $\vec{\mathcal{R}}_r$, driven by the sequential terms $q_{\bar{r}}/2$, with $q_{\bar{r}} \in \chi_l$ up to $r = \mathscr{r}$ terms and defined as

$$\bar{h}_{l,\mathscr{r}}(s) := \sum_{r=1}^{\mathscr{r}} \vec{\mathcal{R}}_r \text{ with } q_{\bar{r}} \in \chi_l. \tag{53}$$

3.1.7. The function $h_{l,\mathscr{r}}(s)$: a partial series to $\mathscr{r}$ terms driven by r

This is simpler than $\bar{h}_{l,\mathscr{r}}(s)$. In appropriate circumstances Equations (51) and (52) can be simplified with important consequences.

Firstly, in Euler's *zeta* we have $l = 1$, and substitute $r = \frac{q_{\bar{r}}}{2}$ to give

$$\left|\vec{\mathcal{R}}_r\right| = \nu^{\left(\frac{1}{2}-\sigma\right)} r^{(\sigma-1)}, \quad \text{for } l = 1 \tag{54}$$

with the arguments of $\vec{\mathcal{R}}_r$ now being,

$$\arg\left(\vec{\mathcal{R}}_r\right) = \tfrac{5\pi}{4} + t\ln\left(\tfrac{r}{[\nu]}\right) \text{ for } l = 1. \tag{55}$$

The index r is now allowed to rise through the important point $r = \kappa$ to reach $r = \tau$. In Euler's *zeta* $\zeta_n(s)$, the index m runs to the important point $m = \kappa$ at the end of the vector $\vec{\kappa}$. In the region of a non-trivial zero the $\vec{\kappa}$ vector crosses ψ, the line of reflection (see below). If the pathway of Euler's *zeta* $\mathrm{P}\left(\zeta_\tau(s)\right)$ is considered after $\vec{\kappa}$, the small $\vec{\mathcal{R}}_r$ vectors soon form superstructures designated $\mathcal{M}_m$ before reaching $r = \tau$ which precedes overt commitment to divergence.

Secondly, for $l \geq 2$, we have $r = \frac{q_{\bar{r}}}{2}$ for all $r < l$ giving

$$\left|\vec{\mathcal{R}}_r\right| = \sqrt{l}\,\nu^{\left(\frac{1}{2}-\sigma\right)} r^{(\sigma-1)}, \tag{56}$$

with the arguments of $\vec{\mathcal{R}}_r$ having a phase shift of π in relation to Equation (55),

$$\arg\left(\vec{\mathcal{R}}_r\right) = \tfrac{\pi}{4} - t\ln\left(\frac{l}{r}\left[\frac{\nu}{l}\right]\right) \text{ when } r < l \text{ and } l \geq 2. \tag{57}$$

In both instances, i.e. for all l, we can define

$$h_{l,\mathcal{r}}(s) := \sum_{r=1}^{\mathcal{r}} \vec{\mathcal{R}}_r \tag{58}$$

for $l = 1$ in Euler's $zeta$ and for all $l \geq 2$ when $\mathcal{r} < l$.

It is now clear that if an l is selected satisfying $\kappa < l \leq \left[\frac{\tau}{\kappa}\right]$ and $\mathcal{r} = \kappa$, the symmetries will be overt. It is observed that $h_{l,a} = \bar{h}_{l,a}$ whenever $a < l$.

If there is a non-trivial zero and $\mathcal{r} = \tau$ and $l > \kappa$ then the pathway $\mathrm{P}\left(\bar{h}_{l,\tau}(s)\right)$ after $\bar{h}_{l,\kappa}(s)$, which is its distal part, lies superimposed upon the proximal part of $\mathrm{P}\left(\eta_l(s)\right)$ namely $\mathrm{P}\left(\eta_{l,\kappa}(s)\right)$. It is important to appreciate that $\mathrm{P}\left(\bar{h}_{l,\tau}(s)\right)$ after $\bar{h}_{l,\kappa}(s)$ does not track $\mathrm{P}\left(\ell_{l,\kappa}(s)\right)$, but the pathway $\mathrm{P}\left(h_{l,\tau}(s)\right)$ after $h_{l,\kappa}(s)$ does track $\mathrm{P}\left(\ell_{l,\kappa}(s)\right)$ and vice versa. Even if $l \ngtr \kappa$ there is of course a relationship between $\left|\Delta\hat{\eta}_{q_r}\right|$ and Equation (51) (see Appendices A3, and A8).

3.1.8. Lines of reflection *Psi*, ψ

There are two lines of reflection ψ, with indeterminate lengths but prescribed orientations

$$\arg(\psi) = \tfrac{5\pi}{8} - \tfrac{t}{2}\ln([\nu]) \text{ if } l = 1, \text{ for Euler's } \textit{zeta} \tag{59}$$

and

$$\arg(\psi) = \tfrac{-3\pi}{8} - \tfrac{t}{2}\ln\left(l^2\left[\tfrac{\nu}{l}\right]\right) \text{ if } l \geq 2, \text{ for } \eta_l(s) \tag{60}$$

which pass through the origin. *Psi* is a line of reflection for the arguments for all paired vectors, and therefore the line of reflection for the difference between all neighbouring vectors. It is the line of reflection for the pathways $\mathrm{P}\left(h_{l,\kappa}(s)\right)$ and $\mathrm{P}\left(\ell_{l,\kappa}(s)\right)$ or $\mathrm{P}(\zeta_\kappa(s))$ when $\sigma = \frac{1}{2}$ since the paired vectors have equal magnitudes when $\sigma = \frac{1}{2}$ and paired pathways set of from the origin.

The first vector of $\ell_{l,\kappa}(s)$, $\vec{\mathcal{L}}_1$ has an orientation of $-(t\ln(l) + \pi)$ and the orientation of the first vector of $h_{l,\kappa}(s)$ appears in Equation (22). The $\arg(\psi)$ is half the sum of the two arguments.

3.2. A partial Euler's zeta function with a complex domain has two roles

This section illustrates $\zeta_\tau(s)$ and its $\mathrm{P}(\zeta_\tau(s))$ having zeros or minima at an $\mathrm{Im}(s)$ very close to $\mathrm{Im}(\rho)$ and symmetry arguments keep these minima on the critical-line. When σ becomes large the function heads to unity.

When analytical continuation is applied in $\eta_l(s)$, the series $\zeta_\tau(s)$ plays a dual role, (1) as a function which vanishes when $s \in \{\rho\}$ and, (2) as the driver that brings $\eta_l(s)$ to unity when $\sigma \gg 1$.

Furthermore, if $\zeta_\tau(s)$ were to play a role when $\sigma \neq \frac{1}{2}$, in helping to generate a non-trivial zero off the critical-line, then it would need to do so at all values of l and yet $\zeta_\tau(s)$ is insensitive to l whilst $\ell_{l,n}(s)$ and $h_{l,r}(s)$ are affected by l. This reassures us that if there were there a $\eta_l(\rho_u) = 0$ there would also be $\zeta_\tau(\rho_u) = 0$.

3.2.1. In Euler's *zeta*, the final pseudo-convergence ends where divergence starts at the *tau* vector

A point which best represents the centre of the final pseudo-convergence of $\zeta_n(s)$ is the output of a function $\theta(s)$ which employs the *tau* vector. The point $\theta(s)$ does not sit at $\zeta_\tau(s)$ but at a point which can be specified by a variety of averaging formulae involving neighbouring vectors. For $\zeta_\tau(\rho)$ the point $\theta(\rho)$ is very close to zero and gets asymptotically closer to zero as $\mathrm{Im}(\rho)$ rises. The function $\theta(s)$ could generate a point in $\mathrm{P}(\zeta_n(s))$ half-way along $\vec{\tau}$, or generate one based on an average of $\vec{\tau}$ with an immediate neighbour but a refined mechanism for $\theta(s)$, would be to use the diverging spiral when $m > \tau$, see Figure 9.

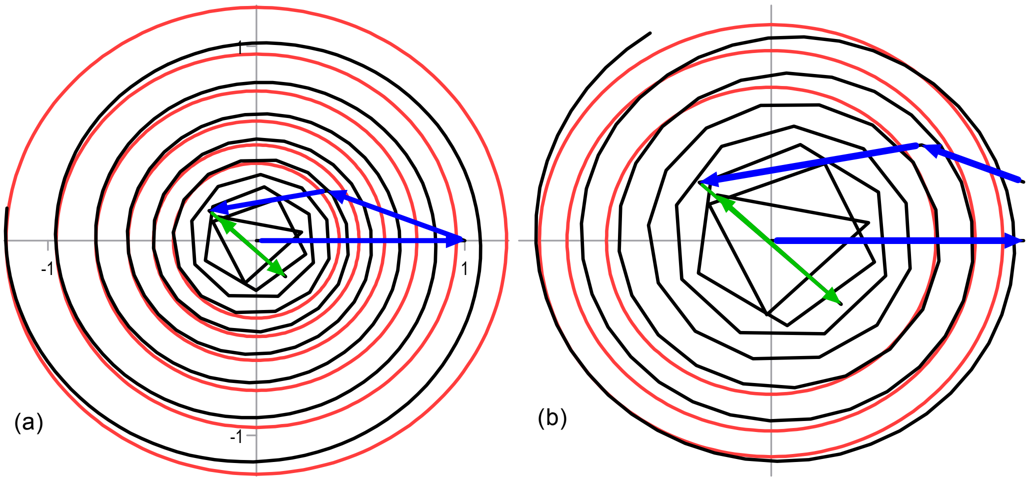

Figure 9. (a) In blue the first 3 vectors of $\zeta_\tau(\frac{1}{2} + 14.1347i)$ are shown, and in green the 4th and the *tau* vectors pass close to zero. The growing black spiral is divergence and the red circles are all centred at 0. The spiral of divergence crosses each red circle only once. **(b)** Illustration to show how a smoothed curve representing $\mathrm{P}(\zeta_n(s))$ in black would cross or touch a circle centred at zero twice when $s \notin \{\rho\}$ in spite of $\vec{\tau}$ (green) now passing through zero for $\sigma = 0.55$ and $t = 14.1347$. A similar plot would apply if $\sigma = 0.50$ and $t = 14.23$

Displacing s from $\{\rho\}$ can bring the vector $\vec{\tau}$ of Euler's *zeta* to cross zero, but these are not non-trivial zeros. This exercise emphasises why small changes in σ or t away from a ρ, that bring a $\vec{\tau}$ to sit exactly at zero are not elements of $\{\rho\}$. Given that at low t the vector $\vec{\tau}$ sits a little away from zero there are two scenarios to illustrate. Firstly, $\vec{\tau}$ passes through zero for 14.1347 at $\sigma = 0.55$ see Figure 10(a) (blue pathway), could this be valid domain? It cannot be a valid domain since $\sigma = 0.45$ fails the functional equation (red pathway).

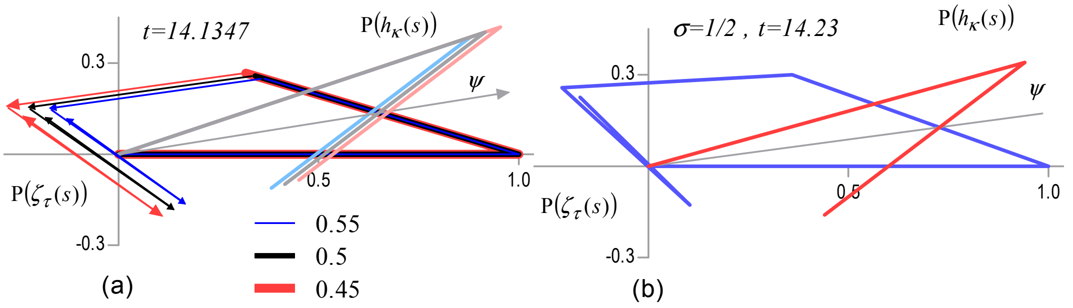

Figure 10. (a) Shows the first 5 vectors of $\mathrm{P}(\zeta_\tau(s))$ for $\sigma = 0.45$ in red, $\sigma = 0.50$ in black and $\sigma = 0.55$ in blue with arrow heads. The vector $\vec{\tau}$ for $\sigma = 0.55$ crosses zero. The two vectors of

$\mathrm{P}\big(h_{1,\kappa}(s)\big)$ for each real domain are shown in paler colours without arrow heads. **(b)** A change in t can bring the vector $\vec{\tau}$ to cross zero with a real domain on the critical-line but the crossing is removed from the middle of the vector and so no $\theta(s)$ would generate a zero.

Furthermore, only when $\sigma = \frac{1}{2}$ do the paired *kappa* vectors meet at ψ in symmetry, but a plot of the divergent spiral would cross a circle centred at the origin twice. These show that there is no zero for $\zeta_\tau(s)$ off the critical-line at $\sigma = 0.55$. Secondly a change in t to $t = 14.23$ brings the vector $\vec{\tau}$ to zero but it is clear in this example that this is far from the middle of $\vec{\tau}$, see Figure 10(b).

Analytical continuation, as in Dirichlet's *eta*, obviates the need for a $\theta(s)$, but the points above are made to emphasis that: (1) there is no reason to believe that a $\mathrm{P}\big(\zeta_n(\rho_{u_\alpha})\big)$ would have a vector $\vec{\tau}$ that did not cross close to zero, nor (2) a divergent spiral whose $\theta(\rho_{u_\alpha})$ was not centred at zero. In these respects $\mathrm{P}\big(\zeta_n(\rho_{u_\alpha})\big)$ would share the features shown in Figure 9(a) that follow for all of $\{\rho_i\}$. For these reasons, it is axiomatic that for high values of t, where RH might fail we can say that, if for Riemann's *zeta* $\zeta(\rho_{u_\alpha}) = 0$ then for $\zeta_\tau(\rho_{u_\alpha})$ we have a $\theta(\rho_{u_\alpha}) = 0$ and we lose no force of argument by considering that if *tau* is the subscript we can understand that $\zeta_\tau(\rho_{u_\alpha}) = 0$.

3.2.2. Symmetry in Euler's *zeta*

The pathway of Euler's *zeta*, without analytical continuation is shown for the 901^{st} non-trivial zero in Figure 11(a) in black. The first five $\vec{m}$ of the proximal pathway are emphasized with dark arrows on the right-hand side. Overall, the symmetries are striking since $\arg(\psi)$ is close to $\frac{\pi}{2}$. The pathway has 14 blue proximal vectors, and many distal vectors, with 9 primitive superstructures and 5 obvious superstructures each with paired pseudo-spirals ending back at the origin. The distal pathway, in black, has 14 red $\vec{\mathcal{R}}_r$ vectors laid upon it. These mirror the blue vectors and the first five of $\mathrm{P}\big(h_{1,\kappa}(s)\big)$ are shown with red arrow heads. The black pathway of Euler's *zeta* ultimately diverges as implied by the expanding grey clockwise spiral. Figure 11(a) also illustrates the approximation

$$\zeta_\tau(s) \approx \zeta_\kappa(s) - h_{l,\kappa}(s). \tag{61}$$

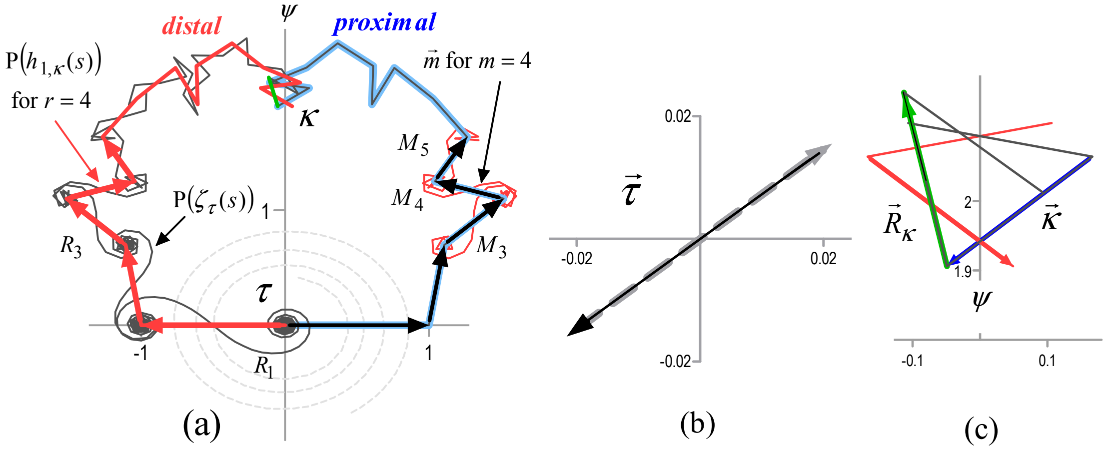

(a) (b) (c)

Figure 11. (a) In black $\mathrm{P}(\zeta_\tau(s))$ is shown with $\sigma = \frac{1}{2}$ and $t = 1303.2732$ as far as the τ vector. In blue the 14 $\vec{m}$ of $\mathrm{P}(\zeta_\kappa(s))$ are shown and in red their 14 reflections being the $\vec{\mathcal{R}}_r$ of $\mathrm{P}\big(h_{1,\kappa}(s)\big)$ which retrace the distal pathway of $\mathrm{P}(\zeta_\tau(s))$. **(b)** The final pseudo-convergence of $\mathrm{P}(\zeta_\tau(s))$; in black the vector $\vec{m}$ for $m = 414$ and in dashed grey $\vec{m}$ for $m = 415$ are shown. The second of these is the τ vector. **(c)** The $\vec{m}$ vector, for which $m = \kappa$ is shown in blue as $\vec{\kappa}$ and the $\vec{m}$ vector for which $m = \kappa + 1$ is shown in green. In red $\vec{\mathcal{R}}_\kappa$ the κ^{th} vector of $\mathrm{P}\big(h_{1,\kappa}(s)\big)$ intersects with ψ where the paired vectors cross one another.

In Figure 11(a) divergence of $\mathrm{P}(\zeta_n(s))$, shown as a dashed grey spiral, commences immediately after two easily located vectors which almost exactly oppose one another, as shown in Figure 11(b). Divergence starts after the *tau* vector $\vec{\tau}$, which for Euler's *zeta* is at

$$\tau = \left[\frac{1}{2}\left(\left(e^{\frac{\pi}{t}} - 1\right)^{-1} + \left(1 - e^{-\frac{\pi}{t}}\right)^{-1}\right)\right]. \tag{62}$$

In Figure 11(c), the junction of proximal and distal parts of the pathway are redrawn with the κ^{th} vector $\vec{m}$ of $\zeta_n(s)$, when $m = \kappa$ indicated $\vec{\kappa}$ and here shown in blue. *Kappa* is defined as

$$\kappa := \left[\frac{1}{2}\left(\left(e^{\frac{2\pi}{t}} - 1\right)^{-\frac{1}{2}} + \left(1 - e^{-\frac{2\pi}{t}}\right)^{-\frac{1}{2}}\right)\right]. \tag{63}$$

Since the *point-of-inflection* in the last superstructure $\mathcal{R}_1$, will be near

$$m \approx \left(e^{\frac{2\pi}{t}} - 1\right)^{-1}$$

we know that κ^2 and indeed $\kappa(\kappa + 1)$ will be located in this region and so will be sited only a little distance from the final pseudo-convergence of $\zeta_\tau(s)$. For very large t the product $\kappa(\kappa + 1)$ will reference a vector that is asymptotically close to the *point-of-inflection*. The lowest value of l which reveals the symmetries yields $\kappa l = \kappa(\kappa + 1)$. These two locations are shown in Figure 12.

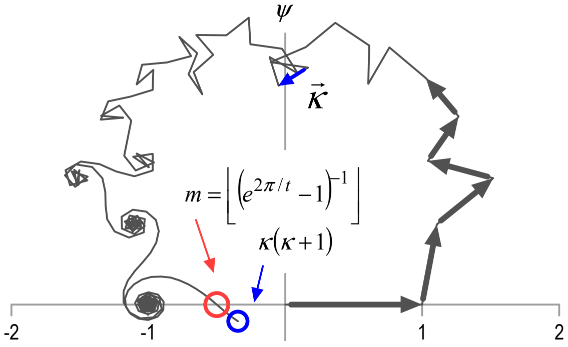

Figure 12. The partial Euler *zeta* series: $\mathrm{P}(\zeta_n(s))$ for the 901st non-trivial zero. The red circle and arrow are at the *point-of-inflection*, the blue circle is at $\kappa(\kappa+1)$ which bears a relationship to κl when l is the lowest value which exposes the symmetries in $\mathrm{P}(\eta_l(s))$.

The lowest value of l which exposes the symmetries is useful but it should be appreciated that when $l = \kappa + 1$ though $\zeta_{\kappa l}(s)$ is small it does not completely vanish at the non-trivial zeros. However, for all the non-trivial zeros of Riemann's *zeta* function, $\zeta(\rho_i) = 0$, we expect the un-extended Euler *zeta* series $\zeta_\tau(\rho_i) \approx 0$. Likewise, if there exists an as yet unknown non-trivial zero of an analytically continued *zeta* function $\zeta(\rho_u) = 0$ with $\sigma \neq \frac{1}{2}$ then we expect Euler's *zeta* series $\zeta_\tau(\rho_u) \approx 0$. Later we will see that $\eta_l(s) \approx \zeta_n(s) + \lambda_l(s,x)$ and so manipulations that allow $n \approx \tau$ in the $\zeta_n(s)$ series are helpful since they permit $\eta_l(s) \approx \lambda_l(s,x)$ near the non-trivial zeros. It will be seen that if $l = [{}^{\tau}/_{\kappa}]$ the those requirements are met.

3.2.3. Unique intersections at ψ in Euler's *zeta*: the function $\lambda_1(s,x)$

The final vectors of the paired pathways $\mathrm{P}(\zeta_\kappa(s))$ and $\mathrm{P}\big(h_{1,\kappa}(s)\big)$ are $\vec{\kappa}$ and $\vec{\mathcal{R}}_\kappa$, and over certain short intervals in t they meet and cross at the line ψ. These intersections occur when $\mathrm{Im}(s)$ is close to $\mathrm{Im}(\rho_i)$, but all intersections have to be with $\sigma = \frac{1}{2}$ to be in symmetry. Without a symmetrical intersection there is no overlap of proximal vectors with complimentary distal superstructures for either pathway. The fraction along the *kappa* vector at which intersection takes place is designated x with $0 < x \leq 1$ so that $x = 0$ is no intersection.

The difference between the two pathways can then be defined as $\lambda_1(s,x)$;

$$\lambda_1(s,x) := (\zeta_{\kappa-1}(s) + x\vec{\kappa}) - \big(h_{1,\kappa-1}(s) + x\vec{\mathcal{R}}_\kappa\big), \tag{64}$$

yielding an approximation to Euler's *zeta* of

$$\zeta_\tau(s) \approx \lambda_1(s,x). \tag{65}$$

Calculations suggest that the relationship $x = f(t)$ is an oscillation whose frequency decreases as t rises, with x mostly satisfying $\frac{2}{10} < x < \frac{8}{10}$ (see Appendix A4). In the absence of a deeper understanding of $x = f(t)$ the value $= \frac{1}{2}$ is used in Figure 13 to illustrate $\lambda_1(s,x)$ tracking the non-trivial zeros of Riemann's *zeta* function over an interval in t from 14 to 50.

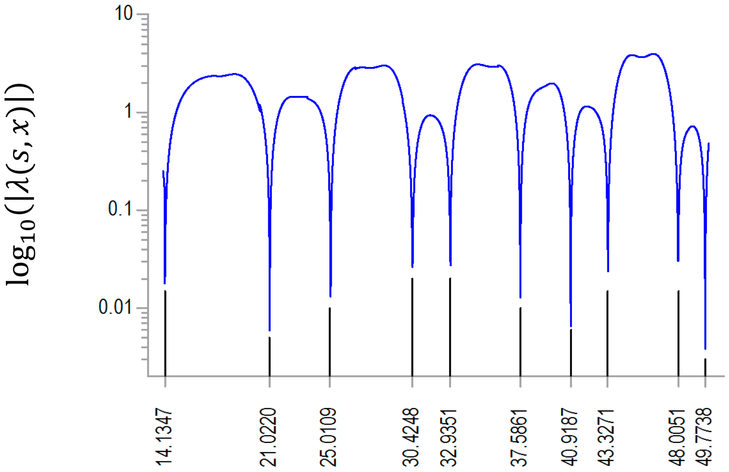

Figure 13. A plot of the log magnitude of $\lambda_1(s,x)$ for $\sigma = \frac{1}{2}$ (using $x = \frac{1}{2}$) over an interval embracing the first 10 non-trivial zeros which are indicated with fine vertical lines.

Figure 13 shows that minima in the magnitude of $\lambda_1(s,x)$, over an interval embracing the first 10 known non-trivial zeros of the Riemann *zeta* function, coincide well with those zeros. The function $\lambda_1(s,x)$ behaves well in this interval and it is of interest to identify the upper and lower bounds that could host non-trivial zeros if $0 < x \leq 1$, rather than fixing $x = \frac{1}{2}$.

3.2.4. The short finite series $\zeta_\kappa(s)$ and $h_{1,\kappa}(s)$ specify intervals in t which host non-trivial zeros

The short finite series $\zeta_\kappa(s)$ and $h_{1,\kappa}(s)$ can be used to determine the upper and lower bounds of an interval in t, which could host a non-trivial zero. The interval in t is that for which there is overlap of the *kappa* vectors, either with each other, or with ψ. These are formally the same but the latter is computationally simpler. An example is shown in Table 1.

Table 1. $\lambda_1(s,x) = 0$ for x over the interval 0 to 1

x	Lower bound	t_i	Upper bound	Δt Interval[1]
[0→1]	1132489.1590	1132489.163	1132489.1711	0.0120
[1→0]	1132489.5795	1132489.585	1132489.5877	0.0081
[0→1]	1132490.1633	1132490.165	1132490.1697	0.0063

1. Intervals in t over which $\vec{\kappa}$ intersects with $\vec{\mathcal{R}}_\kappa$ or ψ. [0→1] indicates that the lower bound relates to $x = 0$ and the upper bound to $x = 1$.

The intervals in t in Table 1 are conservative since the values of $x = 0$ and $x = 1$ lie just inside the Lower and Upper bounds. This example shows that a short finite series to *kappa* terms of only 425 can identify narrow intervals in t relatively high up the imaginary axis that are able to host non-trivial zeros, however, there is no relationship between the prime composition of *kappa* and the number of non-trivial zeros in an associated region.

3.2.5. *Kappa* and the number of non-trivial zeros covered

Each sequential value of *kappa* makes a growing imaginary region accessible to the *lambda* function such that each value hosts more non-trivial zeros. Figure 14 shows on the left-hand axis the total number of non-trivial zeros and on the right axis the number of zeros associated with that specific value of *kappa*.

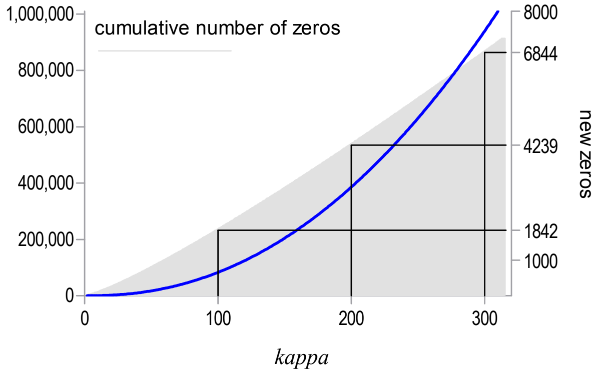

Figure 14. The cumulative number of zeros is plotted in blue using the right-hand axis against *kappa* on the x axis. A dense histogram in grey shows the number of zeros associated with each value of *kappa.* For example, a *kappa* of 200 specifies an interval in t of 2512.68 covering 4239 non-trivial zeros in an interval starting at $t =$ 250,073.4.

At the conception of this work it was not imagined that such short finite series could capture so many zeros of the infinite *eta* series. Continuing from Figure 14, intersection of *kappa* vectors at $\kappa = 423$ from $t_i = 1{,}124{,}244.12$ to $t_i = 1{,}129{,}565.69$ contains 10,246 non-trivial zeros. From the $1{,}985{,}173^{rd}$ zero to the $1{,}995{,}418^{\,th}$zero, each of these can be located by $\lambda_l(s,x)$.

3.2.6. The behaviour of Euler's *zeta* function when $\sigma \neq \frac{1}{2}$.

Figure 15(a) illustrates symmetry breaking in the finite series tracking the behaviour of Euler's *zeta* function. The pathways $\mathrm{P}\big(\zeta_\kappa(s)\big)$ and $\mathrm{P}\big(h_{1,\kappa}(s)\big)$ appear for the 901st non-trivial zero, as in Figure 11, but are also plotted for two values of $\sigma \neq \frac{1}{2}$. Euler's *zeta* approximates as follows; $\zeta_\tau(s) \approx \zeta_\kappa(s) - h_{1,\kappa}(s)$. Figure 15(a) uses $\lambda_1(s,x)$ with $x = 0.77$ for this region of t for plotting the larger vector equating to $\zeta_\tau\big(\frac{1}{4} + it\big)$.

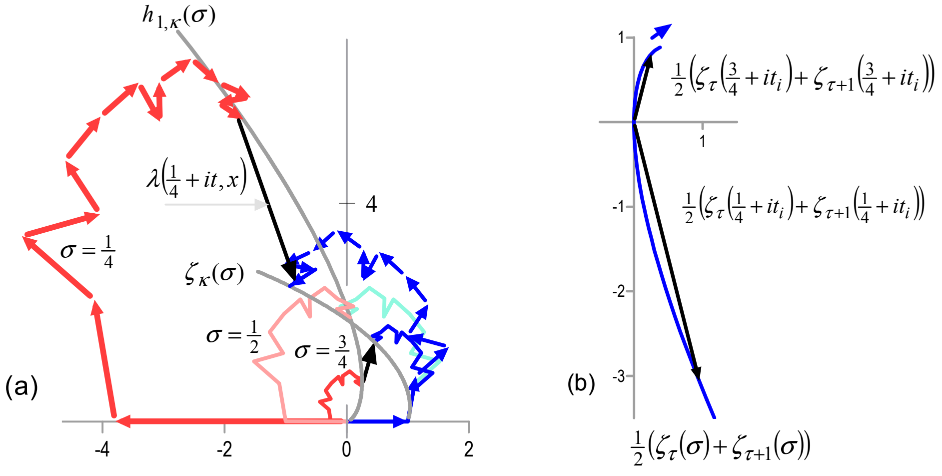

Figure 15. (a) $\lambda_1(s,x)$ with its two finite series; $\mathrm{P}\big(h_{1,\kappa}(s)\big)$ in red and $\mathrm{P}(\zeta_\kappa(s))$ in blue, with $\kappa = 14$. The light pathways have $\sigma = {}^1/_2$ and their κ vectors intersect in a unique way at this ρ. The outer pathway with arrows is for $\sigma = {}^1/_4$ with the downward black vector being $\lambda_1(s,x)$ with $x = 0.77$. The inner smaller solid pathway is for $\sigma = {}^3/_4$ with the upward black vector being $\lambda_1(s,x)$. The two grey lines represent $h_{1,\kappa}(\sigma)$ for fixed t ending at 0, and $\zeta_\kappa(\sigma)$ ending at 1. These arcs cross at the non-trivial zero. **(b)** $\zeta_\tau(\sigma)$ for fixed t is plotted in blue with σ rising in the direction of the arrow. Two vectors representing $\zeta_\tau(s)$ are illustrated (with averages made explicit) and they equate in magnitude and argument with the comparable vectors in $\lambda_1(s,x)$ plotted in (a).

Preprints (www.preprints.org) | NOT PEER-REVIEWED | Posted: 16 March 2017 doi:10.20944/preprints201703.0121.v1

It is noted that Figure 15(a) has plots of $\zeta_\kappa(\sigma)$ for fixed t which track the end of $\vec{\kappa}$ and the end of $\vec{\mathcal{R}}_\kappa$ and not the movement of the points $x\vec{\kappa}$ and $x\vec{\mathcal{R}}_\kappa$, nonetheless the figure serves to show that

$$\left(h_{1,\kappa-1}(s) + x\vec{\mathcal{R}}_\kappa\right) + \zeta_\tau(s) = \zeta_{\kappa-1}(s) + x\vec{\kappa}.$$

Figure 15(a) also shows that for Euler's *zeta* when $\sigma < \frac{1}{2}$ the $\mathrm{P}\left(h_{1,\kappa}(s)\right)$ is bigger than the matching $\mathrm{P}(\zeta_\kappa(s))$, and when $\sigma > \frac{1}{2}$ the pathway $\mathrm{P}\left(h_{1,\kappa}(s)\right)$ is smaller than the matching $\mathrm{P}(\zeta_\kappa(s))$. This difference in behaviour is important and will be shown to be similar for $\eta_l(s)$ with $l \geq 2$; when $\sigma < \frac{1}{2}$ a $\mathrm{P}\left(h_{l,\kappa}(s)\right)$ is bigger than the matching $\mathrm{P}\left(\ell_{l,\kappa}(s)\right)$, and when $\sigma > \frac{1}{2}$ a $\mathrm{P}\left(h_{l,\kappa}(s)\right)$ is smaller than the matching $\mathrm{P}\left(\ell_{l,\kappa}(s)\right)$.

An alternative approach is to reverse $h_{1,\kappa}$ and start a related vector series $\hbar_{1,\kappa}(s)$ from a point of overlap with the end of $\zeta_\kappa(\sigma)$, this complimentary pathway is $\hbar_{1,\kappa}(s)$ and is defined as

$$\hbar_{1,\kappa}(s) := \sum_{r=\kappa}^{1} -\vec{\mathcal{R}}_r. \tag{66}$$

In Figure 16, the pathway $\mathrm{P}(\zeta_\tau(s))$ is shown in blue for $\sigma = 0.35$. This is the pathway of Euler's *zeta* preceding the overt commitment to divergence.

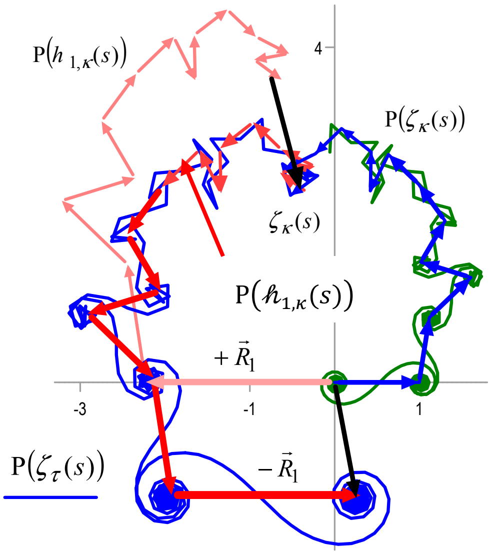

Figure 16. A plot of $\mathrm{P}(\zeta_\tau(s))$ in blue with $\sigma = 0.35$ at $t = 1303.273$ with the distal pathway tracked with $\hbar_{1,\kappa}(s) = \sum_{r=\kappa}^{1} -\vec{\mathcal{R}}_r$ which reverses the series $h_{1,\kappa}(s)$. This figure shows the relationship between the superstructures and the vectors persisting when $\sigma \neq \frac{1}{2}$. In green the superstructures of $\hbar_{1,\tau}(s) = \sum_{r=\tau}^{\kappa} -\vec{\mathcal{R}}_r$ are shown for completeness. In pink is shown $\mathrm{P}\left(h_{1,\kappa}(s)\right)$.

The relationship with $h_{1,\kappa}(s)$ is clear, and the two vectors in black representing $\zeta_\tau(s)$ can be seen to have the same magnitudes and arguments. The first 14 vectors of $\mathrm{P}(\zeta_\kappa(s))$ up to $\zeta_\kappa(s)$ appear with blue arrows. The distal part of $\mathrm{P}(\zeta_\tau(s))$ after the $\vec{\kappa}$ vector is tracked by the dark red pathway of $\mathrm{P}\left(\hbar_{1,\kappa}(s)\right)$ in which the index r falls from κ to 1 so that

$$\zeta_\tau(s) = \zeta_\kappa(s) + \hbar_1(s). \tag{67}$$

The handling of x is a trivial refinement that could be added if desired. This exercise is merely for illustration as the function $\hbar_{1,\kappa}(s)$ adds no new information. It may however lend appreciation to the importance of the superposition of vectors from one pathway on the superstructures from a complimentary pathway.

3.2.7. The pathway for Euler's *zeta*, $\mathrm{P}(\zeta_n(s))$ is the *Bauplan* for $\mathrm{P}\left(\eta_l(s)\right)$

A "*Bauplan*" is a biological term for a collection of morphological features which are shared among many members of a group. Euler's *zeta* is the *Bauplan* for $\mathrm{P}(\eta_l(s))$ This work expects Euler's *zeta* $\zeta_\tau(s) \approx 0$ when $s \in \{\rho\}$ and for this to be more challenging at low values of t than at high values. However, even at the first non-trivial zero 14.1347, for which $\tau = 5$ and $\kappa = 2$, which we met in section 3.2.1. and in Figure 9(a) it is still pretty good. This zero is shown again in Figure 17, with the symmetrical pathway $\mathrm{P}\big(h_{1,\kappa}(s)\big)$, which also has 2 vectors. The line of reflection is ψ.

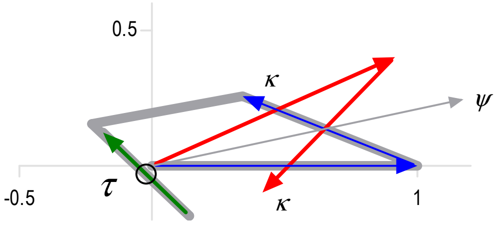

Figure 17. In grey, the pathway $\mathrm{P}(\zeta_\tau(s))$ for $t = 14.1347$ and $\sigma = \frac{1}{2}$ is shown with its 5 $\vec{m}$ vectors; the fifth shown in green almost opposes the fourth. Here $\tau = 5$ and $\kappa = 2$. The pathway $\mathrm{P}(\zeta_\kappa(s))$ is shown in blue crossing the line ψ. In red is $\mathrm{P}\big(h_{1,\kappa}(s)\big)$. The average of the τ vector and its predecessor appears as a black circle. It is close to zero but not at zero.

The expectation is that all subsequent non-trivial zeros of $\zeta_\tau(s)$ have the middle of their τ vectors, or an appropriate average of neighbours, lying even closer to zero. Moving to $\eta_l(s)$ in Figure 18(b), plots of $l = 2$ to $l = 5$ are shown with Euler's *zeta* for comparison, there is one $\mathrm{P}(\eta_l(s))$ shown for each vector of $\mathrm{P}(\zeta_\tau(s))$.

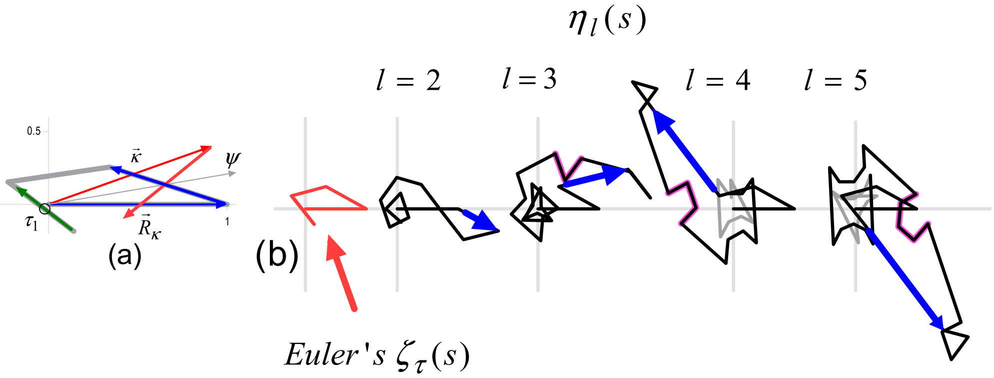

Figure 18. **(a)** The 5 vectors of $\mathrm{P}(\zeta_\tau(s))$ with $t = 14.1347$ and $\sigma = \frac{1}{2}$. **(b)** The *Bauplan*, $\mathrm{P}(\zeta_\tau(s))$ is shown in red followed by the 4 pathways for $\mathrm{P}(\eta_l(s))$ for $l = 2$ to $l = 5$, each shown until convergence is evident. All 4 converge to zero. The blue arrows are the first negated and magnified terms in each series. If the first 5 vectors of each pathway are compared it can be seen that matched vectors share arguments, but there is a phase shift of π for the l^{th} vector.

The images in Figure 18 show the first non-trivial zero is preserved on altering l. Even at this low value of t near-regular polygons with one missing side are discernible in the *principal-axis* of the rudimentary $\mathcal{R}_1$ structures; a triangle $(l = 3)$, a square $(l = 4)$, and a pentagon $(l = 5)$, are highlighted. For completeness it is noted that when $l = 2$, at larger values of t the equivalent of the near-regular polygon with a missing side is a single vector between two nearly co-linear negated vectors.

3.3. *The pathway to convergence for Dirichlet's eta function*

In Figure 19, the pathway $\mathrm{P}(\eta_2(s))$ for a zero is shown in blue. The proximal pathway has in sequence, a set of $\vec{m}$ starting with $\vec{1}$ and proceeding with diminishing magnitudes $m^{-\sigma} > (m+1)^{-\sigma}$. These proximal vectors do not form an obvious superstructure unless their reduced arguments θ Equation (32) form an *opportunistic* sequence (see Appendix A5).

Most importantly the vector $\vec{1}$ is unaffected by σ and introduces an asymmetry which is absent when we consider the differentials. The influence of the vector $\vec{1}$ on how the pathway shrinks when σ rises varies when l is altered since the rest of the $\mathrm{P}(\eta_l(s))$ rotates and is magnified. Once $\ln\left(\frac{m}{m-1}\right) - \ln\left(\frac{m+1}{m}\right) < \frac{2\pi}{t}$ sets of sequential vectors $\vec{m}$ form the paired pseudo-spiral superstructures, $\mathcal{R}_r$. A finite sequence of these superstructures runs as r falls until $r = 1$ and these are also shown in blue. The last, and largest pair of pseudo-spirals is $\mathcal{R}_1$ whose final pseudo-spiral embraces convergence.

The *principal-axis* of an $\mathcal{R}_r$ structure has a relationship with an $\vec{\mathcal{R}}_r$. Importantly $\vec{\mathcal{R}}_r$ has an identity independent of the $\mathcal{R}_r$ structure and is described by the complimentary pathway $\mathrm{P}(\bar{h}_2(s))$, such that when r is large the vector $\vec{\mathcal{R}}_r$ has an existence even when $\mathcal{R}_r$ structures are not formed by $\mathrm{P}(\eta_2(s))$.

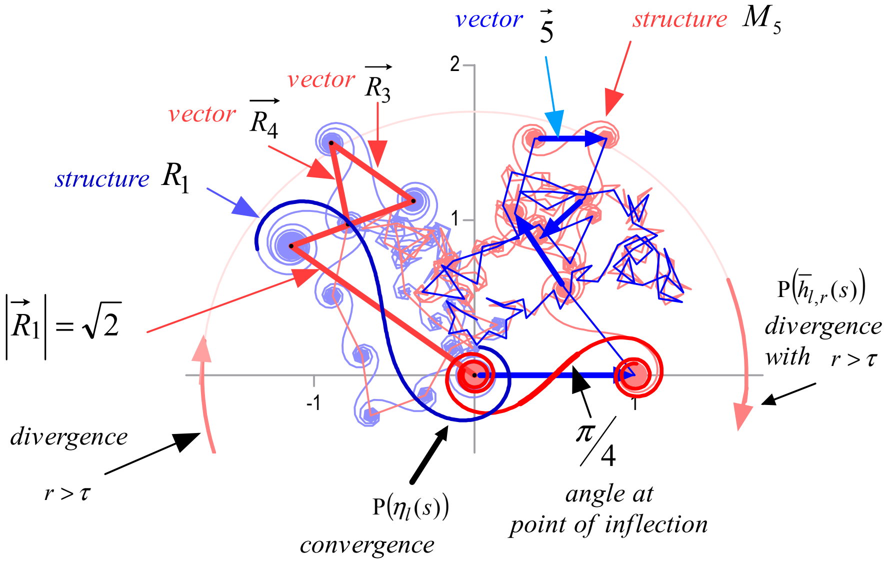

Figure 29. Two pathways are shown; $\mathrm{P}(\eta_l(s))$ in blue and $\mathrm{P}(\bar{h}_{l,\tau}(s))$ in red for $l = 2$, $t_i = 17224.28267$ and $\sigma = \frac{1}{2}$. Both pathways start and end at 0. The series of $\vec{m}$ vectors $\vec{1}$, $\vec{3}$, $\vec{5}$ and $\vec{7}$ are shown in bold in blue. In red the series of $\vec{\mathcal{R}}_r$ vectors, is plotted with $\vec{\mathcal{R}}_1$, $\vec{\mathcal{R}}_2$, $\vec{\mathcal{R}}_3$ and $\vec{\mathcal{R}}_4$ in bold with $\chi_l = \{2, 6, 10, 14 \ldots\}$. In pink part of the encircling clockwise divergent pathway of $\mathrm{P}(\bar{h}_{l,r}(s))$ is indicated for an interval in $r > \tau$.

In Figure 19 $\mathrm{P}(\bar{h}_{l,r}(s))$ is shown in red alongside $\mathrm{P}(\eta_2(s))$. Proximally $\mathrm{P}(\bar{h}_{l,r}(s))$ has in sequence, a finite set of vectors, and since $l = 2$ they have diminishing magnitudes $|\vec{\mathcal{R}}_r| > |\vec{\mathcal{R}}_{r+1}|$. The series ends distally in paired pseudo-spirals $\mathcal{M}_m$ before divergence. The magnitude $|\vec{\mathcal{R}}_1| = \sqrt{l}$ when $\sigma = \frac{1}{2}$. Divergence is indicated with a growing pink arc when $r > \tau$. The covert symmetry is that between the arguments of $\vec{1}$, $\vec{3}$, $\vec{5}$ and $\vec{7}$ and the arguments of $\vec{\mathcal{R}}_1$, $\vec{\mathcal{R}}_2$, $\vec{\mathcal{R}}_3$ and $\vec{\mathcal{R}}_4$.

Figure 20 shows a rotated version of $\mathrm{P}(\bar{h}_{l,\tau}(s))$ with its first 24 vectors in bold. In black the first 24 odd vectors of $\mathrm{P}(\eta_2(s))$ are placed in sequence, so omitting the alternating or negated even vectors. It is clear that for these matched vectors their arguments are mirror-images and there is a line of reflection. The magnitudes however are not equal.

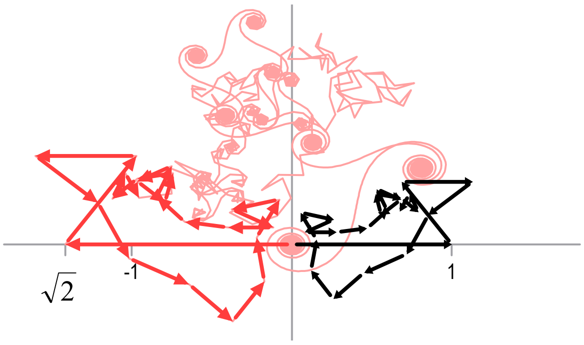

Figure 20. A modification of Figure 19 shows a rotated $\mathrm{P}(\bar{h}_{l,\tau}(s))$ in red with the odd early vectors of $\mathrm{P}(\eta_l(s))$ extracted as a novel series and shown with black arrows. The mirror-imaging of arguments is inescapable.

In the context of Figure 20 this work aimed to extract the symmetries of $\mathrm{P}(\eta_l(s))$ by allowing l to rise.

3.4. The $\mathcal{M}_m$ structures in the distal $\mathrm{P}(\bar{h}_{l,r}(s))$ and the $\mathcal{L}_n$ structures in the distal $\mathrm{P}(\ell_{l,n}(s))$

This work is principally interested in the proximal $\mathrm{P}(h_{l,\kappa}(s))$ when $l > \kappa$ but it would be remiss not to illustrate the distal $\mathrm{P}(\bar{h}_{l,r}(s))$ when $r > \kappa$. The next example is for $l < \kappa$, with $t = 1230.58$ giving $\kappa = 14$ but for which we set $l = 4$.

The $\mathcal{M}_m$ superstructures are a coherent set of small $\vec{\mathcal{R}}_r$ in the distal $\mathrm{P}(\bar{h}_{l,r}(s))$. An integer ϱ determines each $q_{\bar{r}}$ that identifies an important $\vec{\mathcal{R}}_r$, in an $\mathcal{M}_m$. The integer ϱ carries subscripts, m or $\overline{m}$, with $\varrho_m \in \mathbb{O}$ and $\varrho_{\overline{m}} \in \mathbb{E}$ referring to a pseudo-convergence or a *point-of-inflection* respectively. In like manner, the integer q was used to determine an m which identifies an important $\vec{m}$, with similar $q_r \in R_l$ and $q_{\bar{r}} \in \chi_l$ referring to a pseudo-convergence or a *point-of-inflection* in an $\mathcal{R}_r$ superstructure. The vector $\vec{m}$, unlike $\vec{\mathcal{R}}_r$ needs no subscript since it is its own index and the ordered sets $\mathbb{O}$ and $\mathbb{E}$ unlike R_l and χ_l are independent of l.

The final pseudo-convergence of $\mathrm{P}(\bar{h}_{l,r}(s))$ has a point $\bar{h}_{l,r}(s)$ at $r = \tau$ close to the start of divergence. An averaging function in this region would be appropriate for calculations but is of no material importance.

The centre of the pseudo-convergences and the *points-of-inflection* in the $\mathcal{M}_m$ are generated by the diminishing vectors of the distal $\mathrm{P}(\bar{h}_{l,r}(s))$ when $r > \kappa$ and occur near $t\ln\left(\frac{q_{\bar{r}}+2}{q_{\bar{r}}}\right) = \frac{\pi}{l}\varrho$ when neighbouring differences lie immediately either side of specific integral multiples of $\frac{\pi}{l}$. This follows from the geometry of $\mathrm{P}(\bar{h}_{l,r}(s))$. The integer ϱ distinguishes significant vectors. Sequential $q_{\bar{r}}$, rise in χ_l in increments of 2 or 4. For convenience we first assume the rise is 2 and then determine the nearest element of the set, either χ_l or R_l, using the brackets $[\![x]\!]$ to mean the nearest element of the appropriate set. The inequality

$$t\ln\left(\frac{q_{\bar{r}}+4}{q_{\bar{r}}+2}\right) < \frac{\pi}{l}\varrho \leq t\ln\left(\frac{q_{\bar{r}}+2}{q_{\bar{r}}}\right) \tag{68}$$

follows from the geometry of the l sided polygons. The *point-of-inflection* in $\mathcal{M}_m$ for each m lies at a specific $q_{\bar{r}}$ as determined by Equation (68). This point lies very close to the mid-point of the $\vec{\overline{m}}$ which equates to the *principal-axis* of the $\mathcal{M}_m$. The integral multiple of $\frac{\pi}{tl}$ is designated $\varrho_{\overline{m}}$ (being structurally similar to $q_{\bar{r}}$) with the bar indicating the association with the *point-of-inflection*. If $q_{\bar{r}}$ were allowed to take any real value then

$$t\ln\left(\frac{q_{\bar{r}}+2}{q_{\bar{r}}}\right) = \frac{\pi}{l}\varrho_m \tag{69}$$

but the nearest we can establish will be to choose $q_{\bar{r}} \in \chi_l$ as in;

$$q_{\bar{r}} = \left[\!\left[\left(e^{\frac{\pi \varrho_{\bar{m}}}{tl}} - 1\right)^{-1} + \left(e^{\frac{-\pi \varrho_{\bar{m}}}{tl}} - 1\right)^{-1} \right]\!\right] \text{ with } \varrho_{\bar{m}} \in \mathbb{E} \tag{70}$$

and

$$q_{\bar{r}} = \left[\!\left[\left(e^{\frac{\pi \varrho_{m}}{tl}} - 1\right)^{-1} + \left(e^{\frac{-\pi \varrho_{m}}{tl}} - 1\right)^{-1} \right]\!\right] \text{ with } \varrho_{m} \in \mathbb{O}. \tag{71}$$

It is important to be clear that each $q_{\bar{r}}$ relates to the mid-part of an $\vec{\mathcal{R}}_r$ and a pair of q_r (without the bar) represent the ends of the $\vec{\mathcal{R}}_r$. Here we are looking at the $\vec{m}$ whose centres are related to $\varrho_{\bar{m}}$, each determined from a $q_{\bar{r}}$, and whose ends are related to the ϱ_m which are also determined from a $q_{\bar{r}}$. This is illustrated in Figure 21 (a).

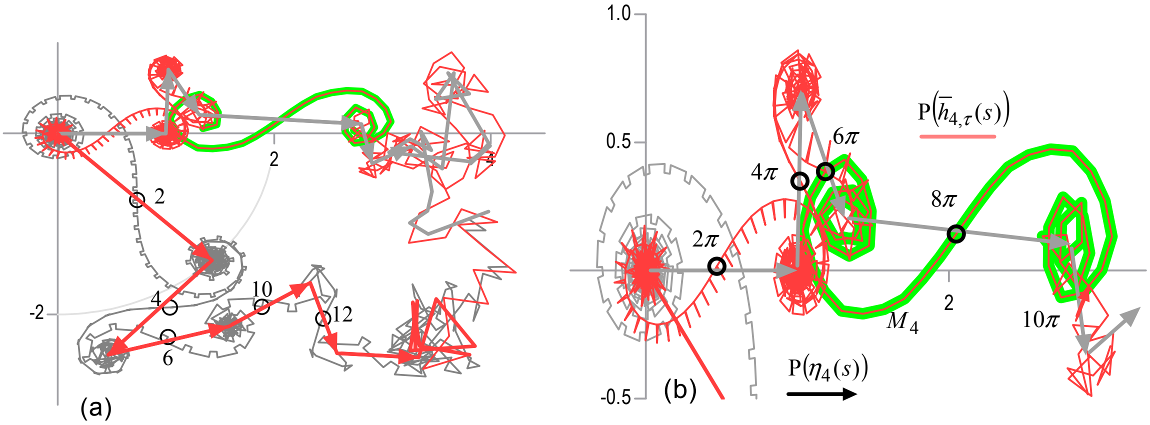

Figure 21 (a) An overview of $\mathrm{P}(\eta_4(s))$ in grey/black for $t = 1230.585$ at $\sigma = \frac{1}{2}$. In red is shown $\mathrm{P}(\bar{h}_{4,\tau}(s))$ which has in bold individual $\vec{\mathcal{R}}_r$ overlying the *principal-axes* of the $\mathcal{R}_r$ structures of $\mathrm{P}(\eta_4(s))$; the set $\{q_{\bar{r}}\}$ runs $\{2, 4, 6, 10, 12 \ldots\}$, $8 \notin \chi_4$. Note that the *principal-axis* has length $\sqrt{l}$. **(b)** detail from (a) showing the $\vec{\mathcal{R}}_r$ near the *point-of-inflection* in $\mathcal{M}_1$ to $\mathcal{M}_4$ with black circles and that near $\mathcal{M}_5$ with a red arrow at 10π.

In Figure 21(b), the $\vec{m}$ for $m = 4$ has a magnitude of $3/\sqrt{4}$ and is associated with the largest superstructure $\mathcal{M}_4$ which is highlighted in green. The $\mathcal{M}_4$ structure has a number of $\vec{\mathcal{R}}_r$ falling into a uniform progression at around 8π in contrast to the three subsequent $\mathcal{M}_m$ structures where 2 in 4 spike to one side of the pathway's progression at 6π, and where 1 in 4 double-back on the pathway's progression at 4π, see Figure 20, in this way $\mathcal{M}_4$ achieves its greater size.

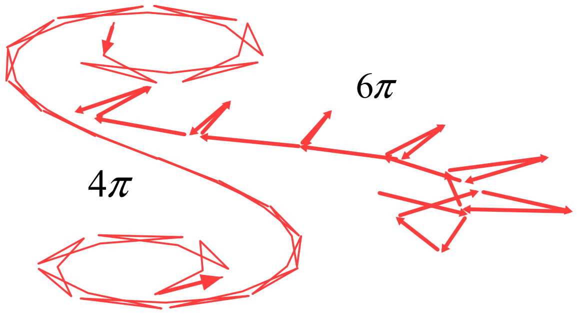

Figure 22. Detail of the geometry at 6π and 4π from $\mathrm{P}(\bar{h}_{4,\tau}(s))$ in Figure 21(b).

In Figure 21 the superposition of the $\mathcal{M}_m$ (made of many $\vec{\mathcal{R}}_r$) upon the $\vec{m}$ is clear. Importantly, the figure shows the relationship between $\vec{4}$ having a larger magnitude than its neighbours and the mechanism by which the $\mathcal{M}_m$ superstructure is able to match this change in magnitude through simple geometry. In Table 2 the relationship between m, ϱ_m, $q_{\bar{r}}$ and r is detailed. To be explicit an m specifies a ϱ_m since $m = \varrho_m/2$, then Equation (71) gives $q_{\bar{r}} = f(\varrho_m)$ and then from χ_l the $q_{\bar{r}}$ yields the value r, which is of course simply its position in the ordered set.

Table 2. Detail from Figure 21. The relationship of r in an $\vec{\mathcal{R}}_r$ to the point of inflection in the superstructure $\mathcal{M}_m$.

Inflection in Structure $\mathcal{M}_m$	$\varrho_{\bar{m}}$	Label in Figure 21(b)	Output of Equation (71)	$q_{\bar{r}} \in \chi_4$	$\vec{\mathcal{R}}_r$ r
$\mathcal{M}_1$	2	2π	1566.83	1566	588
$\mathcal{M}_2$	4	4π	783.41	782	294
$\mathcal{M}_3$	6	6π	522.28	522	196
$\mathcal{M}_4$	8	8π	391.71	390	147

The final pseudo-convergence of $\mathcal{M}_1$ from Equation (71) is at $q_{\bar{r}} = 3134$ which relates to $r = 1176$ and is illustrated in Figure 23.

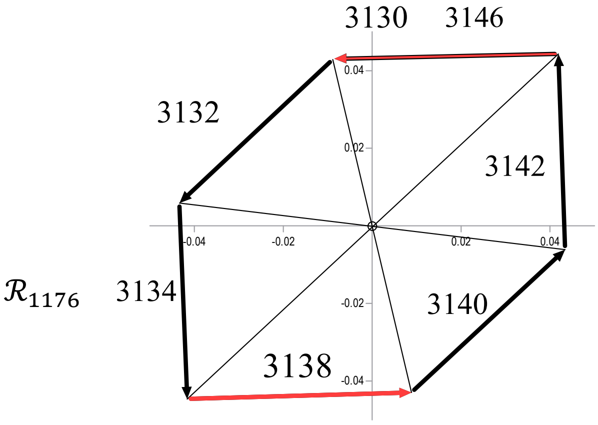

Figure 23. The final pseudo-convergence of $\mathrm{P}(\bar{h}_{4,r}(s))$ in the region specified by $\varrho_m = 1$ is $q_{\bar{r}} = [\![3133.65]\!] = 3134$ which locates $\vec{\mathcal{R}}_{1176}$. This vector with its 5 neighbours is able to provide an average pseudo-convergence remarkably close to zero.

In like manner the distal part of $\mathrm{P}(\ell_{l,\pi}(s))$ is illustrated with $\pi = \tau$ in Figure 24.

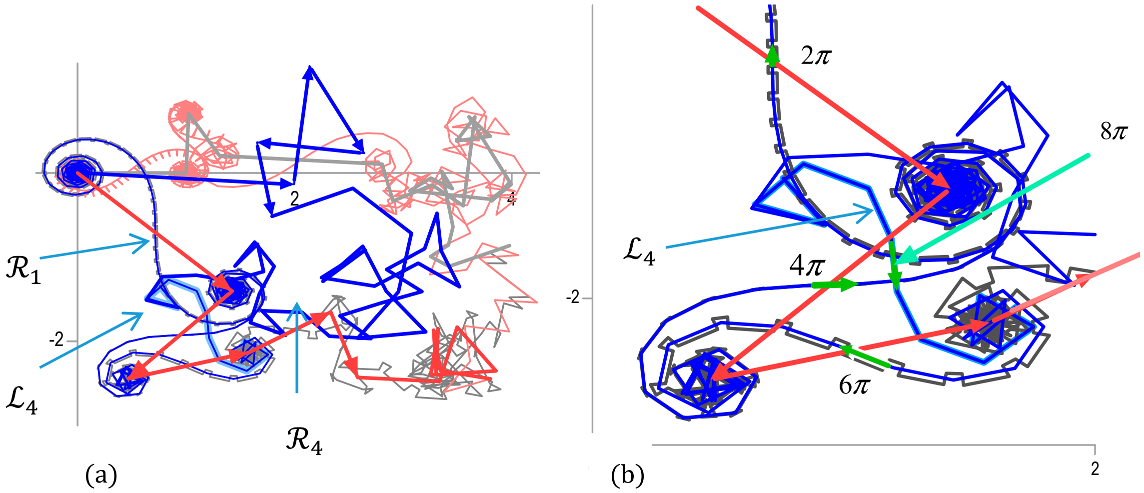

(a) (b)

Figure 24. (a) With $t = 1230.584$ and $= \frac{1}{2}$ $\mathrm{P}(\eta_4(s))$, is shown in grey/black and in red $\mathrm{P}(\bar{h}_{4,\tau}(s))$ with its early vectors is shown in bold. In blue $\mathrm{P}(\ell_{4,\tau}(s))$ is shown and would be complimentary to $\mathrm{P}(h_{4,\tau}(s))$. The first three $\mathcal{L}_n$ superstructures are superimposed on the first three $\mathcal{R}_r$ superstructures and relate to the first three $\vec{\mathcal{R}}_r$ vectors. **(b)** Detail from (a) showing the associated *points-of-inflection* in $\mathrm{P}(\ell_{4,\tau}(s))$ crossing the first three $\vec{\mathcal{R}}_r$ vectors. In these tangential arrangements the $\vec{\mathcal{L}}_n$ are in line, and their arguments differ by even multiples of 2π. There is no superposition of the $\mathcal{L}_n$ superstructure for $\mathcal{L}_4$ with $\vec{\mathcal{R}}_4$ at 8π and of course $8 \notin \chi_4$.

This section has illustrated the mechanics of superposition of distal superstructures of one pathway upon the proximal vectors of another and shows how these can be complimentary.

3.5. Symmetry-breaking in $\eta_l(s)$

We start by remembering that $\eta_{l,n}(s)$ to κl terms, using scripted $\mathscr{n}$ as a unique index for the second summation, is as follows;

$$\eta_{l,\kappa l}(s) := \sum_{m=1}^{\kappa l} m^{-s} - l^{(1-s)} \sum_{\mathscr{n}=1}^{\kappa} \mathscr{n}^{-s}.$$

This can be restated as

$$\eta_{l,l\kappa}(s) = \zeta_{\kappa l}(s) - l^{(1-s)}\zeta_{\kappa}(s). \tag{72}$$

To simplify notation and explicitly show the symmetries, the vector $\vec{\mathcal{L}}_{\mathscr{n}}$ and the function ℓ_l are;

$$\vec{\mathcal{L}}_{\mathscr{n}} := -l^{(1-s)}\mathscr{n}^{-s} \tag{73}$$

$$\text{and } \ell_l(s) := -l^{(1-s)} \sum_{\mathscr{n}=1}^{\kappa} \mathscr{n}^{-s} = \sum_{\mathscr{n}=1}^{\kappa} \vec{\mathcal{L}}_{\mathscr{n}}. \tag{74}$$

This gives us

$$\eta_{l,\kappa l}(s) = \zeta_{\kappa l}(s) + \ell_{l,\kappa}(s), \tag{75}$$

which is important, because we know that $\zeta_{lk}(\rho)$ can be close to $\zeta_{\tau}(\rho) = 0.$ We now have

$$\eta_l(s) = \zeta_{\kappa l}(s) + \ell_{l,\kappa}(s) - h_{l,\kappa}(s), \tag{76}$$

which can be refined by x to accommodate the intersection of the *kappa* vectors in *lambda*;

$$\lambda_l(s,x) = \ell_{l,\kappa}(s) - h_{l,\kappa}(s), \tag{77}$$

with

$$\eta_l(s) = \zeta_{\kappa l}(s) + \lambda_l(s,x). \tag{78}$$

3.5.1 Setting $l > \kappa$: An example of a pathway $P(\eta_l(s))$ when $l > \kappa$

The number of proximal vectors in the pathways of $\mathrm{P}(h_{l,n}(s))$ and $\mathrm{P}(\ell_{l,\mathrm{n}}(s))$ which have mirror-image arguments about ψ, rises as l increases. When $l > \kappa$, all sequential arguments between neighbouring vectors of the finite $\mathrm{P}(h_{l,\kappa}(s))$ are mirror-images of those arguments between the corresponding neighbouring vectors of the finite $\mathrm{P}(\ell_{l,\kappa}(s))$. The pathway $\mathrm{P}(\eta_l(s))$ with $l > \kappa$ is illustrated for $\mathrm{P}\left(\eta_5\left(\frac{1}{2} + it_i\right)\right)$ for $t_i = 107.1686$, the 33^{rd} non-trivial zero, in Figure 25.

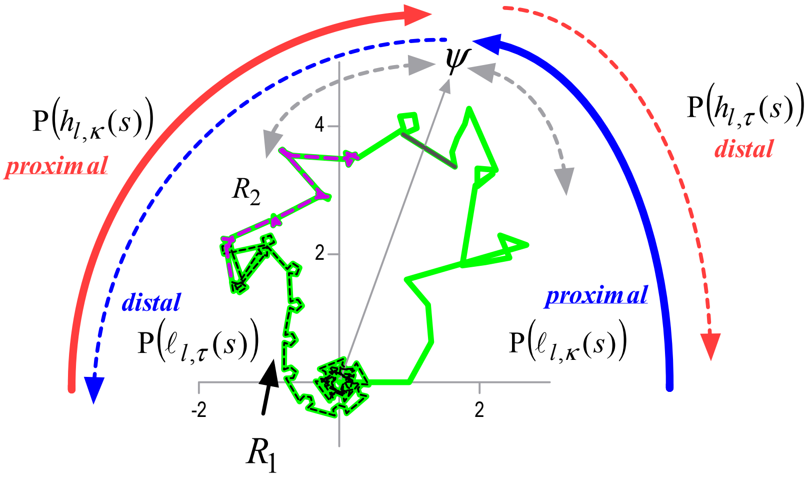

Figure 25. The pathway $\mathrm{P}\left(\eta_5\left(\frac{1}{2} + it_i\right)\right)$ for $t = 107.1686$, the 33rd zero, is shown in green. The proximal part $\mathrm{P}(\eta_{5,\kappa l}(s))$ under the solid blue arrow is tracked by $\mathrm{P}(\ell_{5,\kappa}(s))$ to its *kappa* vector and would be superimposed upon by the superstructures of the distal part of $\mathrm{P}(\bar{h}_{5,\tau}(s))$. The distal part of $\mathrm{P}(\eta_{5,\infty}(s))$ under the dashed blue arrow will be tracked by the distal part of $\mathrm{P}(\ell_{5,\tau}(s))$ and this is superimposed upon by the proximal part of $\mathrm{P}(h_{5,\kappa}(s))$. For other features see the text.

In Figure 25 the pathway $\mathrm{P}(\eta_5(s))$ has proximal and distal parts separated by the vector $\vec{m}$ where $m = \kappa l$. This vector is shown in black crossing the line ψ. The proximal part under the solid blue arrow will be tracked by $\mathrm{P}(\ell_{5,\kappa}(s))$ as far as the line of reflection ψ and as far as its *kappa* vector $\vec{\mathcal{L}}_\kappa$. The distal part of $\mathrm{P}(\eta_5(s))$ lies under the dark dashed blue arrow which will be tracked in the forward direction by $\mathrm{P}(\ell_{5,\tau}(s))$ after the line of reflection ψ and after its *kappa* vector $\vec{\mathcal{L}}_\kappa$.

There is one obvious superstructure $\mathcal{R}_1$ in this $\mathrm{P}(\eta_5(\rho))$ shown with a black dashed line over the green pathway. The function $\eta_5(s)$ also makes a weak attempt at an $\mathcal{R}_2$ shown with a dashed purple line. Figure 26 repeats plots for the 33^{rd} zero altering either σ or t.

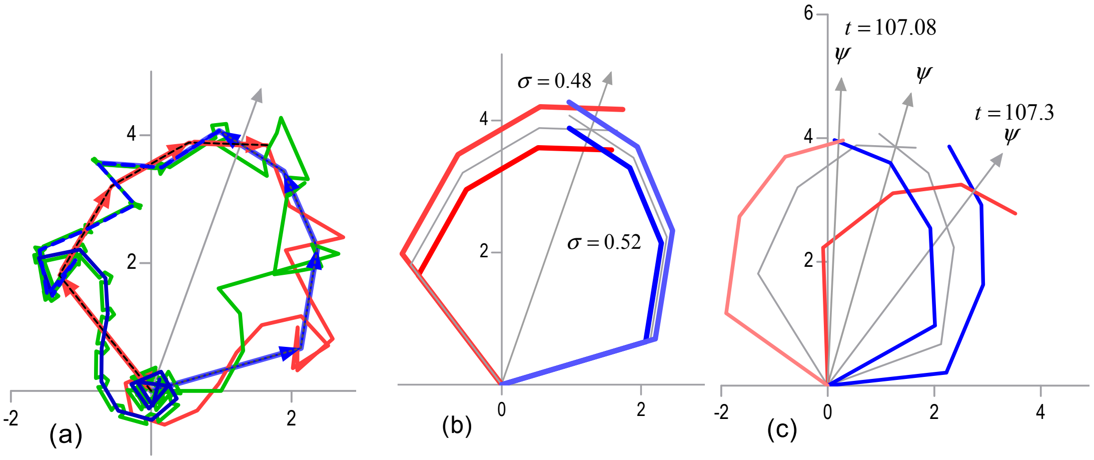

Figure 26. **(a)** $\mathrm{P}\left(\eta_5\left(\tfrac{1}{2}+it_i\right)\right)$ is shown in green for $t = 107.1686$. In dark blue is shown $\mathrm{P}(\ell_{5,\tau}(s))$ which tracks $\mathrm{P}(\eta_5(s))$ going forwards and in red is $\mathrm{P}(h_{5,\tau}(s))$ the mirror-image of $\mathrm{P}(\ell_{5,\tau}(s))$. The 4 terms up to and including $r = n = \kappa$ are shown with arrow heads. The *kappa* vectors cross and meet on the line ψ in symmetry. **(b)** $\mathrm{P}(\ell_{5,\kappa}(s))$ in blue and $\mathrm{P}(h_{5,\kappa}(s))$ in red are shown with two real domains when $\sigma \neq \tfrac{1}{2}$. The *kappa* vectors cross but their intersections are not on the line of reflection and a zero is precluded by failure of superposition. **(c)** Pathways as in (b) but all with $\sigma = \tfrac{1}{2}$ for two different values of t for which the *kappa* vectors just intersect so meeting symmetry requirements making this an interval in t which can host a non-trivial zero.

In relation to Figure 26(c) the interval in t over which x falls from 1 to 0 is roughly from 107.06 to 107.36 and there is no overlap of the vectors outside this as show in Figure 27 (a).

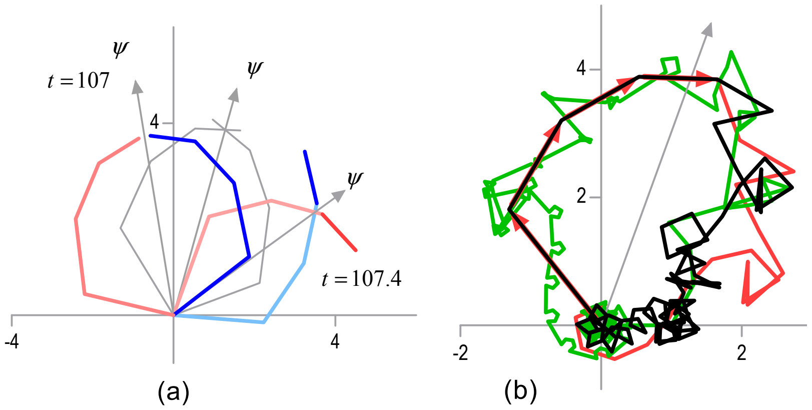

Figure 27. **(a)** $\mathrm{P}\left(\eta_5\left(\tfrac{1}{2}+it\right)\right)$ is shown as in Figure 26(c) with a wider interval in t and no overlap of the *kappa* vectors. **(b)** In red $\mathrm{P}(h_{5,\tau}(s))$ is shown which follows $\mathrm{P}(\ell_{5,\kappa}(s))$, see Figure 26(a) above and in black $\mathrm{P}(\bar{h}_{5,\tau}(s))$ is shown which follows the proximal $\mathrm{P}\left(\eta_{5,\kappa l}\left(\tfrac{1}{2}+it\right)\right)$.

The difference between $\mathrm{P}(h_{l,\tau}(s))$ in Figure 26(a) and $\mathrm{P}(\bar{h}_{l,\tau}(s))$ in Figure 27(b) after the *kappa* vectors are clearly illustrated.

3.5.2. The separation of proximal and distal parts of $\mathrm{P}(\eta_l(s))$ for $l = \kappa + 1$ when $|\vec{\mathcal{R}}_r| \cong |\vec{m}|$

We will consider $l = \kappa + 1$. The vectors of $\mathrm{P}(\eta_{l,n}(s))$ and $\mathrm{P}(h_{l,r}(s))$ get smaller as m and r rise, but since they are superimposed complementary pathways at non-trivial zeros, there must be a crossover-point where $|\vec{\mathcal{R}}_r| \cong |\vec{m}|$.

If we let this occur when $r = a$ and when $m = al$ we have an $\mathcal{R}_r$ structure in $\mathrm{P}(\eta_l(s))$ with a representative $\vec{m}$ with $l|m$ near the point-of-inflection at $m = \left[\left(e^{\frac{q_{\bar{r}}\pi}{tl}} - 1\right)^{-1}\right]$ associated with a magnitude $|\vec{m}| = (l-1)m^{-\sigma}$. The $q_{\bar{r}}$ of interest is $r = \frac{q_{\bar{r}}}{2}$ because we choose to have $r < l$. This gives us $al \cong \left[\left(e^{\frac{2a\pi}{tl}} - 1\right)^{-1}\right]$ and if we let $a \approx l$ we have $a = \left[\left(e^{\frac{2\pi}{t}} - 1\right)^{-1/2}\right]$ which of course is *kappa*. At the separation of proximal from distal complimentary pathways $\mathrm{P}(\eta_{l,n}(s))$ and $\mathrm{P}(h_{l,r}(s))$, the magnitudes of $|\vec{\mathcal{R}}_r|$ and $|\vec{m}|$ are approximately equal; $|\vec{\mathcal{R}}_\kappa| \cong |\overrightarrow{l\kappa}|$.

A refinement that can occasionally make a material difference when choosing the nearest integer is to be aware that $m = \left[\left(e^{\frac{q_{\bar{r}}\pi}{tl}} - 1\right)^{-1}\right]$ looks at the difference in arguments of neighbouring vectors looking forward from m as in $t\ln\left(\frac{m+1}{m}\right)$ whilst one might look back and find a better match with $t\ln\left(\frac{m}{m+1}\right)$ which yields $m = \left[\left(1 - e^{\frac{-q_{\bar{r}}\pi}{tl}}\right)^{-1}\right]$. This refinement is included for completeness with the average expressed in Equation (5).

3.5.2. An example of the paths of the mid-parts of the kappa vectors

In Figure 28 three plots at different values of t all with $\sigma = \frac{1}{2}$ are shown to illustrate the intersections of the *kappa* vectors over an interval in t. The movement of the principal pathways, shown with dashed lines over the same interval in t, differ, being greatest for $\mathrm{P}(h_{l,\kappa}(s))$ which is a consequence of the differentials having different magnitudes.

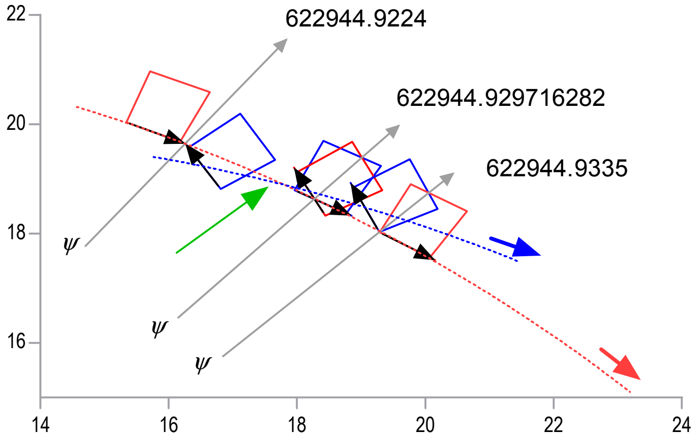

Figure 28. Three plots of the final 4 vectors of $\mathrm{P}(h_{l,\kappa}(s))$ in red and $\mathrm{P}(\ell_{l,\kappa}(s))$ in blue with the *kappa* vectors shown as black arrows. The centre plot is for the 1,041,452th zero at $t_i =$ 622944.9297 but the *kappa* vectors overlap throughout the short interval in t which ends just before 622944.9335. The crossing of the *kappa* vectors at the zero is not a crossing at their mid-points but rather in their tail sections. The arc in dashed red is $\frac{1}{2}\left(h_{l,\kappa}(t) + h_{l,\kappa-1}(t)\right)$ and the arc in dashed blue is $\frac{1}{2}\left(\ell_{l,\kappa}(t) + \ell_{l,\kappa-1}(t)\right)$ over an interval in t from 622944.919 to 622944.944; these dashed lines cross at the green arrow ahead of ψ for the t_i since the zero lies with an intersection in the tails of the last ¼ of the vectors.

In Figure 28 for a fixed σ, it can be appreciated that over the same interval in t, the point $h_{l,\kappa}(t)$ has moved much further than $\ell_{l,\kappa}(t)$. Indeed this is no surprise since $\left|\frac{\partial h_{l,\kappa}(s)}{\partial t}\right| > \left|\frac{\partial \ell_{l,\kappa}(s)}{\partial t}\right|$. Non-trivial zeros occur in the vicinity of the crossing of these arcs. The next non-trivial zero occurs when $h_{l,\kappa}(s)$ catches up with $\ell_{l,\kappa}(s)$.

3.6. The function $\lambda_l(s,x)$ identifies short intervals in t capable of hosting non-trivial zeros

The short finite series $\ell_{l,\kappa}(s)$, locates intervals in t which can host non-trivial zeros between upper and lower bounds on the critical-line. Half of the *lambda* function, here $h_{l,\kappa}(s)$, is not required since the intersection between $\vec{\mathcal{L}}_\kappa$ and ψ is sufficient. Since t specifies both ψ and κ and we let $l = \kappa + 1$ surprisingly few calculations are required. This is similar to section 3.2.4. Importantly the interval in t associated with intersection of the *kappa* vectors gets narrower as t rises, and since κ and l grow slowly with t the computational burden rises very slowly with t.

In this exercise an Excel spread sheet followed t rising from 1,131,941.5 to t = 1,131,947.5 in increments of 0.0001. Values of t were noted when $\vec{\mathcal{L}}_\kappa$ intersected with ψ and those values immediately preceding intersection (Lower bound) and those immediately following intersection (Upper bound) appear in Table 2. The bounds are therefore conservative as they lie outside of $x = 0$ and $x = 1$. In this interval $\kappa = 424$ and $l = 425$. In Table 2, if the column x contains [1→0] it indicates that the Lower bound is just outside an intersection of $x = 1$ and the Upper bound is just outside an intersection starting after $x = 0$.

Table 2.

$t = 1131940 + value\ in\ the\ table$				
x	$\boldsymbol{\lambda(s,x) = 0}$ **Lower bound**	$\boldsymbol{t_i}$	$\boldsymbol{\lambda(s,x) = 0}$ **Upper bound**	$\boldsymbol{\Delta t}$ **Interval**
[1→0]	1.8822	+ 1.8841	1.8887	0.0064
[0→1]	2.5649	+ 2.5708	2.5734	0.0084
[1→0]	2.9114	+ 2.9142	2.9208	0.0093
[0→1]	3.4800	+ 3.4852	3.4875	0.0074
[1→0]	3.9858	+ 3.9882	3.9938	0.0079
[0→1]	***4.4661***	***+ 4.4718***	***4.4743***	***0.0081***
[1→0]	4.9266	+ 4.9288	4.9337	0.0070
[0→1]	5.3665	+ 5.3696	5.3709	0.0043
[1→0]	6.1715	+ 6.1726	6.1753	0.0037
[0→1]	6.6373	+ 6.6413	6.6431	0.0057
[1→0]	7.0666	+ 7.0683	7.0723	0.0056

Intervals in t in which $\lambda_l(s,x)$ hosts 11 non-trivial zeros from t_i =1131941.8841 to t_i =1131947.0683. The figures are added to 1131940 to give t. The middle row shown in bold is the 2,000,000 th non-trivial zero.

The next exercise looked at the same interval of t covered by Table 2. In this interval each magnitude is of $\lambda_l(s,x)$ with $x = \frac{1}{2}$. In Figure 29 the 11 minima of the logarithm of the magnitudes fall very close to the 11 non-trivial zeros, and the tightness of the upper and lower bounds is evident.

doi:10.20944/preprints201703.0121.v1

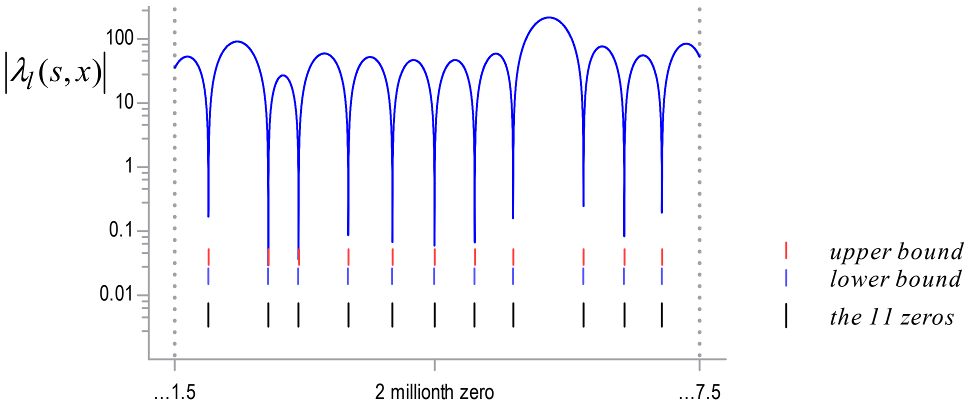

Figure 29. A plot of the logarithm of the magnitude of $\lambda_l(s,x)$ with $x=\frac{1}{2}$; the upper and lower bounds indicate the limits of the intersection of the *kappa* vectors.

3.6.1. How good is the intersection of $\vec{\mathcal{L}}_\kappa(t)$ with ψ at detecting zeros at low values of t ?

The exercise in section 3.2.4 above was repeated for $\operatorname{Im}(s)$ over the interval $t=226$ to $t=242$ with results appearing in Table 3. In this interval $\kappa=6$ and $l=7$. Intersection equates to the maximum interval in t for which $\lambda_l(s,x)$ could host a non-trivial zero.

Table 3.

$\boldsymbol{\lambda(s)=0}$ **Lower bound**	$\boldsymbol{t_i}$	$\boldsymbol{\lambda(s)=0}$ **Upper bound**	$\boldsymbol{\Delta t}$ **Interval**
227.3533	227.4214	227.5012	0.1479
229.2312	229.3374	229.4338	0.2026
231.0702	**231.2502**	**232.1655**	**1.0953**
231.0702	**231.9872**	**232.1655**	**1.0953**
233.6252	233.6934	233.8016	0.1764
236.4073	236.5242	236.5967	0.1894
237.6827	237.7698	237.9533	0.2706
239.3638	239.5555	239.6391	0.2753
240.9733	241.0492	241.2516	0.2783

In Figure 30 the magnitudes of $\lambda_l(s,x)$ with $x=\frac{1}{2}$ are shown with their upper and lower bounds and the location of published non-trivial zeros.

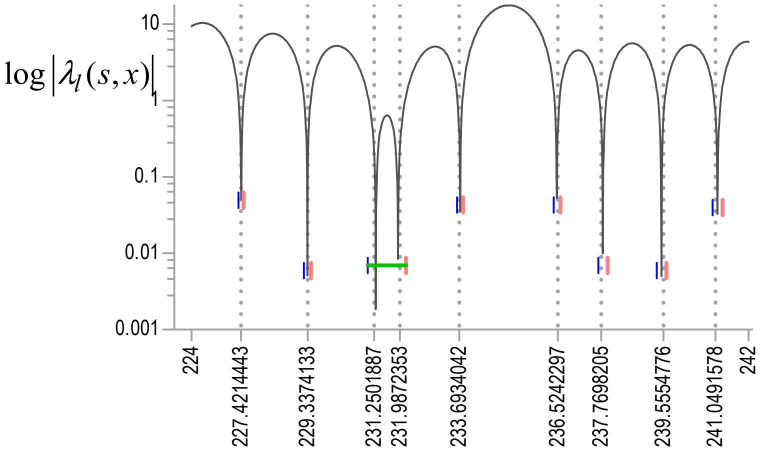

Figure 30. A plot of $\log_{10}|\lambda_l(s,x)|$ against t with $x=\frac{1}{2}$. In red is shown the upper bound and in blue the lower bound. The dotted lines are the locations of the known non-trivial zeros. One interval shown in green hosts two zeros.

In Figure 30 two non-trivial zeros are hosted in the same interval in t. In Figure 31 the paired pathways are illustrated at four values of t in this interval to show the underlying mechanism.

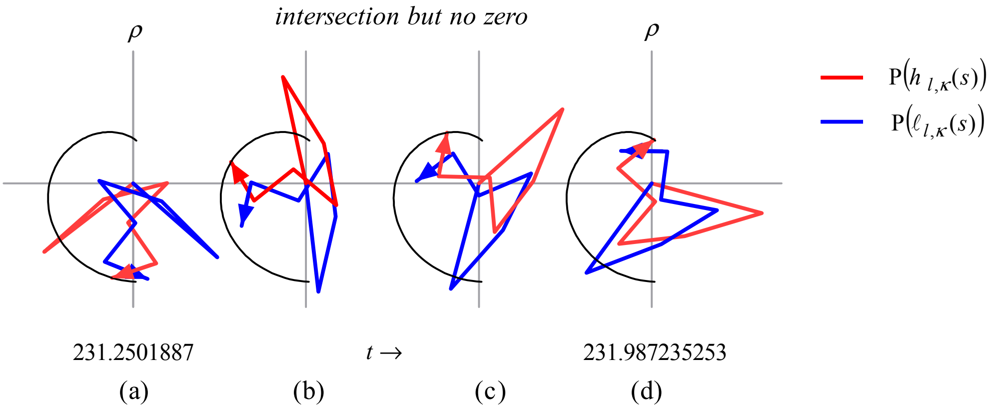

Figure 31. Four sequential plots, **(a)** with t_i as shown, **(b)** $t = 231.6$, **(c)** $t = 231.8$ and **(d)** with t_i as shown. Plots of $\mathrm{P}(h_{l,\kappa}(s))$ appear in red and $\mathrm{P}(\ell_{l,\kappa}(s))$ in blue over the interval between the two zeros during which the *kappa* vectors (arrows) are continually overlapping. The black arc in each figure is a plot of the movement of the tip of the $\vec{\mathcal{R}}_\kappa$ vector i.e. the function $h_{l,\kappa}(t)$ for $\sigma = \frac{1}{2}$ over a slightly wider interval in t.

In Figure 31 it can be appreciated how two non-trivial zeros can be hosted in the same interval of t. This insensitivity in $\lambda_l(s,x)$ does not weaken the symmetry arguments in their support of the validity of RH.

Appendix A4 describes the empirical relationship between x, $\dot{\kappa}$ and the angle of intersection of the *kappa* vectors at a number of non-trivial zeros. Appendix A4 illustrates two extremes of angles of intersection of the *kappa* vectors at non-trivial zeros and gives an example of "opportunistic" superstructures in a proximal pathway preceding the *kappa* vector in Appendix A5.

3.6.2. A comparison of $\eta_l(t)$ and $\lambda_l(t)$ for fixed $\sigma = \frac{1}{2}$

By Equation (78) $\eta_l(s)$ and $\lambda_l(s,x)$ only differ by $\zeta_{\kappa l}(s)$ and equate at the non-trivial zeros when Euler's *zeta* vanishes. In this exercise plots of $\eta_l(t)$ and $\lambda_l(t)$ can be seen to be similar and the difference at one value of t is illustrated to be $\zeta_{\kappa l}(t)$ through superposition of the pathways.

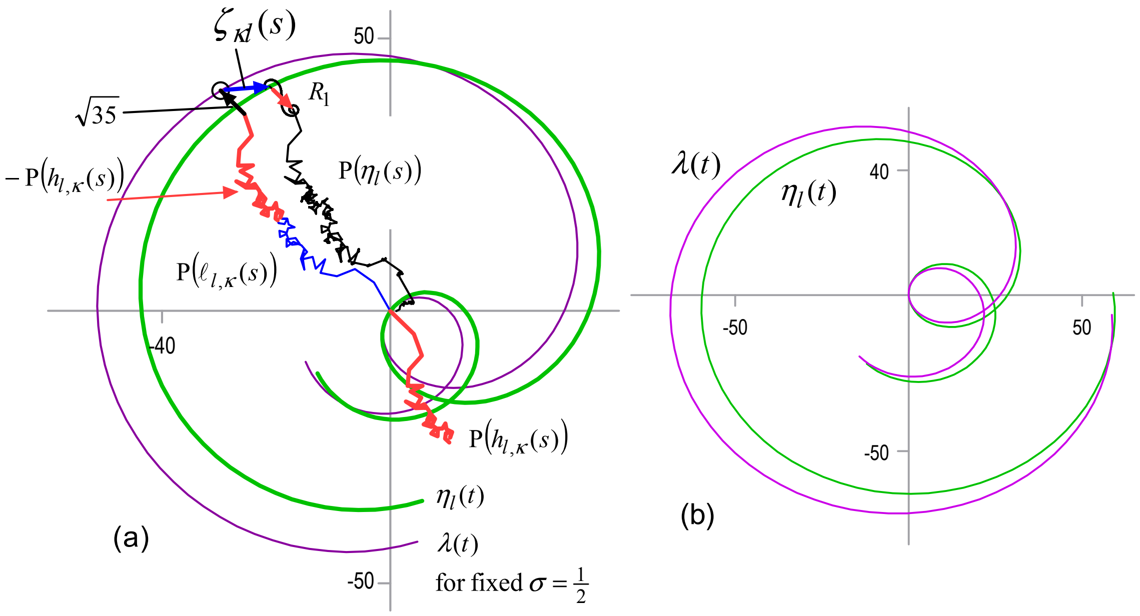

Figure 32. (a) Plots of $\eta_l(t)$ in purple and $\lambda_l(t)$ in green for $\sigma = \frac{1}{2}$ over the interval $t = 7187.33269$ to $t = 7188.83269$ embracing the 6,914th zero with $\kappa = 34$, $l = 35$ and $x = 0.5$. **(b)** The same two curves but with $l = 67 = [\tau/\kappa]$.

In Figure 32(a) the arcs are similar but equate only at the non-trivial zero. The other places where the arcs cross are not at the same value of t. Pathways are shown for $t = 7187.70269$ showing that the difference between $\lambda_l(s) = \ell_{l,\kappa}(s) - h_{l,\kappa}(s)$ and $\eta_l(s)$ is $\zeta_{\kappa l}(s)$ as indicated with a blue vector. The difference between $\lambda_l(s)$ and $\eta_l(s)$ is $\zeta_{\kappa l}(s)$, which is plotted in Figure 33 below for $t = 7187.70269$ taken from Figure 32 above in which the blue vector is illustrated.

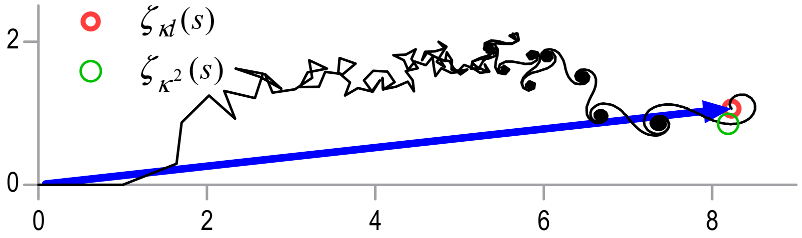

Figure 33. A plot of $\mathrm{P}(\zeta_{\kappa l}(s))$ from Figure 32(a) above in which $l = \kappa + 1$. The end point is not far from $\zeta_\tau(s)$. The point $\zeta_{\kappa^2}(s)$ is also shown. If t is very large and $\zeta_{\kappa l}(s)$ is based on $l = \kappa + 1$ then the term $\zeta_{\kappa l}(s)$ will not completely disappear when $s \in \{\rho\}$.

Figure 33 shows that $\zeta_{\kappa l}(s)$ is not far from $\zeta_\tau(s)$, $\zeta_{\kappa^2}(s)$ is also shown. If t is very large and $\zeta_{\kappa l}(s)$ is based on $l = \kappa + 1$ then the term $\zeta_{\kappa l}(s)$ will not completely disappear when $s \in \{\rho\}$. At most we can let l rise until $\kappa l \approx \tau$ when the final pseudo-convergence of Euler's *zeta* is reached. We should let $l = [{}^{\tau}/_{\kappa}]$ to justify ignoring the partial Euler's *zeta* term when $\zeta_{\kappa l}(\rho) \approx 0$.

3.7. Simultaneous zeros for $\eta_l(s)$: a metaphor for a ρ_u

This section illustrates how a loop in $\eta_l(\sigma)$ for fixed t, which allows a double-point $\eta_l\left(\frac{1}{2} + it_i\right) = 0 \approx \eta_l(1 + it_i)$, can be appreciated in terms of $\eta_l(s) = \zeta_{\kappa l}(s) + \ell_{l,\kappa}(s) - h_{l,\kappa}(s)$. In Figure 34 (a) pathways are shown for $\ell_{l,\kappa}(s)$ and $h_{l,\kappa}(s)$ since $\zeta_{\kappa l}(\rho) \approx 0$. In Figure 34(b) all three pathways are shown together with $\eta_l(\sigma)$. This example uses the 1675^{th} non-trivial zero $t_i = 2170.787075$ for which $\kappa = 19$ and chosen since $\frac{\ln(20)}{2\pi\, t_i} = 1035.00017$ which being very close to an integer places a double-point close to zero. The loop provides a metaphor for the pathways required for a ρ_u to disprove RH. Importantly we are concerned about the relationships between the pathways.

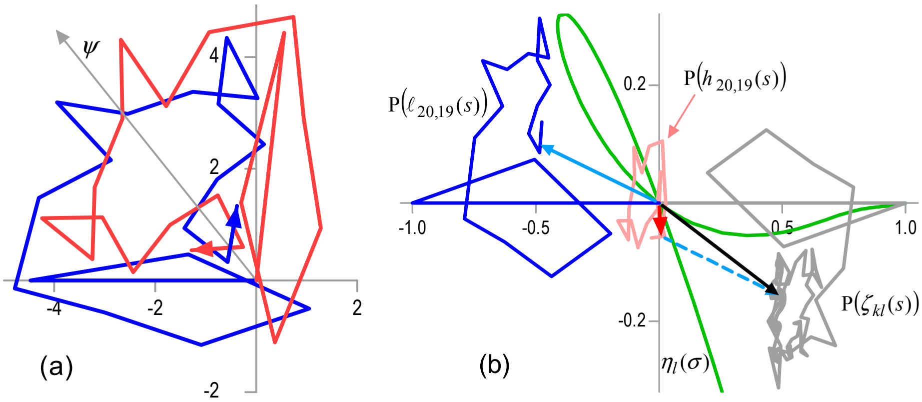

Figure 34. Pathways $\mathrm{P}(h_{l,\kappa}(s))$ in red and $\mathrm{P}(\ell_{l,\kappa}(s))$ in blue for $t_i = 2170.787075$ at **(a)** $\sigma = \frac{1}{2}$ and **(b)** $\sigma = 1$, **(b)** also shows $\mathrm{P}(\zeta_{\kappa l}(s))$ in grey. Plots are with $\kappa = 19$, $l = 20$. The fraction $x = 0.254$ which can be seen in (a) to be the intersection of the *kappa* vectors at their crossing with ψ. In (b) the black vector $\zeta_{\kappa l}(s)$ clearly equates to $h_{l,\kappa}(s) - \ell_{l,\kappa}(s)$, with vectors $h_{l,\kappa}(s)$, a red arrow and $-\ell_{l,\kappa}(s)$, a dashed blue arrow. In green is the loop of $\eta_l(\sigma)$ with its double-point at zero. The light blue arrow is $\ell_{l,\kappa}(s)$.

In Figure 34 it is clear that $\eta_l(s) = \zeta_{\kappa l}(s) + \ell_{l,\kappa}(s) - h_{l,\kappa}(s) \approx 0$. In this way it can be seen that the trivial zero of the double-point comes about from the unique orientation of $\mathrm{P}\left(h_{l,\kappa}(s)\right)$ and $\mathrm{P}\left(\ell_{l,\kappa}(s)\right)$ in relation to $\mathrm{P}(\zeta_{\kappa l}(s))$. This orientation would not exist if l were changed, to any other value than an integral power of l. It is for this simple reason that simultaneous zeros for some hypothetical t_u within the critical-strip, could not be generated by a similar mechanism of collapse of a $\mathrm{P}(\eta_l(s))$ over an interval embracing σ_α and σ_β. To illustrate the effect of a change in l the exercise was repeated with $l = 22$ and the results are shown in Figure 35.

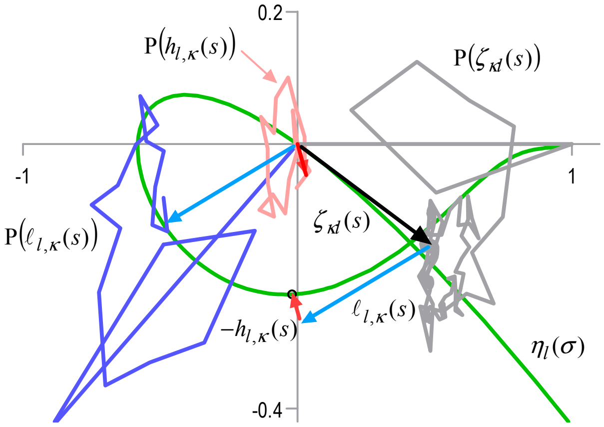

Figure 35. Parameters are as in Figure 34 above but with $l = 22$. $\mathrm{P}(\zeta_{\kappa l}(s))$ is unchanged but $\mathrm{P}(\ell_{l,\kappa}(s))$ in blue and $\mathrm{P}(h_{l,\kappa}(s))$ in pink are both rotated through different angles. The summation $\zeta_{\kappa l}(s) + \ell_{l,\kappa}(s) - h_{l,\kappa}(s)$ reaches the green line of $\eta_l(\sigma)$ for $\sigma = 1$ at the point in the back circle but not at zero. The black, blue and red arrows represent the same vectors as in Figure 34. There is still a double-point in $\eta_l(\sigma)$ but this is not at zero. The loop in green is seen to pass through zero for $\sigma = \frac{1}{2}$ as expected.

3.8. The derivatives of $\eta_l(s)$ and the related series $h_{l,r}(s)$, $\ell_{l,n}(s)$ and $\zeta_{l,\kappa l}(s)$

If RH is false, and the functional equation applies, then there must be an s for which $\eta'_l(s) = 0$ with $\mathrm{Re}(s) < \frac{1}{2}$. This is equivalent to saying that if $\mathrm{Re}(s) > \frac{1}{2}$ for all s which satisfy $\eta'_l(s) = 0$ then RH is true. In this section it will be apparent why, when $\mathrm{Re}(s) < \frac{1}{2}$ we cannot have $\eta'_l(s) = 0$.

Consider first the simple thought experiment in which we ignore $\zeta_{\kappa l}(s)$ and let

$$\lambda(s) := \lambda_l(s, x) \text{ with } l = \left[\frac{\tau}{\kappa}\right] \text{ and } x = 1 \tag{79}$$

such that the behaviour of $\lambda(s)$ becomes a surogate for the behaviour of $\eta_l(s)$ and we ask about the non-trivial zeros of $\lambda(s)$ and the zeros of $\lambda'_l(s)$. When $\mathrm{Re}(s) < \frac{1}{2}$ and falls then $\mathrm{P}(h_{l,\kappa}(s))$ grows larger more rapidly than $\mathrm{P}(\ell_{l,\kappa}(s))$ grows. When $\mathrm{Re}(s) > \frac{1}{2}$ and rises then $\mathrm{P}(h_{l,\kappa}(s))$ shrinks more rapidly than $\mathrm{P}(\ell_{l,\kappa}(s))$ shrinks. These behaviours explain why the *kappa* vectors separate one way on one side of the critical-line and the other way on the other side.

When changes in magnitude occur these are not a uniform scaling along the pathway but have a proximo-distal gradient. In $\mathrm{P}(h_{l,\kappa}(s))$ the effects are greatest proximally and in $\mathrm{P}(\ell_{l,\kappa}(s))$ the effects are more marked distally. These differences in behaviour account for why the separated *kappa* vectors lie on one side of ψ when $\sigma < \frac{1}{2}$ and on the other side when $\sigma > \frac{1}{2}$.

The derivatives provide a means of counteracting these two behavioural differences. Differentiation reverses the direction of every vector but more importantly it multiplies each $\vec{\mathcal{R}}_r$ by $\ln(\frac{\nu}{r})$ and each $\vec{\mathcal{L}}_n$ by $\ln(ln)$, and so since $n \equiv r$ it can be appreciated how both behavioural differences outlined above are overcome only when $\sigma > \frac{1}{2}$.

The non-trivial zeros of $\lambda(s)$ lie on the critical-line and the zeros of $\lambda'_l(s)$ to its right, but $\lambda(s)$ is not $\eta_l(s)$. We have no anxieties over ignoring $x = f(t)$, since this parameter is a refinement that breaks no symmetry but merely displaces the values of the non-trivial zeros of *lambda* a little from each neighbouring t_i. However, we do have anxieties over $\zeta_{\kappa l}(s)$ but these are easily dismissed. The term $\zeta_{\kappa l}(s)$ vanishes in the undifferentiated formulation at a non-trivial zero and can be comfortable ignored, but $\zeta'_{\kappa l}(s)$ does not vanish in $\eta'_l(s)$ and it cannot be ignored. Nonetheless it can be shown that this causes no issues.

Differentiation of $\left|\vec{\mathcal{R}}_r\right| = \sqrt{l}\, \nu^{\left(\frac{1}{2}-\sigma\right)} r^{(\sigma-1)}$ with respect to σ gives

$$\left|\frac{\partial \vec{\mathcal{R}}_r}{\partial \sigma}\right| = \sqrt{l} \nu^{\left(\frac{1}{2}-\sigma\right)} r^{(\sigma-1)} \ln\left(\frac{\nu}{r}\right) = \ln\left(\frac{\nu}{r}\right) \left|\vec{\mathcal{R}}_r\right|,$$
$$\text{or } \left|\frac{\partial \vec{\mathcal{R}}_r}{\partial \sigma}\right| = \sqrt{l}\, \nu^{\left(\frac{1}{2}-\sigma\right)} \left(\frac{q_{\bar{r}}}{2}\right)^{(\sigma-1)} \ln\left(\frac{2\nu}{q_{\bar{r}}}\right) \text{ with } q_{\bar{r}} \in \chi_l \tag{80}$$

which are always positive since r is never greater than ν and the argument becomes

$$\arg\left(\frac{\partial \vec{\mathcal{R}}_r}{\partial \sigma}\right) = \frac{5\pi}{4} - t\ln\left(\frac{l}{r}\left[\frac{\nu}{l}\right]\right) = \arg\left(\vec{\mathcal{R}}_r\right) + \pi. \tag{81}$$

Since $\vec{\mathcal{L}}_n = -l^{(1-s)} n^{-s}$

$$\left|\frac{\partial \vec{\mathcal{L}}_n}{\partial \sigma}\right| = l^{(1-\sigma)} n^{-\sigma} \ln(ln) = \ln(ln) \left|\vec{\mathcal{L}}_n\right| \tag{82}$$

with an argument

$$\arg\left(\frac{\partial \vec{\mathcal{L}}_n}{\partial \sigma}\right) = \pi - t\ln(ln). \tag{83}$$

The series are then simply

$$\frac{\partial h_{l,\kappa}(s)}{\partial \sigma} = \sum_{r=1}^{\kappa} \frac{\partial \vec{\mathcal{R}}_r}{\partial \sigma} \tag{84}$$

and

$$\frac{\partial \ell_{l,\kappa}(s)}{\partial \sigma} = \sum_{n=1}^{\kappa} \frac{\partial \vec{\mathcal{L}}_n}{\partial \sigma}. \tag{85}$$

The differential of the partial *zeta* function is

$$\frac{\partial \zeta_{\kappa l}(s)}{\partial \sigma} = -\sum_{m=1}^{\kappa l} \ln(m) m^{-\sigma} (\cos(t \ln(m)) - i\sin(t\ln(m))). \tag{86}$$

Clearly

$$\frac{\partial \eta_l(s)}{\partial \sigma} = \frac{\partial \zeta_{\kappa l}(s)}{\partial \sigma} + \frac{\partial \ell_{l,\kappa}(s)}{\partial \sigma} - \frac{\partial h_{l,\kappa}(s)}{\partial \sigma}, \tag{87}$$

however,

$$\frac{\partial \eta_l(s)}{\partial \sigma} = \frac{\partial \zeta_{\kappa l}(s)}{\partial \sigma} + \frac{\partial \lambda_l(s,x)}{\partial \sigma} \tag{88}$$

is less helpful than Equation (78) since the term $\frac{\partial \zeta_{\kappa l}(s)}{\partial \sigma}$ does not vanish at the zeros of the differential.

3.8.1. An example of $\lambda'_l(s) = 0$

In Figure 36 three pairs of pathways are plotted for the matched finite series $h_{l,\kappa}(s)$ and $\ell_{l,\kappa}(s)$ each with 34 terms. Added on to the end of $\mathrm{P}\left(\ell_{l,\kappa}(s)\right)$ in blue are shown the $\mathrm{P}(\zeta_n(s))$ in green. The index of negation is set at $l = 64$, with the justification for that value explained below. When $\sigma = \frac{1}{2}$ the pathways are mirror-images about the line of reflection ψ. The value of t has been increased from $t = 7188.322595$ where the nearby ρ_i exists. Since near this t_i there is a zero for $t = \frac{2\pi(793)}{\ln(2)} = 7188.323185$ at $\sigma = 1$ and so there exists a double-point in the function $\eta_l(\sigma)$ and a loop in that function over an interval in σ embracing $\sigma = \frac{1}{2}$ and $\sigma = 1$, which has a minimum $\frac{\partial \eta_l(s)}{\partial \sigma}$ near the apex of the loop.

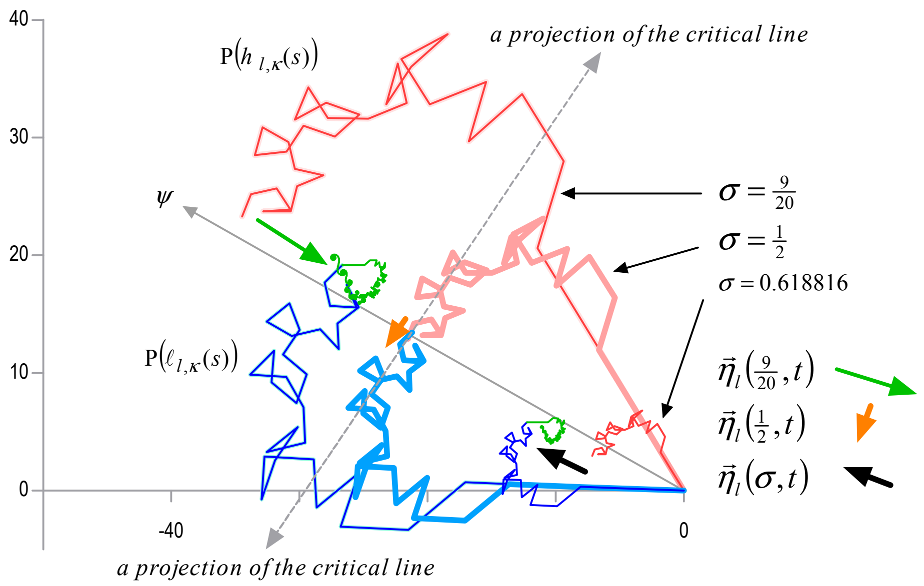

Figure 36. Three plots of $\mathrm{P}(h_{l,\kappa}(s))$ in red and $\mathrm{P}(\ell_{l,\kappa}(s))$ in blue for $t = 7188.332453$ and the three real domains $\sigma = \frac{9}{10}$, $\sigma = \frac{1}{2}$ and σ =0.618816. The three arrows are approximations for vectors representing $\eta_l(\sigma)$ shown in green, orange and black. The line of reflecton ψ is shown. The critical-line is projected as a normal to ψ, crossing it and passing through the $\sigma = \frac{1}{2}$ pathway's *kappa* vectors. The breaking of symmetries either side of the projected line are clear.

Minor adjustments to t from t_i soon establish the values of both t and σ for which $\eta'_l(s) = 0$ when $\frac{\partial \eta_l(s)}{\partial \sigma} = -i\frac{\partial \eta_l(s)}{\partial t} = 0$. If we do this for $l = 2$ we may be disappointed because unlike the set $\{t_i\}$ which are independent of l the zeros of $\eta'_l(s) = 0$ are dependent on l. Indeed, even though the zeros of $\eta_l(\sigma)$ at $\sigma = 1$ are invariant under integral powers of l, i.e. l^2, l^3, l^4, l^a with $a \in \mathbb{N}$ the zeros of the differential $\eta'_l(s) = 0$ are sensitive to a.

To examine the differential $\frac{\partial \eta_l(s)}{\partial \sigma}$ when approximated by the difference $\frac{\partial \ell_{l,\kappa}(s)}{\partial \sigma} - \frac{\partial h_{l,\kappa}(s)}{\partial \sigma}$ we determine $\kappa = 34$ and move to a new index of negation such that $l > \kappa + 1$. Changing l alters and can annihilate loops in $\eta_l(\sigma)$ but we can choose an integral power of 2 and the nearest is 64.

Figure 37 uses $l = 64$ and shows a loop for $t_i = 7188.322595$ in blue and a cycloid-like curve in $\eta_l(\sigma)$ for $t_c = 7188.332453$ over $\sigma = 0.45$ to 3 in black. There is also a cycloid-like curve in $\eta_l(t)$ with $\sigma_c = 0.618816$ in red, part of a prolate cycloid-like curve with $\sigma = \frac{1}{2}$ in green and a curtate cycloid-like curve with $\sigma = 1$ in orange.

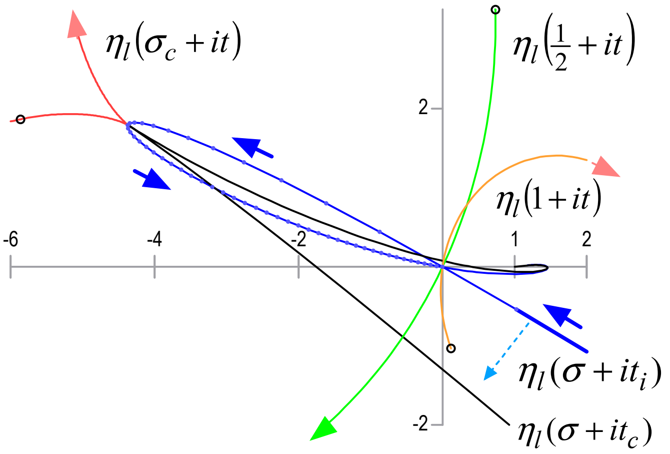

Figure 37. A loop in $\eta_{64}(\sigma)$ with t fixed at $t_i = 7188.322595$ is shown in blue with σ rising in the direction of the blue arrows. The loop passes through zero at $\sigma = \frac{1}{2}$ and at $\sigma = 1$. Equal increments in σ of 0.01 are indicated with dots between the double-points.

In Figure 37 it can be seen that adjusting t upwards narrows the blue loop and moves the double-point from zero towards the apex of the loop to produce in black the cycloid-like curve of $\eta_l(\sigma)$ at fixed $t = t_c$ with its apex at $\eta_l(\sigma_c + it_c)$ where it meets the cycloid-like curve of $\eta_l(t)$ for fixed $\sigma = \sigma_c$. Curves for $\eta_l(t)$ over short intervals embracing t_i are shown for $\sigma = \frac{1}{2}$ in green and for $\sigma = 1$ in red passing through the origin in roughly opposite directions. Each crosses $\eta_l(\sigma)$ at $\pi/2$. The loop in $\eta_l(\sigma)$, shown in blue, is with t fixed at $t_i \approx \frac{2\pi k}{\ln(64)}$ (Roman k and not Greek κ) so placing a double-point close to zero and providing a mental image of the type of curve that would have to exist if RH were false. We imagine that $t = t_u$ rather than $t_i \approx \frac{2\pi k}{\ln(l)}$ and the two values of σ at the double-point would be σ_α and σ_β. The following would still apply: the differentials would relate as follows $\frac{\partial\eta_l(s)}{\partial t} = i\frac{\partial\eta_l(s)}{\partial\sigma}$, and this is seen with the two curves of $\eta_l(t)$, in green and orange, crossing the two regions of $\eta_l(\sigma)$ at $\pi/2$ - note the directions indicated by the arrows. The blue loop has a minimum in its differential at the apex, at a value that lies closer to σ_α than σ_β; note the blue dots making rapid progress before slowing at the apex and then speeding up before finally slowing at high values of σ.

Adjustment of t allows the loop to shrink, and the two values of σ at the double-point approach one another until they meet at a value we call σ_c at which point we designate t as t_c. Two cycloid-like curves meet at $\eta_l(\sigma_c + it_c)$; in red $\eta_l(t)$ for $\sigma = \sigma_c$ over a short interval in t and in black $\eta_l(\sigma)$ for $t = t_c$ over an interval in σ. Just as in Figure 37 we have $(1 - \sigma_c) > (\sigma_c - \frac{1}{2})$, in our mental image $(\sigma_\beta - \sigma_c) > (\sigma_c - \sigma_\alpha)$. Since $\sigma_\beta = 1 - \sigma_\alpha$ if RH is false there must be a zero of the differential with $\sigma_c < \frac{1}{2}$. We now take part of Figure 36 and illustrate the directions, and schematically the magnitudes, of the partial differentials to produce Figure 38.

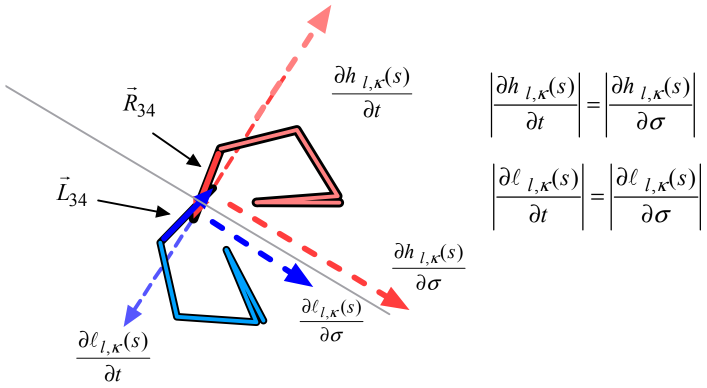

Figure 38. Detail from the centre of Figure 36 above. This shows the 34^{th} vectors of $\mathrm{P}(h_{l,\kappa}(s))$ and $\mathrm{P}(\ell_{l,\kappa}(s))$ where they cross ψ. The ends of these vectors are the points $h_{l,\kappa}(s)$ and $\ell_{l,\kappa}(s)$ and their partial differentials are shown with their relationships evident $\arg\left(\frac{\partial h_{l,\kappa}(s)}{\partial t}\right) = \arg\left(\frac{\partial \ell_{l,\kappa}(s)}{\partial t}\right) + \pi$ and $\frac{\partial h_{l,\kappa}(s)}{\partial t} = i\frac{\partial h_{l,\kappa}(s)}{\partial \sigma}$ whilst $\frac{\partial \ell_{l,\kappa}(s)}{\partial t} = -i\frac{\partial \ell_{l,\kappa}(s)}{\partial \sigma}$. Importantly $\left|\frac{\partial h_{l,\kappa}(s)}{\partial \sigma}\right| > \left|\frac{\partial \ell_{l,\kappa}(s)}{\partial \sigma}\right|$.

For values of t significantly removed from the vicinity of a $t \in \{t_i\}$ the *kappa* vectors of the pathways $\mathrm{P}(h_{l,\kappa}(s))$ and $\mathrm{P}(\ell_{l,\kappa}(s))$ do not cross one another. In the vicinity of a non-trivial zero the vectors may cross. Figure 36 shows the meeting of the pathways of $\mathrm{P}(h_{l,\kappa}(s))$ and $\mathrm{P}(\ell_{l,\kappa}(s))$, there is symmetry but no *"distal superposition"* since $t \notin \{t_i\}$. If we were to continue a little way further towards $\mathrm{P}(h_{l,\tau}(s))$ and $\mathrm{P}(\ell_{l,\tau}(s))$ by allowing r and n to rise above κ we would soon find paths sepatating and eventually $h_{l,\tau}(s) \neq \ell_{l,\tau}(s)$.

In Figure 39 there is a zero of the differential and it can be seen that $\mathrm{P}\left(\frac{\partial h_{l,\kappa}(s)}{\partial\sigma}\right)$ meets $\mathrm{P}\left(\frac{\partial \eta_{l,\kappa l}(s)}{\partial\sigma}\right)$ with their final vectors intersecting.

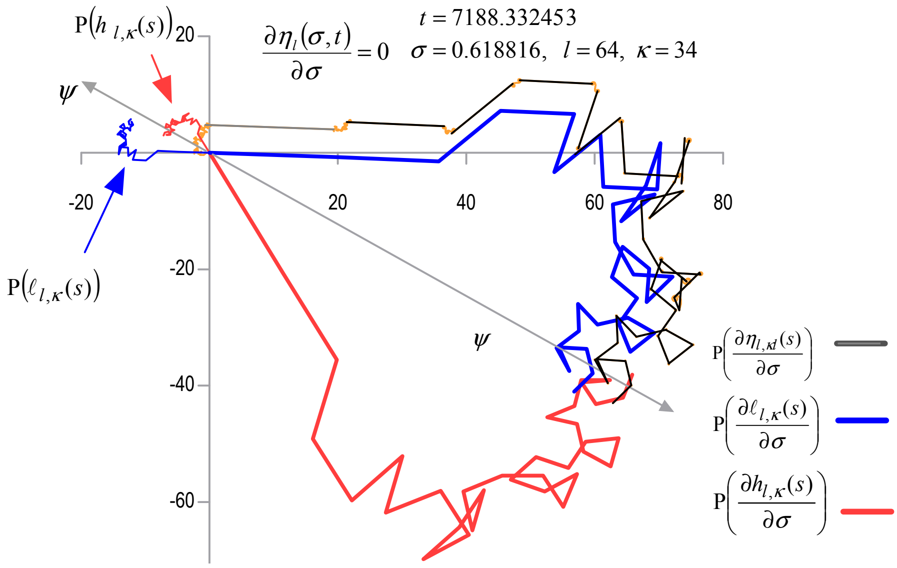

Figure 39. Near symmetry is restored when differentiation brings about a zero. The pathways $P(\ell_{l,\kappa}(s))$ in blue and $P(h_{l,\kappa}(s))$ in red (top left) are for a $\sigma > \frac{1}{2}$ as in Figure 36 above. Matched vectors have unequal magnitudes $|\vec{\mathcal{R}}_r| < |\vec{\mathcal{L}}_n|$, with $r = n$. However, on differentiation all vectors are reversed and enlarged. Enlargement is greatest for vectors in $P(h_{l\kappa}(s))$ and so $\eta'_l(s) = 0$ becomes possible but only with $\sigma > \frac{1}{2}$. $P\left(\frac{\partial \ell_{l,\kappa}(s)}{\partial\sigma}\right)$ is shown in blue, $P\left(\frac{\partial h_{l,\kappa}(s)}{\partial\sigma}\right)$ in red and $P\left(\frac{\partial \eta_{l,\kappa l}(s)}{\partial\sigma}\right)$, with every l^{th} vector in black is shown with the intervening vectors in orange.

The pathway $P\left(\frac{\partial \ell_{l,\kappa}(s)}{\partial\sigma}\right)$ does not meet $P\left(\frac{\partial \eta_{l,\kappa l}(s)}{\partial\sigma}\right)$ unless $P\left(\frac{\partial \zeta_{\kappa l}(s)}{\partial\sigma}\right)$ is added in, see Figure 40 .

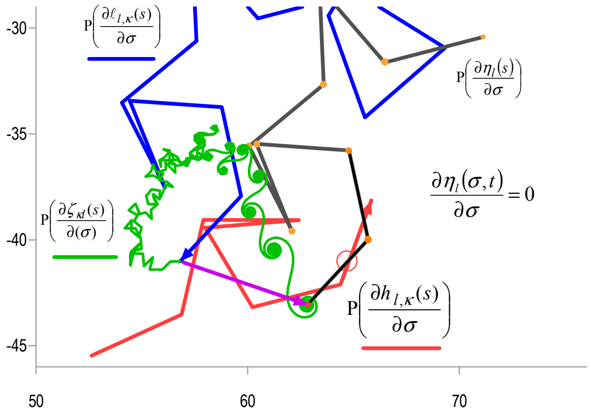

$t = 7188.332453, \quad \sigma = 0.618816, \quad l = 64, \quad \kappa = 34$

Figure 40. With s as shown and $l = 64$ the function $\frac{\partial \eta_l(s)}{\partial\sigma} \approx 0$. The black line is the end of $P\left(\frac{\partial \eta_{l,\kappa l}(s)}{\partial\sigma}\right)$ ending with $\vec{m}$ for $= 34x64 = 2176$. The orange dots lie at the end of every vector $\vec{m}$ and as can be seen the l^{th} vectors predominate in the pathway. The same number of terms 2176, is used for $\frac{\partial \zeta_{\kappa l}(s)}{\partial\sigma}$ (purple arrow) and its pathway $P\left(\frac{\partial \zeta_{\kappa l}(s)}{\partial\sigma}\right)$, which is shown in green, both start from the end of the *kappa* vector $\vec{\mathcal{L}}_\kappa$ terminating $P\left(\frac{\partial \ell_{l,\kappa}(s)}{\partial\sigma}\right)$, which is shown in blue. The $P(\zeta_{\kappa l}(s))$ ends at an $m = 2176$ in a red dot which is a little shy of $\tau = 2288$, but still very close to the final pseudo-convergence of Euler's *zeta*. The *kappa* vector of $P\left(\frac{\partial h_{l,\kappa}(s)}{\partial\sigma}\right)$ intersects with the κl vector of $\eta'_{l,\kappa l}(s)$ consistent with this being very close to a zero of the derivative.

In Figure 40 the $\frac{\partial \zeta_{\kappa l}(s)}{\partial\sigma}$ vector in purple runs between the ends of the *kappa* vectors but could have been placed to reflect x and would then have ended in the red circle.

doi:10.20944/preprints201703.0121.v1

Appendix A6 tabulates some example calculations in relation to the magnitudes of the vectors for the differentials.

4. Discussion

In 1826 Niels Abel wrote to his friend Bernt Holmboe saying it was a disgrace to base any proof on divergent series,

> *"Les séries divergentes sont en général quelque chose de bien fatal et c'est une honte qu'on ose y fonder aucune démonstration."*

which is often misquoted as "divergent series being an invention of the devil". In the work presented here, a partial Euler's *zeta* series to *tau* terms, designated $\zeta_\tau(s)$ with $\tau = \left[\left(e^{\frac{\pi}{t}} - 1\right)^{-1}\right]$ foreshortens the divergent series at a final pseudo-convergence such that in the critical-strip $\zeta_\tau(\rho) \approx 0$. Euler's *zeta* has a proximal pathway of *kappa* terms, with $\kappa = \left[\left(e^{\frac{2\pi}{t}} - 1\right)^{-\frac{1}{2}}\right]$ and a distal pathway thereafter which forms superstructures whose *principal-axes* can be considered to be vectors of a complementary finite series. Euler's *zeta* acquires convergence through negation of every l^{th} term which is multiplied by $l-1$. This is the function $\eta_l(s)$; a modification of Dirichlet's *eta*. The non-trivial zeros of $\eta_l(s)$ are also the non-trivial zeros of $\eta_{l+1}(s)$.

The infinite series $\eta_l(s)$ can be closely followed by the sum of three finite series in that $\eta_l(s) = \zeta_{\kappa l}(s) + \ell_{l,\kappa}(s) - h_{l,\kappa}(s)$. The first series, $\zeta_{\kappa l}(s) \approx 0$ when $s \in \{\rho\}$ if $\kappa l \approx \tau$. Since $\zeta_{\kappa l}(s) = 0$ at the domains of interest a suitable l allows $\zeta_{\kappa l}(s)$ to be placed to one side and focus turns to $\lambda_l(s) = \ell_{l,\kappa}(s) - h_{l,\kappa}(s)$. Or we can gild the lily by writing $\lambda_l(s,x) = \ell_{l,\kappa}(s,x) - h_{l,\kappa}(s,x)$ to refine the intersection of the *kappa* vectors.

For any given t, as long as $l \gg \kappa$, the matched vectors of the two series of $\lambda_l(s)$ share mirror-image arguments about a line of reflection ψ for all σ, but their magnitudes equate only when $\sigma = \frac{1}{2}$. These geometric constraints limit the non-trivial zeros to the critical-line as hypothesised by Riemann and force the differentials to the right.

If for some s with $\zeta_{\kappa l}(s) \neq 0$ there was also a $\zeta_{\kappa l}(s) = h_{l,\kappa}(s) - \ell_{l,\kappa}(s)$ this zero of $\eta_l(s)$ would not to be independent of l, such instances can only arise at the trivial zeros when t is an integral multiple of $\frac{2\pi}{\ln(l)}$ and $\sigma = 1$. However, if in the same way a hypothetical loop in $\eta_l(\sigma)$ for fixed t were imagined to generate a double-point, and that double-point were to be imagined at zero, then a change in l to $l+1$ would clearly preclude its existence in $\eta_{l+1}(\sigma)$ and since all non-trivial zeros have to exist for all values of l the imagined $s \notin \{\rho\}$. Loops are only preserved if l rises to l^a where $a \in \mathbb{N}$.

The two pathways $\mathrm{P}\big(h_{l,\kappa}(s)\big)$ and $\mathrm{P}\big(\ell_{l,\kappa}(s)\big)$ start from the origin and set off in different directions. If their terminal vectors $\vec{\mathcal{R}}_\kappa$ and $\vec{\mathcal{L}}_\kappa$ intersect over an interval in t there can be a zero of $\eta_l(s)$ in that interval. Either function alone, $h_{l,\kappa}(s)$ or $\ell_{l,\kappa}(s)$, can be used to identify those intervals, and every element of the set $\{t_i\}$ for $\sigma = \frac{1}{2}$ lies in such an interval.

The pathways have vectors with matching orientations that are invariant under changes in σ but their magnitudes are not invariant. In this analysis there is no room for a zero off the critical-line. If one were hypothesised to exist above or below $\frac{1}{2}$ then its partner could not come into existence by changing σ since $\vec{\mathcal{R}}_\kappa$ and $\vec{\mathcal{L}}_\kappa$ will either not intersect or if they do intersect they will not intersect with symmetry and that intersection will not be at ψ. When there is asymmetry a pathway's distal superstructures will not overlie the proximal vectors of the appropriate complimentary pathway.

A model for simultaneous zeros at the same t is possible in $\eta_l(s)$ when $t_i \cong \frac{2\pi k}{\ln(l)}$ since there will be a loop in $\eta_l(\sigma)$ for fixed t_i with a double-point near the origin $\eta_l\big(\frac{1}{2} + it_i\big) = 0 \cong \eta_l(1 + it_i)$, however the mechanics of such simultaneous convergence are sensitive to l and are driven by the principal orientation of the pathways in relation to their final collapse to $(1,0)$ as $\mathrm{Re}(s) \to \infty$. Were there a mechanism, capable of generating $\eta_l(\sigma_\alpha + it_i) = 0 = \eta_l\big(\sigma_\beta + it_i\big)$ which would disprove RH it would have to be a mechanism whose output is unaffected by changes in l.

No mechanism is capable of generating loops in $\eta_l(\sigma)$ which are stable under changes in l and also generate similar loops in $\eta_l(\sigma)$ that only appear at certain values of l e.g. when $t_i \cong \frac{2\pi k}{\ln(l)}$.

Furthermore, if there were a $\eta_l(\sigma_\alpha + it_i) = 0 = \eta_l(\sigma_\beta + it_i)$ and we then allowed $l \cong e^{\frac{2\pi k}{t_i}}$ there would be a requirement for two loops in $\eta_l(\sigma)$ for $t = t_i$ and a triple-point formed by the addition of $0 \cong \eta_l(1 + it_i)$. No pathway to convergence could be envisaged to behave in such a way though a rigorous proof along these lines has not been found, see Figure 41.

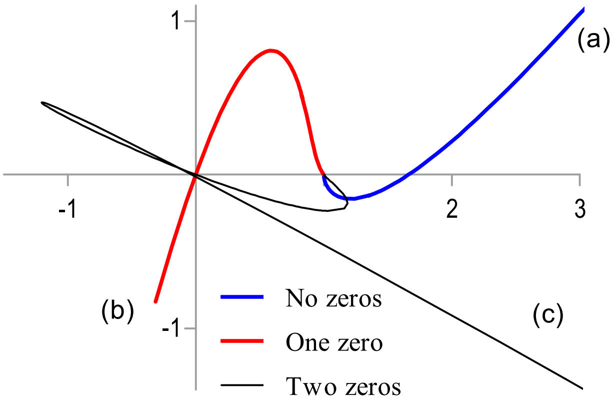

Figure 41. Three curves in $\eta_l(\sigma)$ for different values of t over a wide interval in t. The blue curve (a) has no zero, the red curve (b) has one zero, and the black loop has two zeros. A mechanism to create three zeros seems a challenge too far but one for which a rigorous proof has not been found.

Any loop in $\eta_l(\sigma)$ for some t with a double-point for two real parts $\sigma_a < \sigma_b$, not necessarily at zero, has two limbs, a primary one from σ_a reaching the apex of the loop and a secondary one from the apex to σ_b. At the apex, $\frac{\partial \eta_l(\sigma)}{\partial \sigma}$ will be a minimum and the apex will have a value of σ closer to σ_a than σ_b. If t is adjusted in the correct direction the interval between σ_a and σ_b will alter with σ_a rising to $\sigma_{a'}$ and σ_b falling to $\sigma_{b'}$. At some nearby $t = t_c$ the loop vanishes when $\sigma_{a'} = \sigma_{b'} = \sigma_c$ at which point $\frac{\partial \eta_l(\sigma_c)}{\partial \sigma} = 0 = -i\frac{\partial \eta_l(t_c)}{\partial t}$ with $\sigma_b - \sigma_c > \sigma_c - \sigma_a$. If we consider simultaneous zeros that refute RH and satisfy the functional equation we have a hypothetical loop $\eta_l(\sigma_\alpha + it_i) = 0 = \eta_l(\sigma_\beta + it_i)$ and this loop vanishes at a nearby t_c when $\frac{\partial \eta_l(\sigma_c)}{\partial \sigma} = 0 = -i\frac{\partial \eta_l(t_c)}{\partial t}$ with $\sigma_\beta - \sigma_c > \sigma_c - \sigma_\alpha$ giving $\frac{\partial \eta_l(\sigma_c)}{\partial \sigma} = 0$ only when $\sigma_c < \frac{1}{2}$. If RH is false the first differential of $\eta_l(s)$ must have zeros to the left of the critical-line.

It is easy to find examples of $\frac{\partial \eta_l(\sigma)}{\partial \sigma} = 0$ when $\sigma > \frac{1}{2}$ but the geometry of convergence of the pathway of the differential necessarily precludes $\frac{\partial \eta_l(s)}{\partial \sigma} = 0$ for $\mathrm{Re}(s) < \frac{1}{2}$. This is a corollary of RH.

The *lambda* function $\lambda_l(s,x)$ has perfect bilateral symmetry, and it limits its own zeros to the critical-line and those zeros have a strict link to the location of each ρ. *Lambda* gives some small uncertainty in the $\mathrm{Im}(\rho)$, with each zero hosted in a narrow imaginary interval with the uncertainty related to $f(x)$, but the $\mathrm{Re}(\rho)$ is limited to $\frac{1}{2}$. There is a relationship between x and t that is evident from calculations at low values of t. That relationship has not been fully characterised and has been set aside as it is of no material consequence for the arguments of this paper.

When Euler's *zeta* function is added to $\lambda_l(s)$ it breaks the symmetry since $\eta_{l,\kappa l}(s) = \zeta_{\kappa l}(s) + \ell_{l,\kappa}(s)$, and it is this symmetry breaking which permits the generation of loops in $\eta_l(\sigma)$ for fixed t. A loop in $\eta_l(\sigma)$ for fixed t has the double-point $\eta_l(\sigma_a + it) = \eta_l(\sigma_b + it)$ and raises the possibility of hypothetical simultaneous zeros. It is this same asymmetry which allows pathway collapse on rising σ outside of the critical-strip to drive all pathways towards their final demise at (1,0). Any such mechanism which generates loops in $\eta_l(\sigma)$ for fixed t would be highly sensitive to $\arg(\vec{\mathcal{R}}_1)$ and $arg(\psi)$ and so to changes in l. The clarity obtained by the function $\lambda_l(s)$ is to realize that it is the symmetry breaking of $\zeta_{\kappa l}(s)$ that permits $\eta_l\left(\frac{1}{2} + it_i\right) = \eta_l(1 + it_i) = 0$ when $t_i = \frac{2\pi k}{\ln(l)}$.

Once $l > \kappa$ the symmetries are evident and when $l = \left\lfloor \frac{\tau}{\kappa} \right\rfloor$ the term $\zeta_{\kappa l}(\rho) = 0$ allows $\lambda_l(s) = 0$ to reliably specify short regions of the imaginary axis which can host the non-trivial zeros of Riemann's *zeta* function. Importantly $\lambda_l(s) = 0$ confines the hosting regions to $\text{Re}(s) = \frac{1}{2}$.

5. Conclusions

Two finite vector series $h_{l,\kappa}(s)$ and $\ell_{l,\kappa}(s)$ are described whose paired terms have mirror-image arguments about a single line of reflection ψ but whose magnitudes equate only when $\text{Re}(s) = \frac{1}{2}$. The intersection of the final vector of either one of these series with the line of reflection allows identification of a small region of t capable of hosting a non-trivial zero. All non-trivial zeros have such a relationship with the line of reflection at the meeting of their final vectors. The cardinality of the sets rises slowly with $\text{Im}(s)$ allowing confidence that, no matter how high a region of t is contemplated, a comparatively short finite computation would allow identification of those hosting regions.

The intersection of the final vectors of the series is such that the non-trivial zeros of the Riemann *zeta* function can only come into existence when there is perfect symmetry. Symmetry breaking restricts the non-trivial zeros to $\text{Re}(s) = \frac{1}{2}$. The asymmetry of the differentials of the two series when $\text{Re}(s) \neq \frac{1}{2}$ is such that it immediately follows that the zeros of the differential can only be found when $\text{Re}(s) > \frac{1}{2}$. This relationship has implications for the nature of loops in $\eta_l(\sigma)$ for fixed t that together with the functional equation preclude all non-trivial zeros from having $\text{Re}(s) \neq \frac{1}{2}$.

Acknowledgments: This study was not funded nor part of paid employment. No funds have been received to covering the costs to publish in open access.

Author Contributions: The author was the sole contributor.

Conflicts of Interest: The author declares no conflict of interest.

Appendix A

A1. Near regular polygons and star-polygons

To describe regular star-polygons the Schläfli symbol $\{p/q\}$, is traditionally used where p and q are relatively prime [9]. Thus for the pentagon one would have $\{5/2\}$ and $\{5/3\}$. We will hijack this nomenclature and use $\left\{l/\left(\frac{q_{\bar{r}}}{2} mod(l)\right)\right\}$ to describe a family of structures: when $1 = q(mod\ l)$ we have clockwise near regular polygons and anticlockwise near regular polygons when $l - 1 = q(mod\ l)$, and when $l|q$ we have a structure in a pseudo-convergence, otherwise we have near regular star-polygons.

The pathways between any two pseudo-convergences contain the *point-of-inflection* and exhibit shapes whose geometries can be described as incomplete *near-regular polygons* or *near-regular star-polygons*. Imagine an l-sided regular polygon with its vertices enumerated $\varrho \in \mathbb{N}_0$ and counted clockwise allowing $\varrho > l - 1$ such that a modular arithmetic applies $\varrho = kl \equiv 0$ with k an integer. A family of new geometries arise when one vertex at $\varrho = 0$ of the regular l-sided polygon is connected to another vertex ϱ of the polygon counted in the clockwise direction and the process repeated until the first vertex is reached and the polygon itself or a star-polygon is created. We will allow $\varrho \in \mathbb{N}_0$ and these geometries can be designated $\{l/\varrho\}$ such that a polygon is described when $\varrho = 1$ or $\varrho = l - 1$. If $\varrho = 0$ or $\varrho|l$ we have a special case where the polygon collapses and our structure lies in the pseudo-convergence. Otherwise we have a near-regular star-polygon which is a self-intersecting, near-equilateral near-equiangular structure. For instance, in a regular pentagon, a five-pointed star can be obtained by drawing a line from the first to the third vertex, from the third vertex to the fifth vertex, from the fifth vertex to the second vertex, from the second vertex to the fourth vertex, and from the fourth vertex to the first vertex. Our structures have a missing side which is nearly co-linear with the larger neighbouring vectors where $l|n$.

This section illustrates the structures that lie between the l^{th} vectors near the *point-of-inflection* of a series of $\mathcal{R}_r$ superstructures. The notation is $\{l/\varrho\}$ with l being the number of sides in a regular polygon or the number of vertices in a regular star polygram, the ϱ is the neighbouring vertex in a clockwise direction to which vector moves to.

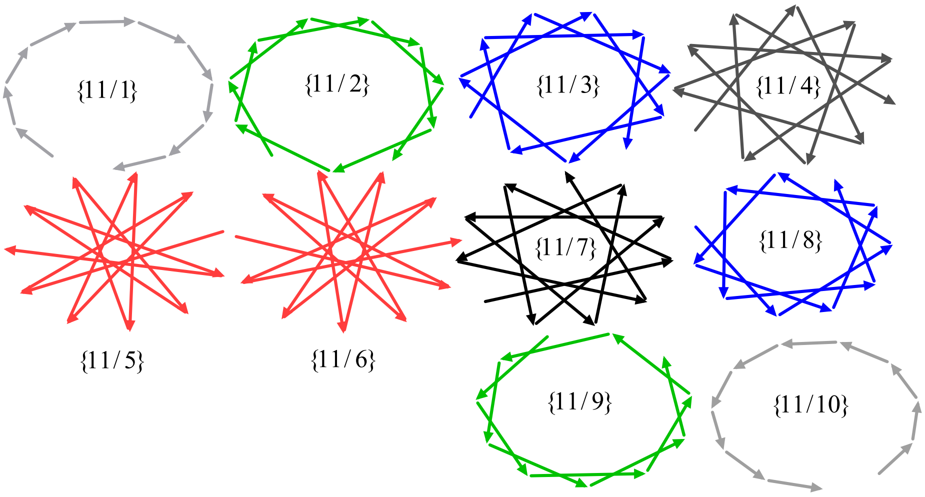

Figure A1. Two near regular polygons {11/1} and {11/10}, and eight near regular star-polygons for $l = 11$ are shown taken from $\mathrm{P}(\eta_l(s))$ near the points of inflection for $\mathcal{R}_1$ to $\mathcal{R}_{10}$ for $t = 39096.46$. The structures are not to the same scale.

In Figure A1 the larger l^{th} vectors $(11|m)$ which neighbour the structures are not shown, but would be roughly co-linear with each other and in-line with the missing segment of each near regular structure. The value of $q_{\bar{r}}$ is such that the change in argument at each vector is $\frac{q_{\bar{r}}\pi}{l}$ so that from an l^{th} vector to the next l^{th} vector we have l roughly equal arguments that when summated bring us full circle to give the collinearity seen at inflection. The $\{l/0\}$ structures are collapsed sections that essentially oscillate along one line making no advance in the Argand plane. These are located at pseudo-convergences along the pathways. Details appear in Table A1.

Table A1. Polygons and star-polygons

r	$q_{\bar{r}}$	$\left\{l/\left(\frac{q_{\bar{r}}}{2}mod(l)\right)\right\}$	Structural position
		$\{11/0\}$	P-C
1	2	$\{11/1\}$	Inf
2	4	$\{11/2\}$	Inf
3	6	$\{11/3\}$	Inf
4	8	$\{11/4\}$	Inf
5	10	$\{11/5\}$	Inf
6	12	$\{11/6\}$	Inf
7	14	$\{11/7\}$	Inf
8	16	$\{11/8\}$	Inf
9	18	$\{11/9\}$	Inf
10	20	$\{11/10\}$	Inf
		$\{11/11\} \equiv \{11/0\}$	P-C
11	24	$\{11/12\} \equiv \{11/1\}$	Inf
12	26	$\{11/13\} \equiv \{11/2\}$	Inf

"Inf" means a *point-of-inflection* and "P-C" means a pseudo-convergence

A2. A Note on the collapse of structures either side of $2l|q$

Inherent in the specification of R_l is the absence of the odd values of q either side of the q where $2l|q$. The is illustrated in Figure A2.

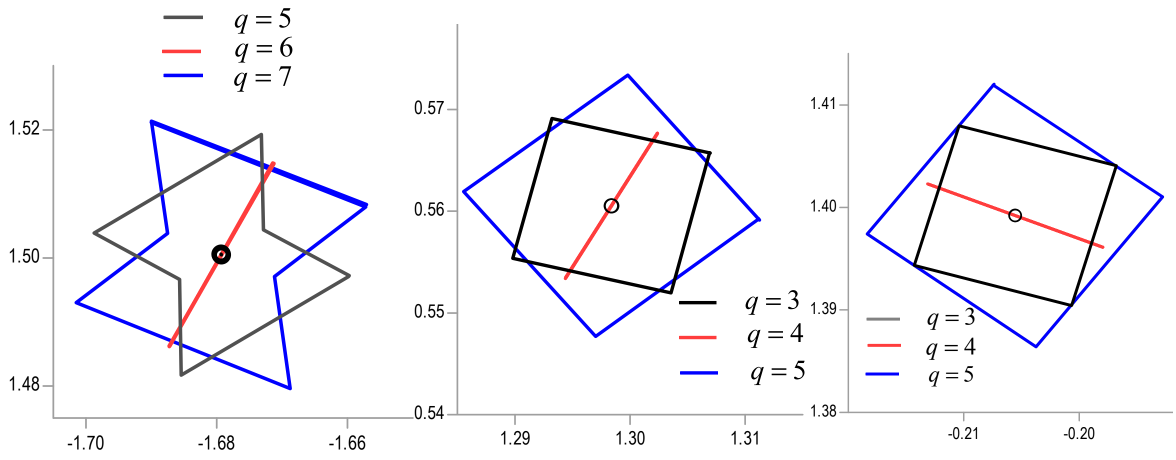

(a) (b) (c)

Figure A2. (a) With $l = 3$ and $t = 27016$ the average of neighbouring vectors where $l|m$ is shown with all three averages being in the centre of the black circle. All three values of q have an equivalence when $q|2l$. **(b)** With $l = 2$ the common pseudo-convergence is evident for $t = 27016$. **(c)** As in (b) but with $t = 27017$ to show that there has been movement in the Argand plane and rotation of structures but still a shared pseudo-convergence.

A3. Calculations of $|\Delta\hat{\eta}_{q_r}|/|\Delta\hat{\eta}_1|$ *and* $\left(\frac{q_{\bar{r}}}{2}\right)^{(\sigma-1)}$

Calculations were made to provide reassurance that Equation (17) represents the lengths of *principal-axes* determined from direct summations. Averaging was applied as in Equation (13), as reproduced here. The magnitude of the *principal-axis* by calculation is simply;

$$\hat{\eta}_q(\mathrm{s}) := \tfrac{1}{4}\left(\eta_{l,a-1}(\mathrm{s}) + \eta_{l,a}(\mathrm{s}) + \eta_{l,b-1}(\mathrm{s}) + \eta_{l,b}(s)\right)$$

with $a = l\lfloor m(q)/l\rfloor$ and $b = l(\lfloor m(q)/l\rfloor + 1)$ and $q \in R_l$,

giving $|\Delta\hat{\eta}_{q_r}| = |\hat{\eta}_{q_r}(\mathrm{s}) - \hat{\eta}_{q_{r+1}}(\mathrm{s})|$.

In Figure A3 an early part of a pathway is shown and in the table the ratios of interest.

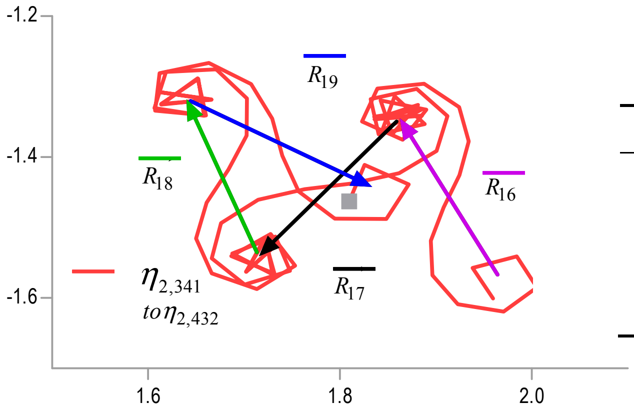

Table A2. Calculations .

	$\lvert\Delta\hat{\eta}_{q_r}\rvert$	$\lvert\Delta\hat{\eta}_{q_r}\rvert/\lvert\Delta\hat{\eta}_1\rvert$	$q_{\bar{r}}/2$	$(q_{\bar{r}}/2)^{(\sigma-1)}$
$\mathcal{R}_{19}$	0.230345	0.162879	37	0.164399
$\mathcal{R}_{18}$	0.235747	0.166698	35	0.169031
$\mathcal{R}_{17}$	0.245132	0.173335	33	0.174078
$\mathcal{R}_{16}$	0.250194	0.176914	31	0.179605

Figure A3. A region of the pathway in $\eta_{2,n}(s)$ for $\sigma = \frac{1}{2}$ for $t_{50,000} = 40433.68739$ running from $m = 341$ (grey square) to $m = 432$ showing the vectors $\vec{\mathcal{R}}_{19}$ to $\vec{\mathcal{R}}_{16}$. The incorporated table compares computations from partial series on the left with the output of direct calculations on the right.

Part of a pathway to convergence is shown to illustrate four relatively early vectors in a distal pathway where inadequacies of approximations should be most evident; reassuringly the errors are small. If we look closer to convergence we find much smaller errors, see Table A3.

Table A3. Calculations .

	$\lvert\Delta\hat{\eta}_{q_r}\rvert$	$\lvert\Delta\hat{\eta}_{q_r}\rvert/\lvert\Delta\hat{\eta}_1\rvert$	$\frac{q_{\bar{r}}}{2}$	$\left(\frac{q_{\bar{r}}}{2}\right)^{-\frac{1}{2}}$
$\mathcal{R}_5$	0.471419	0.333344	9	0.333333
$\mathcal{R}_4$	0.534537	0.377975	7	0.377964
$\mathcal{R}_3$	0.632446	0.447207	5	0.447214
$\mathcal{R}_2$	0.816487	0.577344	3	0.57735
$\mathcal{R}_1$	1.414213	1	1	1

Table A3 is a comparison of the ratio of averaged summations $\lvert\Delta\hat{\eta}_{q_r}\rvert/\lvert\Delta\hat{\eta}_1\rvert$ and $\left(\frac{q_{\bar{r}}}{2}\right)^{-\frac{1}{2}}$ for the distal pathway for $\eta_{l,n}(s)$ for $\sigma = \frac{1}{2}$ for $t_{50,000} = 40433.68739$ and $l = 2$. The summations yield $\lvert\Delta\hat{\eta}_1\rvert^2$ =1.999998.

For comparison a table for $l = 5$ appears below, principally to illustrate the more intricate values of $\frac{q_{\bar{r}}}{2}$ and once again we see $\left|\Delta\hat{\eta}_1\right|^2 = 4.999978$.

Table A4. Calculations.

	$\lvert\Delta\hat{\eta}_{q_r}\rvert$	$\lvert\Delta\hat{\eta}_{q_r}\rvert/\lvert\Delta\hat{\eta}_1\rvert$	$\frac{q_{\bar{r}}}{2}$	$\left(\frac{q_{\bar{r}}}{2}\right)^{-\frac{1}{2}}$
$\mathcal{R}_{15}$	0.533496	0.238587	18	0.23570226
$\mathcal{R}_{14}$	0.547925	0.24504	17	0.242535625
$\mathcal{R}_{13}$	0.557137	0.24916	16	0.25
$\mathcal{R}_{12}$	0.596435	0.266734	14	0.267261242
$\mathcal{R}_{11}$	0.6225107	0.278396	13	0.277350098
$\mathcal{R}_{10}$	0.6463426	0.289054	12	0.288675135
$\mathcal{R}_9$	0.6736206	0.301253	11	0.301511345
$\mathcal{R}_8$	0.7454706	0.333385	9	0.333333333
$\mathcal{R}_7$	0.7908195	0.353666	8	0.353553391
$\mathcal{R}_6$	0.844766	0.377792	7	0.377964473
$\mathcal{R}_5$	0.9128243	0.408228	6	0.40824829
$\mathcal{R}_4$	1.1180591	0.500012	4	0.5
$\mathcal{R}_3$	1.2910683	0.577385	3	0.577350269
$\mathcal{R}_2$	1.5811098	0.707096	2	0.707106781
$\mathcal{R}_1$	2.2360624	1	1	1

Table A3 is a comparison of the ratio of averaged summations $\lvert\Delta\hat{\eta}_{q_r}\rvert/\lvert\Delta\hat{\eta}_1\rvert$ and $\left(\frac{q_{\bar{r}}}{2}\right)^{-\frac{1}{2}}$ for the distal pathway for $\eta_{l,n}(\mathrm{s})$ for $\sigma = \frac{1}{2}$ for $t_{50,000} = 40433.68739$ and $l = 5$. Note that the $\frac{q_{\bar{r}}}{2}$ column has no integers which have l as a factor.

A4. The function $x = f(t)$

The function *lambda* acts on s with the parameters x and l with $0 < x \leq 1$ so that

$$\lambda_l(s, x) = \ell_{l,\kappa-1}(s) + x\vec{\mathcal{L}}_\kappa - \left(h_{l,\kappa-1}(s) + x\vec{\mathcal{R}}_\kappa\right).$$

In this exercise x was determined from the intersection of $\vec{\mathcal{L}}_\kappa$ and $\vec{\mathcal{R}}_\kappa$ at known non-trivial zeros. This is formally the same as determining x to satisfy for each ρ_i

$$\ell_{l,\kappa-1}(\rho_i) + x\vec{\mathcal{L}}_\kappa = h_{l,\kappa-1}(\rho_i) + x\vec{\mathcal{R}}_\kappa.$$

In Figure A.2 x is plotted against t for all the t_i in an interval in t.

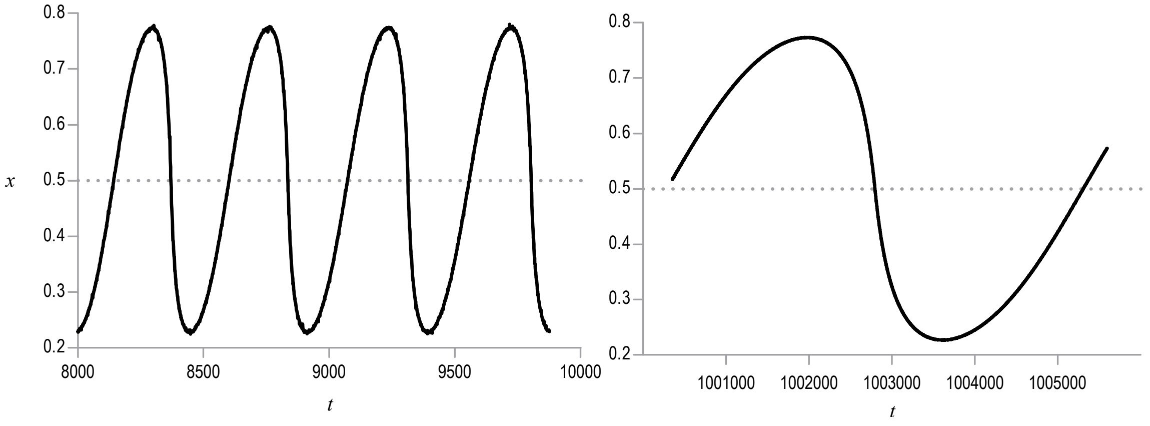

(a) (b)

Figure A4. (a) and **(b)** the fraction x against t_i oscillates about $x = \frac{1}{2}$ with a gradually decreasing frequency.

Figure A4 shows the frequency of oscillation relates to t and Figure A5 adds in a plot for $\dot{\kappa}$ as a function of t.

$$\dot{\kappa} = \frac{1}{2}\left(\left(e^{\frac{2\pi}{t}} - 1\right)^{-\frac{1}{2}} + \left(1 - e^{-\frac{2\pi}{t}}\right)^{-\frac{1}{2}}\right) - \left[\frac{1}{2}\left(\left(e^{\frac{2\pi}{t}} - 1\right)^{-\frac{1}{2}} + \left(1 - e^{-\frac{2\pi}{t}}\right)^{-\frac{1}{2}}\right)\right]$$

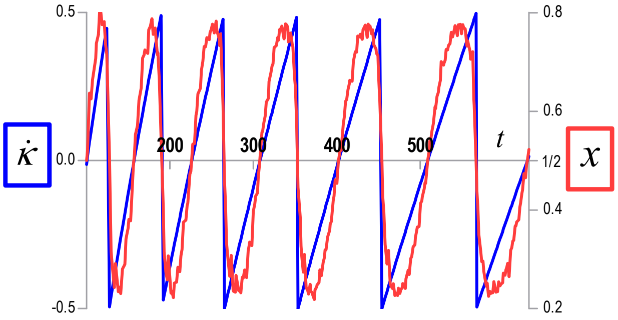

Figure A5. These plots illustrate the relationship between x in red on the (right-hand axis) representing the intersection of $\vec{\mathcal{L}}_\kappa$ and the $\vec{\mathcal{R}}_\kappa$ vector for all the non-trivial zeros in the interval $t = 100$ to $t = 630$ and $\dot{\kappa}$ in blue (left-hand axis) which is the residual associated with κ after rounding to the nearest integer.

The relationship between x and $\dot{\kappa}$ without t appears in Figure A6.

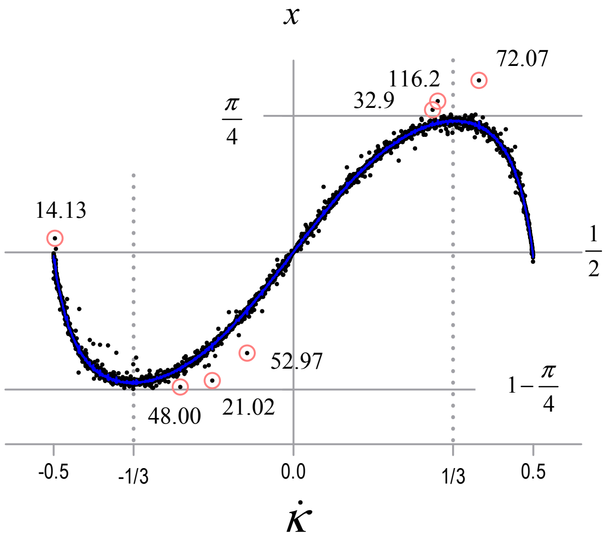

Figure A6. The first 10,000 non-trivial zeros have been used to illustrate the relationship between $\dot{\kappa}$ and x. A smoothed curve is plotted in blue and it is noted that the principal outliers all have low values of t.

Figure A6 uses $l = \kappa + 1$ but the *kappa* vector is independent of l and so this does not affect the plot. *Kappa* dot is by definition limited to $-\frac{1}{2} < \dot{\kappa} < \frac{1}{2}$ and $0 < x \leq 1$, however x appears to have bounds of $\frac{\pi}{4}$ and $1 - \frac{\pi}{4}$ which occur at $\dot{\kappa} = \frac{1}{3}$ and $\dot{\kappa} = -\frac{1}{3}$ respectively. Figure A7 shows an example of intersection when $x \approx 0$.

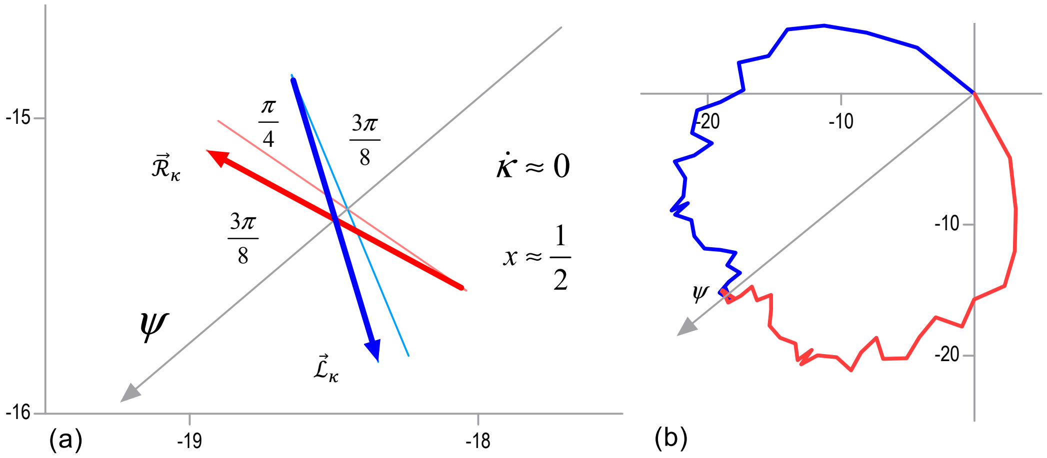

Figure A7. (a) An illustration of $\vec{\mathcal{R}}_\kappa$ from $\mathrm{P}(h_{l,\kappa}(s))$ in red and $\vec{\mathcal{L}}_\kappa$ from $\mathrm{P}(\ell_{l,\kappa}(s))$ in blue for the non-trivial zero $t = 5655.819253$ at $\sigma = \frac{1}{2}$ with $\kappa = 30$ and $l = 31$. **(b)** The two pathways whose final vectors are shown in (a). The figure shows that when $\dot{\kappa} \approx 0$ then $x \approx \frac{1}{2}$ and the vectors $\vec{\mathcal{R}}_\kappa$ and $\vec{\mathcal{L}}_\kappa$ intersect at $\frac{\pi}{4}$.

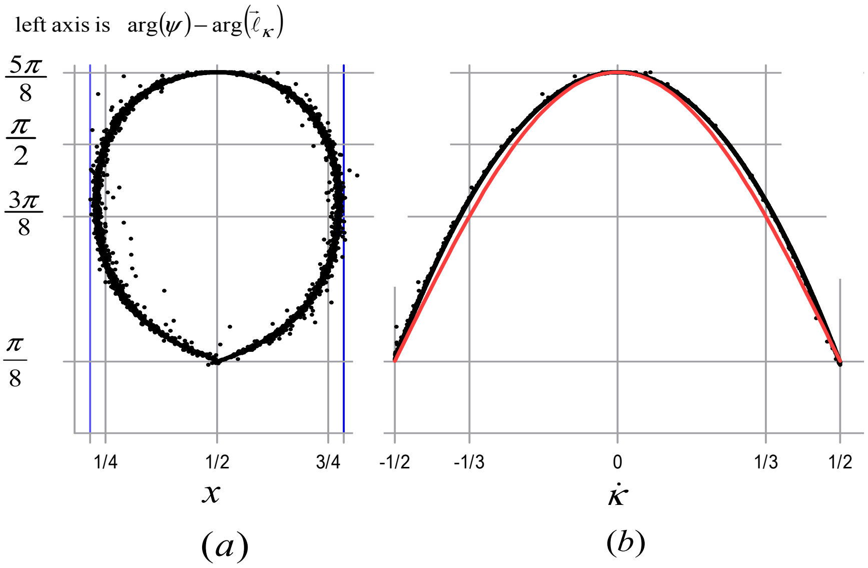

Figure A8. Both figures are dot plots for the first 10,000 nontrivial zeros. The vertical axis in both figures is the reduced argument $\arg(\psi) - \arg(\vec{\mathcal{L}}_\kappa)$. In **(a)** the horizontal axis is x with the blue lines at $\frac{\pi}{4}$ and $1 - \frac{\pi}{4}$. In **(b)** the horizontal axis is $\dot{\kappa}$. The difference in arguments is roughly tracked by the red cosine curve with amplitude $\frac{\pi}{2}$ and period $2\dot{\kappa}$ and lifted by $\frac{\pi}{8}$.

If at a non-trivial zero the difference in arguments were exactly $\frac{\pi}{2}$ then the $\vec{\ell}_\kappa$ vector and the $\vec{\mathcal{R}}_\kappa$ vector would be collinear and x would not be defined.

An example of a non-trivial zero with nearly collinear kappa vectors

In the following example a non-trivial zero with $l = \kappa + 1$ is illustrated with the *kappa* vectors nearly collinear to each other where they meet.

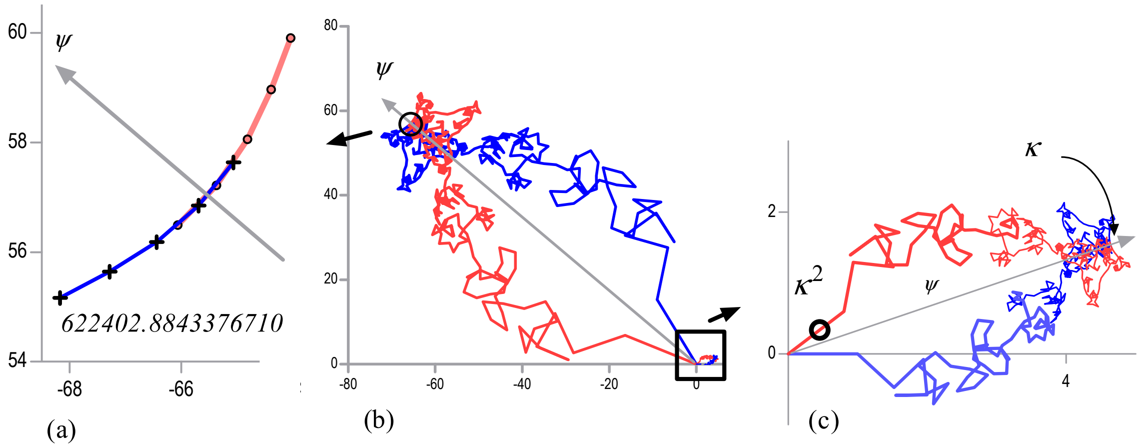

Figure A9. $P(h_{l,\kappa}(s))$ in red and $P(\ell_{l,\kappa}(s))$ in blue with $\kappa = 315$ and $l = 3$ for $t_i =$ 622402.884 at $\sigma = \frac{1}{2}$. **(a)** The *kappa* vectors are almost co-linear being at 92.7 degrees to ψ. **(b)** Both pathways in full; the bottom right hand corner shows the associated pathway $P(\zeta_{\kappa l}(s))$ which nearly vanishes at the non-trivial zero. **(c)** The partial Euler's *zeta*, is taken from (b) and enlarged with $P(h_{1,\kappa}(s))$ in red and $P(\zeta_\kappa(s))$ in blue. The black circle represents the end of the partial series with $\vec{m}$ for $m = \kappa l$ lying near the *point-of-inflection* in the $\mathcal{R}_1$ of $\zeta_\tau(s)$.

In Figure A9 it can be seen that the *kappa* vectors can be almost collinear. It is likely that true collinearity would not occur for any t. The figure also illustrates that the partial Euler's *zeta* function nearly vanishes when $l = \kappa + 1$.

An example of an intricate pathway and kappa vectors at an extreme angle

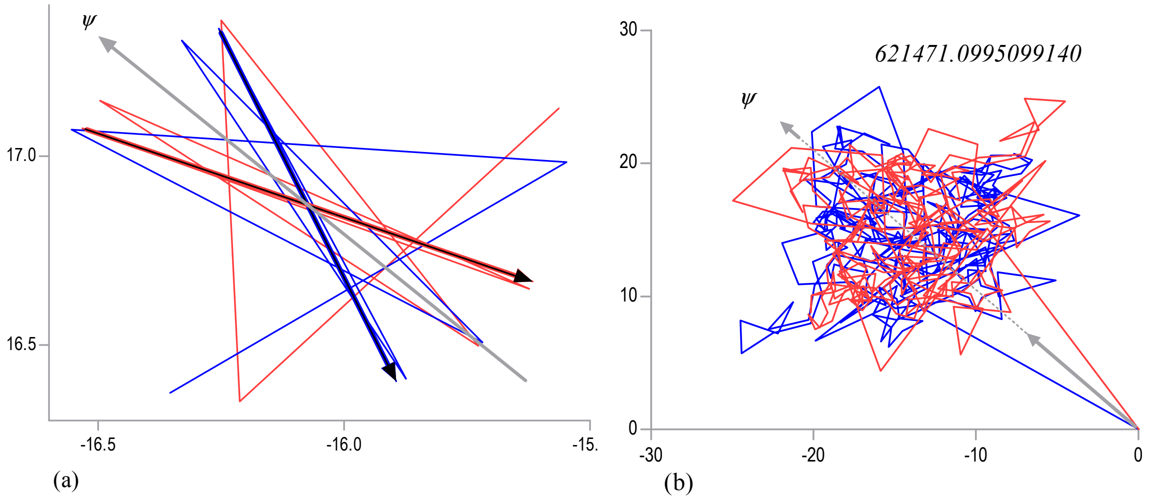

(a) (b)

Figure A10. A non-trivial zero with *kappa* vectors meeting at 22.5 degrees; $\kappa = 314$, $t = 621471.099509914$

In Figure A10 the two *kappa* vectors are heading almost in the same direction which seems counter intuitive but this is possible since subsequent vectors soon fall in line with complimentary superstructures.

A5. An example showing failure of superposition either side of a zero and showing "opportunistic superstructures" in the proximal pathway.

In Figure A10 a short region of the mirror-image pathways for values of t slightly below a t_i in (a), for the t_i in (b) and for a t slightly above the t_i in (c). In (b) there is symmetry and perfect superposition at the zero either side of ψ such that the light blue dashed line is the overlap extending $P(\ell_l(s))$ beyond κ terms.

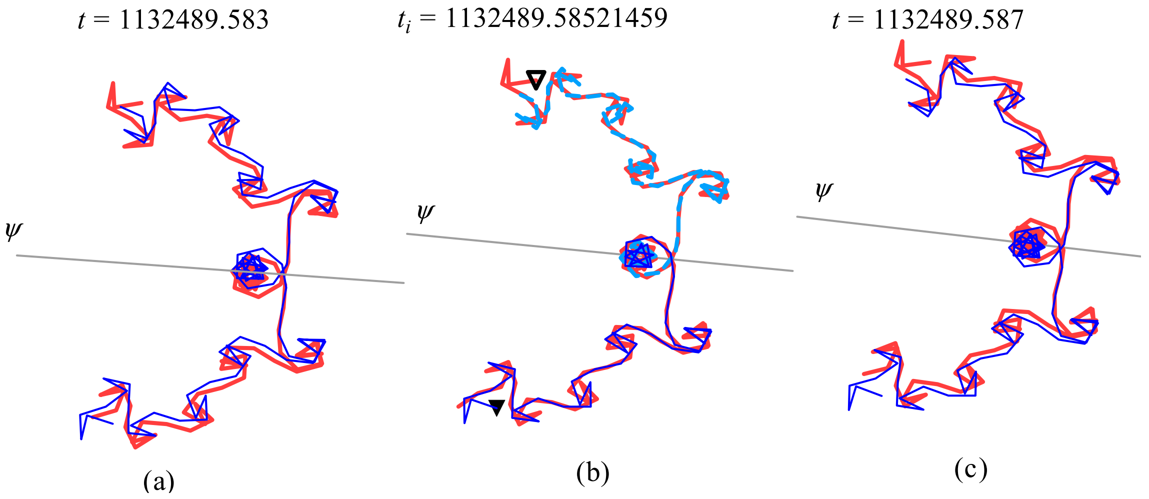

$t = 1132489.583$ $t_i = 1132489.58521459$ $t = 1132489.587$

(a) (b) (c)

Figure A11. Three plots of parts of two pathways. In **(a)** $t < t_i$ in **(b)** $t = t_i$ with i being 200,1050, and in **(c)** $t < t_i$. $\mathrm{P}(\ell_{l,n}(s))$ is shown in blue, starting at the bottom of (b) with a solid black triangle. $\mathrm{P}(h_{l,\kappa}(s))$ is in red, starting at the top of (b) with an open triangle. Each pathway has been extended beyond the $\vec{\ell}_\kappa$ vector to show the congruence of the pathways. It is evident that this non-trivial zero of $\zeta(s)$ is easily located to a small interval in t by the finite series using $\kappa = 425$ and $l = 426$.

In Figure A11 a small interval in t is illustrated to show that the superposition of the more distal pathways on the proximal pathways provides a mechanism for isolating non-trivial zeros and narrowing down the region of intersection that could host a non-trivial zero. It can also be appreciated how slight changes in σ would separate pathways and preclude superposition.

Interestingly, there appear to be $\mathcal{R}_r$ superstructures in $\mathrm{P}\big(\ell_{l,n}(s)\big)$ before its *kappa* vector yet the vectors of $\mathrm{P}\big(h_{l,r}(s)\big)$ clearly do not equate to what might be imagined to be the *principal-axes* of these superstructures. This is simply because the vectors of $\mathrm{P}\big(\ell_{l,n}(s)\big)$ do not satisfy Equation (37). These structures appear because sequential $Arg\left(t\ln\left(\frac{n+1}{n}\right)\right)$, which is the reduced form, generate a closely falling sequence, however since $t\ln\left(\frac{(n+1)^2}{n(n+2)}\right) > 2\pi$ these are not true superstructures. It is important to appreciate that if

$$t\ln\left(\frac{n+1}{n}\right) - t\ln\left(\frac{n+2}{n+1}\right) > 2\pi \tag{B1}$$

the region is in the proximal pathway. This analysis is formally the same as noting that if two l^{th} vector differs in argument by $t\ln\left(\frac{(k+1)l}{kl}\right) = 2\pi$ then $kl = \left(e^{\frac{2\pi}{t}} - 1\right)^{-1}$ and with $l = \kappa + 1$ we have $\kappa \approx \left(e^{\frac{2\pi}{t}} - 1\right)^{-1/2}$.

A6. A comparison of the magnitudes of the principal-axes of $\mathcal{R}_r$ structures by summation, and the complementary vectors $\vec{\mathcal{R}}_r$ by single calculation

A comparison was made between $|\vec{\mathcal{R}}_r|$ for $\mathrm{P}(h_l(s))$ at low r and the magnitude of the *principal-axis* of the related $\mathcal{R}_r$ in $\eta_l(s)$, here designated $|\Delta\hat{\eta}_{q_r}|$. The chosen parameters were $l = 5$ and $t = 40433.69$ over a range of values of σ. The $|\vec{\mathcal{R}}_r|$ was determined by Equation (17) as reproduced here;

$$|\vec{\mathcal{R}}_r| = \sqrt{l}\,\nu^{\left(\frac{1}{2}-\sigma\right)}\left(\frac{q_{\bar{r}}}{2}\right)^{(\sigma-1)} \text{ with } q_{\bar{r}} \in \chi_l.$$

The magnitude of the *principal-axis* of the $\mathcal{R}_r$ was determined from the location of the start and finish points of the axis after summation of the partial series. Averaging was applied as in Equation (13), as reproduced here. The magnitude of the *principal-axis* by calculation is simply;

$$\hat{\eta}_q(\mathrm{s}) := \tfrac{1}{4}\big(\eta_{l,a-1}(\mathrm{s}) + \eta_{l,a}(\mathrm{s}) + \eta_{l,b-1}(\mathrm{s}) + \eta_{l,b}(s)\big)$$

$$\text{with } a = l\lfloor m(q)/l\rfloor \text{ and } b = l(\lfloor m(q)/l\rfloor + 1) \text{ and } q \in R_l,$$

$$\text{giving } |\Delta\hat{\eta}_{q_r}| = |\hat{\eta}_{q_r}(\mathrm{s}) - \hat{\eta}_{q_{r+1}}(\mathrm{s})|.$$

The results appear in Table A5 with σ rising from 0 to 1.1.

doi:10.20944/preprints201703.0121.v1

Table A5.

r	$q_{\bar{r}}$	Eq 0	$\lvert\Delta\hat{\eta}_{q_r}\rvert$ 0	Eq 0.1	$\lvert\Delta\hat{\eta}_{q_r}\rvert$ 0.1	Eq 0.2	$\lvert\Delta\hat{\eta}_{q_r}\rvert$ 0.2	Eq 0.3	$\lvert\Delta\hat{\eta}_{q_r}\rvert$ 0.3
1	2	401.09604	401.09838	142.06781	142.06841	50.320277	50.3204	17.823392	17.82341
2	4	200.54802	200.54618	76.132256	76.131421	28.90141	28.90104	10.971585	10.97142
3	6	133.69868	133.70715	52.85506	52.858343	20.895175	20.89645	8.2604836	8.260976
4	8	100.27401	100.27624	40.798266	40.799172	16.599501	16.59987	6.7538025	6.753953
5	12	66.849339	66.846111	28.324325	28.322943	12.001127	12.00053	5.0849241	5.08467
6	14	57.299434	57.274438	24.655139	24.644271	10.608759	10.60403	4.5647997	4.562745
7	16	50.137005	50.153472	21.863249	21.870377	9.5339097	9.536994	4.1574531	4.158788
8	18	44.566226	44.573338	19.664252	19.667366	8.6765888	8.677953	3.828429	3.829026
9	22	36.463276	36.432693	16.415053	16.401219	7.3897352	7.383478	3.326714	3.323883
10	24	33.42467	33.467856	15.17863	15.198294	6.8928373	6.901791	3.1301379	3.134215
11	26	30.853541	30.968401	14.123641	14.176347	6.4652949	6.489481	2.9595794	2.970678
12	28	28.649717	28.590153	13.212362	13.185171	6.0931321	6.08072	2.8099638	2.804299
13	32	25.068502	24.984676	11.716225	11.677007	5.4757932	5.457444	2.5592126	2.550627
14	34	23.593884	23.837881	11.09409	11.208776	5.2165561	5.270463	2.4528789	2.478217
15	36	22.283113	22.554743	10.537812	10.666366	4.9833916	5.044233	2.3566745	2.385469
16	38	21.110318	20.918401	10.037313	9.9463647	4.7724363	4.729337	2.269148	2.248724
17	42	19.099811	19.337312	9.1727241	9.2870576	4.4052198	4.46026	2.115616	2.142113
18	44	18.231638	18.345793	8.7966089	8.8515107	4.2442883	4.270693	2.0478327	2.060532

r	$q_{\bar{r}}$	Eq 0.4	$\lvert\Delta\hat{\eta}_{q_r}\rvert$ 0.4	Eq 0.5	$\lvert\Delta\hat{\eta}_{q_r}\rvert$ 0.5	Eq 0.6	$\lvert\Delta\hat{\eta}_{q_r}\rvert$ 0.6	Eq 0.7	$\lvert\Delta\hat{\eta}_{q_r}\rvert$ 0.7
1	2	6.3130274	6.313022	2.236068	2.236062	0.792013	0.79201	0.2805302	0.280529
2	4	4.1650448	4.164976	1.5811388	1.58111	0.6002336	0.600221	0.2278613	0.227856
3	6	3.2656146	3.265805	1.2909944	1.291068	0.5103685	0.510397	0.2017638	0.201775
4	8	2.7479048	2.747966	1.118034	1.118059	0.454892	0.454902	0.1850809	0.185085
5	12	2.1545021	2.154393	0.9128709	0.912824	0.386787	0.386767	0.1638831	0.163875
6	14	1.964169	1.963276	0.8451543	0.844766	0.363658	0.363489	0.1564769	0.156404
7	16	1.8129411	1.813519	0.7905694	0.790819	0.3447437	0.344852	0.1503324	0.150379
8	18	1.6892432	1.689505	0.745356	0.745471	0.3288784	0.328929	0.1451132	0.145135
9	22	1.4976215	1.496341	0.6741999	0.673621	0.3035116	0.303249	0.136635	0.136516
10	24	1.4214413	1.423298	0.6454972	0.646343	0.2931297	0.293515	0.1331145	0.13329
11	26	1.354789	1.359882	0.6201737	0.622511	0.2838932	0.284966	0.1299561	0.130448
12	28	1.2958683	1.293283	0.5976143	0.596435	0.2756012	0.275063	0.1270987	0.126853
13	32	1.196095	1.192078	0.559017	0.557137	0.2612669	0.260387	0.1221079	0.121696
14	34	1.1533691	1.165279	0.5423261	0.547925	0.2550074	0.257639	0.1199071	0.121144
15	36	1.1144849	1.128113	0.5270463	0.533496	0.2492432	0.252296	0.1178685	0.119313
16	38	1.0789107	1.069232	0.5129892	0.508403	0.2439107	0.241737	0.1159721	0.114942
17	42	1.016029	1.028785	0.48795	0.494091	0.234339	0.237295	0.1125418	0.113965
18	44	0.9880617	0.994169	0.4767313	0.479669	0.2300188	0.231431	0.1109821	0.111661

Table A5(continued).

r	$q_{\bar{r}}$	Eq	$\lvert\Delta\hat{\eta}_{q_r}\rvert$	Eq	$\lvert\Delta\hat{\eta}_{q_r}\rvert$	Eq	$\lvert\Delta\hat{\eta}_{q_r}\rvert$	Eq	$\lvert\Delta\hat{\eta}_{q_r}\rvert$
		0.8	0.8	0.9	0.9	1	1	1.1	1.1
1	2	0.0993635	0.099363	0.0351945	0.035194	0.0124658	0.012466	0.0044154	0.004415
2	4	0.086501	0.086499	0.0328376	0.032837	0.0124658	0.012465	0.0047323	0.004732
3	6	0.0797632	0.079768	0.0315328	0.031534	0.0124658	0.012466	0.0049281	0.004928
4	8	0.0753035	0.075305	0.0306386	0.030639	0.0124658	0.012466	0.0050719	0.005072
5	12	0.0694379	0.069434	0.0294211	0.02942	0.0124658	0.012465	0.0052818	0.005282
6	14	0.0673298	0.067298	0.0289711	0.028957	0.0124658	0.01246	0.0053639	0.005361
7	16	0.0655555	0.065576	0.0285868	0.028596	0.0124658	0.01247	0.005436	0.005438
8	18	0.0640293	0.064039	0.0282521	0.028256	0.0124658	0.012468	0.0055004	0.005501
9	22	0.0615104	0.061457	0.0276908	0.027666	0.0124658	0.012455	0.0056119	0.005607
10	24	0.0604492	0.060529	0.0274509	0.027487	0.0124658	0.012482	0.0056609	0.005668
11	26	0.0594892	0.059715	0.027232	0.027336	0.0124658	0.012513	0.0057064	0.005728
12	28	0.058614	0.058502	0.027031	0.02698	0.0124658	0.012443	0.0057489	0.005738
13	32	0.0570694	0.056877	0.0266724	0.026582	0.0124658	0.012424	0.0058261	0.005806
14	34	0.0563816	0.056963	0.0265112	0.026785	0.0124658	0.012594	0.0058616	0.005922
15	36	0.0557407	0.056425	0.0263601	0.026684	0.0124658	0.012619	0.0058952	0.005968
16	38	0.0551412	0.054653	0.026218	0.025987	0.0124658	0.012356	0.0059271	0.005875
17	42	0.0540484	0.054734	0.0259569	0.026287	0.0124658	0.012625	0.0059867	0.006063
18	44	0.0535479	0.053875	0.0258364	0.025994	0.0124658	0.012541	0.0060147	0.006051

The same exercise was repeated for the differentials. A comparison being made between the $\left|\frac{\partial\vec{\mathcal{R}}_r}{\partial\sigma}\right|$ for low values of r in $\mathrm{P}\big(\bar{h}'_l(s)\big)$ and the magnitude of the *principal-axis* of the related superstructure, still designated $\mathcal{R}_r$, in $\eta'_l(s)$, for $l = 5$ and $t = 40433.69$ determined over the same range of real domains. The formulation for the single calculation is simply

$$\left|\frac{\partial\vec{\mathcal{R}}_r}{\partial\sigma}\right| = \sqrt{l}\,\nu^{\left(\frac{1}{2}-\sigma\right)}\left(\frac{q_{\bar{r}}}{2}\right)^{(\sigma-1)}\ln\left(\frac{2\nu}{q_{\bar{r}}}\right) \text{ with } q_{\bar{r}}\ \in \chi_l.$$

The magnitude of the *principal-axis* of the $\mathcal{R}_r$ which represents the superstructure in $\mathrm{P}(\eta'_l(\mathrm{s}))$ was determined from the location of the start and finish points of the axis after summation of the partial series. Averaging was applied as in a modification of Equation (13), as reproduced here. The magnitude of the *principal-axis* by summation is simply;

$$\widehat{\eta'}_q(\mathrm{s}) := \tfrac{1}{4}\big(\eta'_{l,a-1}(\mathrm{s}) + \eta'_{l,a}(\mathrm{s}) + \eta'_{l,b-1}(\mathrm{s}) + \eta'_{l,b}(s)\big)$$

$$\text{with } a = l\lfloor m(q)/l\rfloor \text{ and } b = l(\lfloor m(q)/l\rfloor + 1) \text{ and } q \in R_l$$

$$\left|\Delta\widehat{\eta'}_{q_r}\right| = \left|\widehat{\eta'}_{q_r}(\mathrm{s}) - \widehat{\eta'}_{q_{r+1}}(\mathrm{s})\right|.$$

The results appear in Table A6 with σ rising from 0 to 1.1.

Table A6.

r	$q_{\bar{r}}$	Eq 0	$\lvert\Delta\widehat{\eta}'_{q_r}\rvert$ 0	Eq 0.1	$\lvert\Delta\widehat{\eta}'_{q_r}\rvert$ 0.1	Eq 0.2	$\lvert\Delta\widehat{\eta}'_{q_r}\rvert$ 0.2	Eq 0.3	$\lvert\Delta\widehat{\eta}'_{q_r}\rvert$ 0.3
1	2	4162.9998	4162.992	1474.5281	1474.525	522.2756	522.2745	184.9892	184.9888
2	4	1942.4896	1942.457	737.4088	737.3964	279.9355	279.9307	106.2693	106.2674
3	6	1240.7825	1240.851	490.5174	490.5447	193.9158	193.9266	76.6606	76.66486
4	8	901.7396	901.7511	366.8882	366.8935	149.2748	149.2771	60.7350	60.73606
5	12	574.0544	574.0215	243.2287	243.215	103.0568	103.0511	43.6655	43.66313
6	14	483.2138	483.001	207.9198	207.8276	89.4648	89.42488	38.4954	38.47809
7	16	416.1172	416.2511	181.4560	181.5142	79.1274	79.15273	34.5050	34.51606
8	18	364.6328	364.688	160.8891	160.9135	70.9901	71.00085	31.3234	31.32814
9	22	291.0187	290.7733	131.0107	130.8999	58.9784	58.92834	26.5509	26.52828

r	$q_{\bar{r}}$	Eq 0.4	$\lvert\Delta\widehat{\eta}'_{q_r}\rvert$ 0.4	Eq 0.5	$\lvert\Delta\widehat{\eta}'_{q_r}\rvert$ 0.5	Eq 0.6	$\lvert\Delta\widehat{\eta}'_{q_r}\rvert$ 0.6	Eq 0.7	$\lvert\Delta\widehat{\eta}'_{q_r}\rvert$ 0.7
1	2	65.5229	65.52274	23.2081	23.20805	8.220274	8.220254	2.911608	2.911601
2	4	40.3420	40.34127	15.3146	15.31437	5.813753	5.813647	2.207020	2.206979
3	6	30.3061	30.30786	11.9809	11.98158	4.736399	4.73667	1.872436	1.872544
4	8	24.7111	24.71155	10.0541	10.05433	4.090694	4.090785	1.664369	1.664409
5	12	18.5012	18.50023	7.8390	7.838614	3.321420	3.321249	1.407296	1.407225
6	14	16.5640	16.5565	7.1272	7.123997	3.066748	3.065341	1.319576	1.318967
7	16	15.0466	15.05138	6.5614	6.563443	2.861209	2.862114	1.247686	1.24808
8	18	13.8210	13.82311	6.0983	6.099254	2.690798	2.691212	1.187277	1.18746
9	22	11.9527	11.94246	5.3808	5.37624	2.422348	2.420268	1.090492	1.089553

r	$q_{\bar{r}}$	Eq 0.8	$\lvert\Delta\widehat{\eta}'_{q_r}\rvert$ 0.8	Eq 0.9	$\lvert\Delta\widehat{\eta}'_{q_r}\rvert$ 0.9	Eq 1	$\lvert\Delta\widehat{\eta}'_{q_r}\rvert$ 1	Eq 1.1	$\lvert\Delta\widehat{\eta}'_{q_r}\rvert$ 1.1
1	2	1.031287	1.031284	0.365280	0.365279	0.129382	0.129381	0.045827	0.045827
2	4	0.837830	0.837814	0.318057	0.318051	0.120741	0.120739	0.045836	0.045835
3	6	0.740229	0.740271	0.292634	0.292651	0.115687	0.115693	0.045734	0.045737
4	8	0.677177	0.677195	0.275521	0.275529	0.112101	0.112104	0.045610	0.045611
5	12	0.596276	0.596246	0.252644	0.252632	0.107046	0.107041	0.045356	0.045354
6	14	0.567794	0.56753	0.244314	0.244199	0.105124	0.105075	0.045234	0.045212
7	16	0.544078	0.544249	0.237256	0.23733	0.103460	0.103492	0.045116	0.04513
8	18	0.523869	0.52395	0.231150	0.231186	0.101992	0.102008	0.045002	0.045009
9	22	0.490917	0.490493	0.221001	0.220809	0.099490	0.099404	0.044788	0.044749

Appendix B Notation

$arg(z)$	unreduced argument of a complex number: $arg(z) \in \mathbb{R}$
$Arg(z)$	principal value of $arg(z)$ as $[0, 2\pi)$ or $(-\pi, \pi]$ if more helpful
α, β	reserved for σ_α when $0 < \sigma < \frac{1}{2}$ and σ_β when $\frac{1}{2} < \sigma < 1$
$\zeta(s)$	Euler's *zeta* function or Riemann's *zeta* function – determined by context

doi:10.20944/preprints201703.0121.v1

$\zeta_n(s)$	partial Euler's *zeta* function to n terms
$\eta(s)$	Dirichlet's *eta* function
$\eta_l(s)$	modified *eta* function: every l^{th} term of *zeta* is negated and multiplied by $l-1$
$\eta_{l,n}(s)$	modified *eta* series to n terms
$\eta_l(\sigma)$	the function $\eta_l(\sigma+it)$ for fixed t over an interval in σ
$\eta_l(t)$	the function $\eta_l(\sigma+it)$ for fixed σ over an interval in t
$\hat{\eta}_q(s)$	a point representing the centre of a pseudo-convergence indexed by q for a stated l
$\theta(s)$	any function that estimates a point of final pseudo-convergence for a divergent series
θ	the reduced angle between neighbouring vectors, $(0<\theta\leq 2\pi)$
ϑ	the primitive angle between neighbouring vectors which can be greater than 2π
κ and $\dot{\kappa}$	*Kappa* and *kappa* dot, integer and fraction relating to vectors at the junction of proximal and distal pathways
$\lambda_l(s,x)$	difference between 2 paired series used as a surrogate for $\eta_l(s)$ with $0<x\leq 1$
$\pi(x)$	the number of primes less than an integer x
ρ	any non-trivial zero of Riemann's *zeta* function
ρ_i	known non-trivial zeros on the critical-line with $\sigma=\frac{1}{2}$
ρ_u	un-known non-trivial zeros off the critical-line with $\sigma\neq\frac{1}{2}$
ϱ	*Rho* variant is used as ϱ_m and $\varrho_{\bar{m}}$ to determine a value of $q_{\bar{r}}$
σ	$Re(s)$ the real part of the domain of *zeta, eta* etc.
$\sigma_a,\ \sigma_b$	values of σ such that $\sigma_a<\sigma_b$ but without the restrictions of α,β (see above)
σ_c	value of σ at a cycloid-like curve where the differential will be zero
τ	an integer whose vector $\vec{\tau}$ separates a final pseudo-convergence from divergence
ψ	a line of reflection with $arg(\psi)$ but no specified magnitude
$\mu(n)$	the Möbius function
i	either $\sqrt{-1}$ or the index in $t_i,\ p_i,\ \rho_i$
j	$j\in\mathbb{N}_0$ used in the definition of $\eta_l(s)$ in two ways
k	Roman *k*, an integer $k\in\mathbb{N}$ as in $=\frac{2\pi k}{\ln(l)}$, the value of t at a trivial zero of $\eta_l(s)$
l	$l\in\mathbb{N}$, the negation index of $\eta_l(s)$ when $l\geq 2$ but also used as $l=1$ in Euler's *zeta*
$\mathcal{M}_m,$	a superstructure in the series $h_l(s)$ made from a set of sequential $\vec{\mathcal{R}}_r$
$\vec{m}$	vector with index m in Euler's *zeta* or in $\eta_l(s)$
$\lvert\vec{m}\rvert$	the magnitude of the vector $\vec{m}$
m,n	$m,n\in\mathbb{N}$, the index m is used for terms in Euler's *zeta* and in $\eta_{l,n}(s)$
p_i	an indexed prime
$\mathrm{P}\big(f_{l,n}(s)\big)$	the pathway of vectors in a series $f(s)$ with parameter l to n terms
$q,\ q_r, q_{\bar{r}}$	integral multipliers of either $\frac{\pi}{t}$ or $\frac{\pi}{tl}$; the indices refer to parts of superstructures
r	the index of $\mathcal{R}_r$ the superstructures in the distal Euler's *zeta* and in $\mathrm{P}(\eta_l(s))$
$\bar{r}$	r carries a bar when it relates to the *point-of-inflection* in an $\mathcal{R}_r$ superstructure
$\mathcal{R}_r$	a structure in Euler's *zeta* or $\mathrm{P}(\eta_l(s))$
$\vec{\mathcal{R}}_r$	a vector sharing properties with the *principal-axis* of an $\mathcal{R}_r$
s	the complex domain $s=\sigma+it$
$[x]$	the nearest integer to x with $\lfloor x\rfloor$ and $\lceil x\rceil$ being the floor and ceiling fucntions
$\mathbb{N},\mathbb{N}_0$	$\mathbb{N}=\{1,2,3,4,\ldots\}$ and $\mathbb{N}_0=\{0,1,2,3,4\ldots\}$
t	$Im(s)$ but also used in $\int_0^x\frac{1}{\ln(t)}dt$ and $\int_x^\infty\frac{dt}{t(t^2-1)\ln(t)}$

t_i	$Im(s)$ when $\zeta\left(\frac{1}{2}+it\right)=0$, the $Im\ (\rho_i)$
t_c	value of t at a cycloid like curve where the velocity will be zero
$\mid$ and $\nmid$	$l \mid m$ means l divides m whilst $l \nmid m$ means l does not divide m

Pathways notation: a summary

The notation for the four principal pathways appears in Table B1 with the pathway formulation, the name of the associated vector and the name of an indexed superstructure formed by a set of small vectors in that pathway forming the paired pseudo-spirals. The index of a superstructure indicates its position in the pathway with the superstructure that embraces convergence or the final pseudo-convergence preceding divergence having an index of 1. Superstructures exist in the distal part of a pathway after the *kappa* vector.

Table B1. Four pathways; designated vectors and associated distal superstructures.

Pathway	**Guide to structure**	**Vector**	**Superstructure**	**Distal/ proximal**	**Principal_axis of superstructure equates to**
$\mathrm{P}(\zeta_n(s))$		$\vec{m}$	$\mathcal{R}_r$	κ	$\vec{\mathcal{R}}_r$
$\mathrm{P}\big(\eta_{l,n}(s)\big)$	$\varrho_{\bar{r}} \in \mathbb{E}$	$\vec{m}$	$\mathcal{R}_r$	κl	$\vec{\mathcal{R}}_r$
$\mathrm{P}\big(h_{l,r}(s)\big)$	$q_{\bar{r}} \in \chi_l$	$\vec{\mathcal{R}}_r$	$\mathcal{M}_m$	κ	$\vec{m}$
$\mathrm{P}\big(\ell_{l,n}(s)\big)$		$\vec{\mathcal{L}}_n$	L_n	κ	some $\vec{\mathcal{R}}_r$

The vector $\vec{m}$ has no index because m is its own index

Each pathway has a named vector, an associated distal superstructure, an index and vector that separates proximal from distal pathways. A distal superstructure has a *principal-axis* upon which a vector from another pathway may be superimposed with meaning. Thus $\vec{\mathcal{R}}_r$ can be superimposed on an $\mathcal{R}_r$ and $\vec{m}$ may be superimposed on an $\mathcal{M}_m$. Some $\mathcal{L}_n$ may have an $\vec{\mathcal{R}}_r$ superimposed upon them.

References

1. Mueller, I. *Philosophy of Mathematics and Deductive Structure in Eulid's Elements. Book Title*, 3rd ed.; Dover Publications, Inc.: Mineola, New York, 1981; pp. 58-83.
2. The Experts Speak for Themselves. In The Riemann Hypothesis; Borwein, P., Choi, S., Rooney, B,. Weirathueller, A. Eds.; Springer: Canada, 2008; Chapter 12.3, pp. 199–221.
3. The Experts Speak for Themselves. In The Riemann Hypothesis; Borwein, P., Choi, S., Rooney, B,. Weirathueller, A. Eds.; Springer: Canada, 2008; Chapter 12.4, pp. 222–295.
4. Riemann B. Ueber die Anzahl der Primzahlen unter einer gegebenen Grösse (On the number of primes less than a given quantity). Monatsberichte der Berliner Akademie 1859
5. Empirical Evidence. In *The Riemann Hypothesis*; Borwein, P., Choi, S., Rooney, B,. Weirathueller, A. Eds.; Springer: Canada, 2008; Chapter 4, pp. 37–44.
6. Hardy, G. H. Sur les Zéros de la Fonction ζ(s) de Riemann. C. R. Acad. Sci. Paris 1914; 158: 1012–1014.
7. Edwards H.M. *Riemann's Zeta Function*, The Dover edition.; Dover Publications, Inc.: Mineola, New York, 2001; pp. 12–16.
8. http://www.dtc.umn.edu/~odlyzko/zeta_tables/index.html
9. Coxeter, H.S.M. Kaleidoscopes: Selected Writings of H.S.M; Sherk, F.A., McMullen, P,. Thompson, A.C. and Weiss, A, I.; Wiley-Interscience Publication, 1995, ISBN 978-0-471-01003-6